The Dissertation Committee for Ryan Patrick Hannigan certifies that this is the approved version of the following dissertation:

Stranger Things at the LHC

Committee:

Christina Markert, Supervisor

Peter Onyisi

Richard Hazeltine

Chandrajit Bajaj

Stranger Things at the LHC

by

Ryan Patrick Hannigan, B.S.

Dissertation

Presented to the Faculty of the Graduate School of
The University of Texas at Austin
in Partial Fulfillment
of the Requirements
for the degree of

Doctor of Philosophy

The University of Texas at Austin
May, 2023

To Jaynee, who unquestionably is the reason why this document exists.

Stranger Things at the LHC

Publication No. ____________________

Ryan Patrick Hannigan, Ph.D.
The University of Texas at Austin, 2023

Supervisor: Christina Markert

Among the most mysterious of the four fundamental forces is the strong nuclear force. Responsible for both the binding together of nucleons within an atom, as well as the

Contents

List of Figures viii

List of Tables xv

Chapter One: Introduction 1

1.1 What is fundamental? 1

Chapter Two: Experimental Apparatus 5

2.1 The LHC 5

2.2 The ALICE Detector 6

Chapter Three: Analysis Details 10

3.1 Dataset and event selection 10

3.2 Charged hadron track selection 11

3.3 Λ reconstruction 13

3.4 Reconstruction efficiency 20

3.5 Corrections to the correlation distributions 23

Chapter Four: Systematic uncertainties and cross-checks 38

4.1 Systematic uncertainties 38

4.2 Cross-checks 86

Bibliography 95

List of Figures

1.1 A diagram depicting the particles we currently believe are fundamental within the so-called "Standard Model" of particle physics. 2

1.2 A coffee cup with the Standard Model Lagrangian density printed on its side. Please ignore the "+ h.c." term following the $i\bar{\psi}\not{D}\psi$, it is the result of a small lapse in judgement from the mug makers. 3

2.1 A diagram depicting the LHC with its various main detectors shown underground. Illustration by Phillipe Mouche, from BBC News. 6

2.2 A 3-D schematic of the ALICE detector, with labels for all of the subdetectors. Note the humans-for-scale in the bottom left of the diagram. . 7

3.1 The p_{T} (left), φ (middle) and η (right) distributions for the trigger hadrons in the multiplicity range 0-20%. 12

3.2 The p_{T} (left), φ (middle) and η (right) distributions for the associated hadrons in the multiplicity range 0-20%. The dips observed in the φ distribution are due to the TPC sector boundaries. 13

3.3 A diagram depicting a typical V^0 decay with labels for the most important kinematic variables. The diagram was taken from [10]. 14

3.4 $n\sigma$ for protons (left) and pions (right) in the TPC detector as a function of p_T. 16

3.5 $n\sigma$ for protons (left) and pions (right) in the TOF detector as a function of p_T. 16

3.6 $n\sigma$ in TOF vs $n\sigma$ in TPC for protons (left) and pions (right). No contimatination is observed for both of the particle species. 17

3.7 Invariant mass distributions in the 0-20% (top), 20-50% (middle), and 50-80% (bottom) multiplicity bins for the Λ candidates which pass the selection criteria with $1.5 < p_{\mathrm{T}} < 2.5$ GeV/c (left) and $2.5 < p_{\mathrm{T}} < 4.0$ GeV/c (right). A Voigtian signal + straight-line background fit to the data is shown in blue, with just the background fit shown in red. For these plots, the Λs were only reconstructed in events with a trigger hadron. 19

3.8 Efficiency vs. p_T for trigger (left) and associated (right) hadrons. While they may look identical, the associated hadron efficiency is slightly lower due to the stricter selection criteria. 21

3.9 Efficiency vs. p_T (left) and η (right) for Λ reconstruction in each multiplicty bin, along with an integrated 0-100% point in red. 22

3.10 2-D non-acceptance corrected h-Λ angular correlations for the 0-20% (top), 20-50% (middle), and 50-80% (bottom) multiplicity bins for $1.5 < p_{\mathrm{T}} < 2.5$ GeV/c (left) and $2.5 < p_{\mathrm{T}} < 4.0$ GeV/c (right). 25

3.11 2-D non-acceptance corrected h-h angular correlations for the 0-20% (top), 20-50% (middle), and 50-80% (bottom) multiplicity bins for $1.5 < p_{\mathrm{T}} < 2.5$ GeV/c (left) and $2.5 < p_{\mathrm{T}} < 4.0$ GeV/c (right). 26

3.12 2-D mixed-event h-Λ angular correlations for the 0-20% (top), 20-50% (middle), and 50-80% (bottom) multiplicity bins for $1.5 < p_{\mathrm{T}} < 2.5$ GeV/c (left) and $2.5 < p_{\mathrm{T}} < 4.0$ GeV/c (right). The $Z_{\mathrm{vtx.}}$ bins are merged together for these plots. 27

3.13 2-D mixed-event h-h angular correlations for the 0-20% (top), 20-50% (middle), and 50-80% (bottom) multiplicity bins for $1.5 < p_{\mathrm{T}} < 2.5$ GeV/c (left) and $2.5 < p_{\mathrm{T}} < 4.0$ GeV/c (right). The $Z_{\mathrm{vtx.}}$ bins are merged together for these plots. 28

3.14 Invariant mass distribution of pπ pairs in the 20-50% multiplicity class. The signal region is shown in light green, and the sideband region is shown in light pink. The correlation distribution in the sideband region is used to remove the combinatorial background from the signal region. 30

3.15 The signal (top) and sideband (bottom) distributions $C_{\mathrm{signal}}^{\mathrm{h\text{-}p}\pi}$ and $C_{\mathrm{SB}}^{\mathrm{h\text{-}p}\pi}$ for the lower (left) and higher (right) associated p_{T} bins. All plots were generated in the 0-20% multiplicity class. 31

3.16 Demonstration of the track merging effect for h-Λ pairs, whereby we see a dip in the reconstructed distribution at small $\Delta\varphi$ and $\Delta\eta$ when compared to the MC ground truth (left). This dip is not present at large $\Delta\eta$ (right), but we also lose nearly the entirety of our near-side peak. 33

3.17 The reconstructed/ground truth ratios of the 2D $C(\Delta\varphi, \Delta\eta)$ distributions for h-(secondary pions) (left) and h-(primary pions) (right). The suppression at smaller $\Delta\varphi, \Delta\eta$ is clearly seen in the secondary case, but is not observable in the primary case, indicating a decay-length dependence. . . 34

3.18 The reconstructed and ground truth $\Delta\varphi$ distributions in the $-1.2 < \Delta\eta < 1.2$ region for h-(secondary pions) with $0.15 < p_{\mathrm{T}} < 2$ (left) and $2 < p_{\mathrm{T}} < 4$ (right). The suppression at smaller $\Delta\eta, \Delta\varphi$ is clearly seen in the higher momentum bin, but not present in the lower one. 35

3.19 The $\epsilon_{\mathrm{pair}}(\Delta\varphi, \Delta\eta)$ templates for the track merging correction in the lower ($1.5 < p_{\mathrm{T}} < 2.5$ GeV/c, left) and higher ($2.5 < p_{\mathrm{T}} < 4.0$ GeV/c, right) associated momentum bins. While it may be difficult to observe, the lower p_{T} bin has a minimum dip of around 0.84, whereas the higher p_{T} bin has a minimum dip of around 0.81, reflecting the p_{T} dependence discussed in this section. 37

4.1 The h-Λ $\Delta\varphi$ distributions within the 0-20% (top), 20-50% (middle) and 50-80% (bottom) multiplicity bins in the lower associated p_{T} bin for each of the signal region variations (left) with the ratios to the nominal distribution (right). 44

4.2 The h-Λ $\Delta\varphi$ distributions within the 0-20% (top), 20-50% (middle) and 50-80% (bottom) multiplicity bins in the higher associated p_{T} bin for each of the signal region variations (left) with the ratios to the nominal distribution (right). 45

4.3 The h-Λ $\Delta\varphi$ distributions within the 0-20% (top), 20-50% (middle) and 50-80% (bottom) multiplicity bins in the lower associated p_{T} bin for each of the sideband region variations (left) with the ratios to the nominal distribution (right). 46

4.4 The h-Λ $\Delta\varphi$ distributions within the 0-20% (top), 20-50% (middle) and 50-80% (bottom) multiplicity bins in the higher associated p_{T} bin for each of the sideband region variations (left) with the ratios to the nominal distribution (right). 47

4.5 The h-Λ $\Delta\varphi$ distributions within the 0-20% (top), 20-50% (middle) and 50-80% (bottom) multiplicity bins in the lower associated p_{T} bin for each of the PID cut variations (left) with the ratios to the nominal distribution (right). 48

4.6 The h-Λ $\Delta\varphi$ distributions within the 0-20% (top), 20-50% (middle) and 50-80% (bottom) multiplicity bins in the higher associated p_{T} bin for each of the PID cut variations (left) with the ratios to the nominal distribution (right). 49

4.7 Barlow check for the signal (left), sideband (middle), and PID (right) variations in the 0-20% multiplicity bin. The red lines represent $N\sigma_{RB} = \pm1$, and if the majority of the points fall within the red lines (across all $\Delta\varphi$, multiplicty and p_{T} bins), they are excluded from the systematic uncertainty calculation. 50

4.8 A visual depiction of the final systematic errors for the h-Λ $\Delta\varphi$ distributions for each multiplicity bin in the low (left) and high (right) associated p_{T} bins. The total systematic error is shown in black. 52

4.9 Visual depiction of the multiplicity-uncorrelated systematic errors for the h-Λ $\Delta\varphi$ distributions for each multiplicity bin in the low (left) and hig (right) associated p_{T} bins, along with the total systematic error shown in black. 53

4.10 The v_2 values for identified hadrons as a function of p_{T}, taken from [20]. 56

4.11 The published [18] p_{T} spectra for Λ baryons (top) and charged hadrons ($\approx$ pions) (bottom), used to compute the weighted average of the v_2 coefficients across the wide momentum bins used in this analysis. 57

4.12 Examples of the underlying event fit using the v_2-based procedure for the h-Λ (left) and h-h (right) $\Delta\varphi$ distributions in the 0-20% multiplicity bin in the higher associated p_{T} bin. 58

4.13 The h-Λ (left) and h-h (right) $\Delta\varphi$ distributions in the 0-20% multiplicity bin and higher p_{T} bin at small and large values of $\Delta\eta$, with the UE fit using the v_2-based procedure shown in blue. The fits are in good agreement with data in both cases. 58

4.14 The final per-trigger h-Λ $\Delta\varphi$ correlation distributions with the full double Gaussian fit for the 0-20% (top), 20-50%(middle) and 50-80% (bottom) multiplicity bins in the lower (left) and higher (right) associated p_{T} bins. The UE fit is also shown as a dashed line. 62

4.15 The final per-trigger h-h $\Delta\varphi$ correlation distributions with the full double Gaussian fit for the 0-20% (top), 20-50%(middle) and 50-80% (bottom) multiplicity bins in the lower (left) and higher (right) associated p_{T} bins. The UE fit is also shown as a dashed line. 63

4.16 The final per-trigger h-Λ $\Delta\varphi$ correlation distributions with the von Mises fit for the 0-20% (top), 20-50%(middle) and 50-80% (bottom) multiplicity bins in the lower (left) and higher (right) associated p_{T} bins. The UE fit with v_2 contribution is also shown as a dashed line. 66

4.17 The final per-trigger h-h $\Delta\varphi$ correlation distributions with the von Mises fit for the 0-20% (top), 20-50%(middle) and 50-80% (bottom) multiplicity bins in the lower (left) and higher (right) associated p_{T} bins. The UE fit with v_2 contribution is also shown as a dashed line. 67

4.18 The Barlow check for the yield extraction procedure in the 0-20% multiplicity bin for the lower (left) and higher (right) associated p_{T} bins. The red lines represent $N_{\sigma_{RB}} = \pm 1$, and if the majority of the points from a given procedure fall within these lines (across all multiplicity and momentum bins), the procedure is excluded from the systematic uncertainty calculation. 68

4.19 The deviation from the nominal h-Λ per-trigger yields for each yield extraction procedure variation (post Barlow check) in each kinematic region for the 0-20% (top), 20-50% (middle) and 50-80% (bottom) multiplicity bins in the lower (left) and higher (right) associated p_{T} bins. The systematic uncertainty for the yield extraction procedure is calculated by taking the RMS of these deviations for each kinematic region. 71

4.20 The deviation from the nominal h-h per-trigger yields for each yield extraction procedure variation (post Barlow check) in each kinematic region for the 0-20% (top), 20-50% (middle) and 50-80% (bottom) multiplicity bins in the lower (left) and higher (right) associated p_{T} bins. The systematic uncertainty for the yield extraction procedure is calculated by taking the RMS of these deviations for each kinematic region. 72

4.21 The Von Mises (left) and Gaussian (right) dist with $\kappa = 1$ and $\sigma = 1$. Note that the von Mises distribution does not approach zero at large x, while the Gaussian does. 74

4.22 The p_{T} distributions of Λ candidates with and without the TOF signal requirement. The mean p_{T} of the Λ candidates with daughters that generate a TOF signal is nearly 10% higher than those without this requirement, which indicates that the requiring a TOF signal for the Λ daughters introduces a physical bias. 75

4.23 The resulting von Mises fits and extracted jet widths after the signal, sideband and PID cut variations are applied to the h-Λ $\Delta\varphi$ distributions. 78

4.24 The resulting h-Λ (top) and h-h (bottom) von Mises fits and extracted jet widths in each multiplicity and momentum bin after each variation of the fitting procedure. 79

4.25 Barlow check for the width extraction procedure for the signal (left), sideband (middle), and PID (right) variations in the 20-50% multiplicity bin. The red lines represent $N\sigma_{RB} = \pm 1$, and if the majority of the points fall within the red lines (across all p_{T} and multiplicity bins), they are excluded from the width systematic uncertainty calculation. 81

4.26 Final systematic errors for the h-Λ $\Delta\varphi$ near-side (top) and away-side (bottom) width extraction for each multiplicity bin in the lower (left) and higher (right) associated p_{T} bins. 83

4.27 Final systematic errors for the h-h $\Delta\varphi$ near-side (top) and away-side (bottom) width extraction for each multiplicity bin in the lower (left) and higher (right) associated p_{T} bins. 84

4.28 The resulting h-Λ (top) and h-h (bottom) von Mises fits and extracted jet widths in the 20-50% multiplicity bin for each momentum bin after random variations of the individual $\Delta\varphi$ bins within the topological selection (h-Λ) and tracking efficiency (h-h) uncertainties from Table 4.1. 84

4.29 The reconstructed (pink) and ground-truth (blue) h-Λ $\Delta\varphi$ distributions in the lower (top) and higher (bottom) associated p_{T} bins, along with a (reconstructed)/(ground-truth) ratio and straight-line fit with errors shown as dashed lines. The ratio is consistent with unity, and thus the corrections applied to the h-Λ distributions are valid. 88

4.30 The reconstructed (pink) and ground-truth (blue) h-h $\Delta\varphi$ distributions in the lower (top) and higher (bottom) associated p_{T} bins, along with a (reconstructed)/(ground-truth) ratio and straight-line fit with errors shown as dashed lines. Again, the ratio is consistent with unity, and thus the corrections applied to the h-h distributions are valid. 89

4.31 A diagram showing the effect of multiple triggers on the per-trigger pair-wise yield. In the first event, there is a single trigger with three associated particles, so the pair-wise yield is equal to the number of associated particles. In the second event, there are two triggers with three associated particles, so the pair-wise yield is twice the number of associated particles. 90

4.32 A log-plot showing the number of triggers per event across the entire data sample. Only a small fraction of events have at least a single trigger, and of those events, only a small fraction have more than one trigger. 91

4.33 The per-trigger h-Λ (top) and h-h (middle) $\Delta\varphi$ distribution comparison between using a single trigger (closed points) and all triggers (open points) in a given event, along with the (single trigger)/(all trigger) distribution ratio (bottom), for the 0-20% (left), 20-50% (center) and 50-80% (bottom) multiplicity bins in the associated momentum range $2.0 < p_{\mathrm{T}} < 4.0$ GeV/c. The distributions are nearly identical up to a ≈ 0.95 scale factor, which is constant as a function of multiplicity. 92

4.34 Comparison of the the dihadron $\Delta\varphi$ correlations between the ϕ and Λ analyses for the 0-20% (left), 20-50% (middle) and 50-80% (right) multiplicity bins, taken in the $2.0 < p_{\mathrm{T}} < 4.0$ GeV/c associated momentum range. They are functionally identical for all multiplicity bins. 94

List of Tables

3.1 Number of events passing our criteria for each multiplicity bin considered. Here Z_{vtx} refers to the position of the PV along the beam (z) axis. 11

3.2 The track quality cuts applied to the trigger hadrons in this analysis. . . 12

3.3 The ALICE standard track quality cuts for primary charged hadrons, used for the selection of the associated hadrons in this analysis. 13

3.4 The track quality cuts applied to both the daughter proton and pion tracks used to reconstruct Λ candidates. These cuts are intentionally less strict than those applied to the trigger and associated hadrons as the daughter tracks are reconstructed from secondary particles. 15

3.5 Topological selection criteria applied to Λ candidates. 18

4.1 The systematic uncertainties for the $\Delta\varphi$ distributions which are not directly calculated in this thesis, instead taken from previous analyses using the same particle species and collision system [15], [17]–[19]. Each source of uncertainty is verified to be independent of multiplicity, but the Λ material budget and topological selection uncertainties exhibit a small dependence on p_{T}. 41

4.2 The variations of the Λ invariant mass signal region considered for this analysis. 41

4.3 The variations of the Λ invariant mass sideband region considered for this analysis. Note that the "shifted left" sideband falls on the opposite (left) side of the signal region. 42

4.4 The variations of the Λ daughter PID cuts considered for this analysis. The "require TOF" variation requires a TOF hit for both the proton and pion, but maintains the nominal values for $|n\sigma_{\mathrm{TPC,\ TOF}}|$. 43

4.5 The final systematic uncertainties (in percentages) from the h-Λ $\Delta\varphi$ distribution generation for each multiplicity and associated p_{T} bin. 51

4.6 v_2 values used in this analysis for each associated p_{T} bin. The values were calculated as the weighted average of published p_{T}-differential v_2 measurements with the published p_{T} spectra, taken across the entire associated p_{T} range. 55

4.7 Final systematic errors (in %) for the per-trigger h-Λ yields in each kinematic region, multiplicity and momentum bin. 69

4.8 Final systematic errors (in %) for the h-h per-trigger yields in each kinematic region, multiplicity and momentum bin. 69

4.9 Final multiplicity-uncorrelated systematic errors (in %) for the per-trigger h-Λ yields in each kinematic region, multiplicity and momentum bin, used for calculating errors associated with quantities describing trends versus multiplicity (slopes and percent changes). 70

4.10 Final multiplicity-uncorrelated systematic errors (in %) for the h-h per-trigger yields in each kinematic region, multiplicity and momentum bin, used for calculated errors associated with quantities describing trends versus multiplicity (slopes and percent changes). 70

4.11 The final systematic errors from the h-Λ $\Delta\varphi$ near-side (NS) and away-side (AS) width extraction for each multiplicity bin in the lower (top) and higher (bottom) associated p_{T} bins. The total systematic error is calculated by adding each systematic error in quadrature. 82

4.12 The final systematic errors from the h-h $\Delta\varphi$ near-side (NS) and away-side (AS) width extraction for each multiplicity bin in the lower (top) and higher (bottom) associated p_{T} bins. The total systematic error is calculated by adding each systematic error in quadrature. 82

4.13 The final systematic uncertainties for the h-Λ $\Delta\varphi$ distributions, the per-trigger jet and UE yields, and the jet widths in all multiplicity and associated momentum bins. The fraction of the systematic uncertainty which is uncorrelated with multiplicity is reported separately in parentheses for the extracted yields. The low (high) momentum bin is such that $1.5 < p_T^{\mathrm{assoc.}} < 2.5$ GeV/c ($2.5 < p_T^{\mathrm{assoc.}} < 4.0$ GeV/c). 85

4.14 The final systematic uncertainties for the h-h $\Delta\varphi$ distributions, the per-trigger jet and UE yields, and the jet widths in all multiplicity and associated momentum bins. The fraction of the systematic uncertainty which is uncorrelated with multiplicity is reported separately in parentheses for the extracted yields. The low (high) momentum bin is such that $1.5 < p_T^{\mathrm{assoc.}} < 2.5$ GeV/c ($2.5 < p_T^{\mathrm{assoc.}} < 4.0$ GeV/c). 85

Chapter One: Introduction

The purpose of this chapter is to transform a scientifically literate reader who may be vaguely familiar with the idea of a “quark” into one who can understand the motivation and techniques behind the analysis presented in the rest of this thesis. If you are an extremely educated physicist who regularly performs lattice quantum chromodynamics calculations in their head, I would also encourage you to read this chapter it its entirety as it may contain egregious errors that need to be corrected.

1.1 What is fundamental?

The answer to the question “What are the fundamental building blocks of our universe?” has changed drastically over the course of human history. The idea that all matter is composed of smaller, uncuttable pieces has been around since 5th century BCE when Greek philosophers Democritus and Leucippus first introduced the concept of an atom [1]. While this idea was mostly motivated by philosophical reasoning, it was later adopted by the English scientist John Dalton in the 19th century to explain the results of his chemical experiments, where he found that chemical elements always combined with each other by discrete units of mass [2]. However, everything changed around the turn of the 20th century when scientists like Rutherford and Chadwick determined that the supposedly indivisible atom was composed of even smaller particles, eventually named protons and neutrons [3], [4]. The notion that protons and neutrons were unbreakable was relatively short lived, as not even half a century later the deep inelastic scattering experiments performed by Kendall, Friedman and Taylor [5]–[7] revealed that protons (and subsequently neutrons) were actually composed of even smaller particles, eventually dubbed “partons”. [8]. This discovery was one of the largest contributing factors to the creation of the so-called Standard Model of particle physics, a theory which describes all of the fundamental particles and the way in which they interact with each other. A diagram of those fundamental particles can be seen in Figure 1.1. It should be noted that all of the particles labeled as quarks and leptons – collectively as “fermions” – have corresponding anti-particles with opposite electric charge. The equation that describes all of these

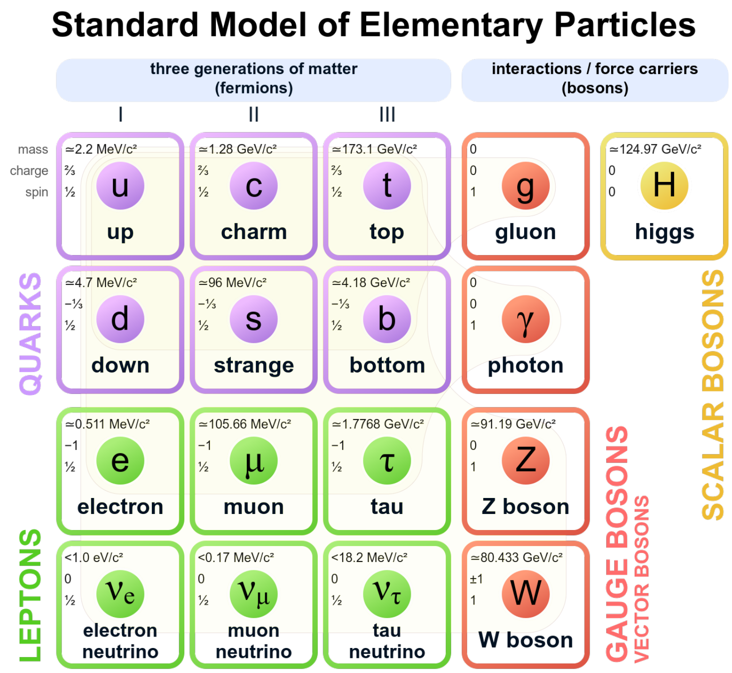

Figure 1.1: A diagram depicting the particles we currently believe are fundamental within the so-called "Standard Model" of particle physics.

particles and their interactions, often incorrectly[1] referred to as the "Standard Model Lagrangian", can be compactified into a relatively palatable form that can easily fit on a coffee cup like the one shown in Figure 1.2.

While this equation may appear brief[1], it can be used to completely describe three of the four fundamental forces of nature:

1. The Electromagnetic Force, which is responsible for the electrons pushing against each other to keep you from falling through your chair,

2. The Weak Nuclear Force, which is responsible for the initiating the nuclear fusion reactions that fuel our sun, and

[1]It is "incorrect" because this is technically a Lagrangian density (i.e. Lagrangian per unit volume), but as it is usually integrated over all space the distinction is mostly irrelevant.

[1]Here "brief" is in the eye of the beholder, but certainly its brevity is misleading as even in the first line the $F_{\mu\nu}$ refers to three completely different gauge field tensors with their indices fully contracted...

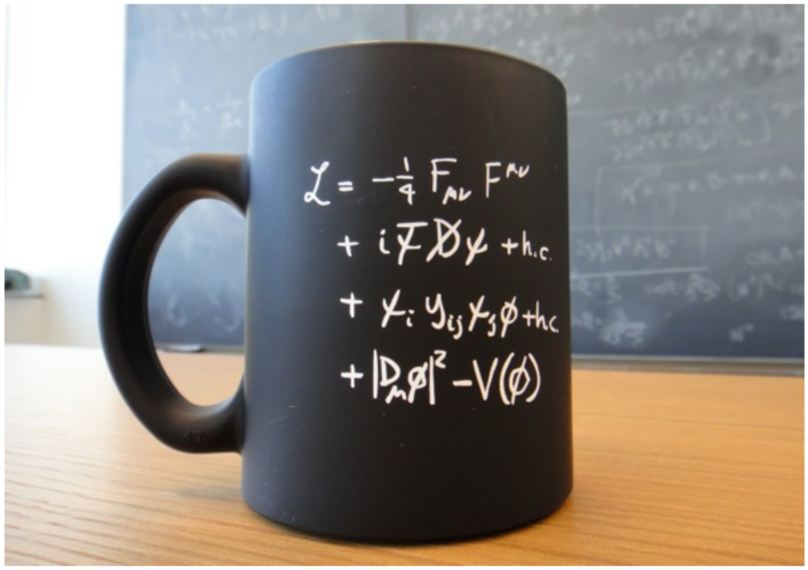

Figure 1.2: A coffee cup with the Standard Model Lagrangian density printed on its side. Please ignore the "+ h.c." term following the $i\bar{\psi}\not{D}\psi$, it is the result of a small lapse in judgement from the mug makers.

3. The Strong Nuclear Force, which is responsible for holding quarks and gluons together in bound stands known as hadrons, like the protons and neutrons that make up everyday matter.

The only fundamental force missing from this list is the Gravitational Force, which is described by a completely separate set of equations[2]

Each of the three forces that are described within the Standard Model are mediated by different gauge bosons. For example, the electromagnetic force is mediated by the boson known as the photon, the weak nuclear force is mediated by the W and Z bosons, and the strong nuclear force is mediated by bosons known as gluons. In this thesis we will be primarily focusing on the Strong Nuclear Force, which acts solely on particles with color charge – an intrinsic property of quarks and gluons. The "color" charges are red, green, and blue with antio

Even though each of the electromagnetic, weak and strong forces can be described using the Standard Model Lagrangian, the way in which they appear within the

[2]Specifically, the Einstein Field Equations, $G_{\mu\nu} + \Lambda g_{\mu\nu} = \kappa T_{\mu\nu}$, but this is the thesis of a particle physicist so gravity is taboo.

equation is not easy to determine. For example, the electromagnetic force actually corresponds to line 1

Chapter Two: Experimental Apparatus

As this thesis is focused on the physics of heavy-ion collisions, it stands to reason that the data analyzed in this thesis was gathered using the only detector along the LHC dedicated to studying such collisions: the ALICE detector. In this chapter, a brief synopsis of the LHC will be provided, followed by a much more detailed overview of the ALICE detector and its corresponding sub-detectors.

2.1 The LHC

Located along the Swiss-French border near Geneva, Switzerland, the Large Hadron Collider (LHC) is the largest particle accelerator on the planet. At a circumference of 27 kilometers, its tunnels lie almost 200 meters beneath the surface of the earth. Inside the tunnels are two high-energy particle beams pointing in opposite directions, with the beam pipes being kept inside of an ultra-high vacuum. The particles inside the beam are guided by a multitude of superconducting magnets: 393 quadrapole magnets keep the beam focused, while 1232 dipole magnets bend the particles along the circular path. The beams are designed to collide at four intersection points along the LHC, each with a corresponding detector surrounding the collision points: (1) ALICE, which specializes in heavy-ion collisions; (2) ATLAS, which specializes in studying high-p_T particles produced in pp collisions, (3) CMS, which TODO and (4) LHCb, which is designed to study CP violations through measurements of B mesons at forward rapidity. A diagram of the LHC with these four intersection points can be seen in Figure 2.1.

Currently, the highest center of mass energies achieved for each of the main collision systems are $\sqrt{s} = 13$ TeV for pp, $\sqrt{s} = 7$ TeV for p-Pb and $\sqrt{s} = 5.02$ TeV for Pb-Pb. The LHC underwent a long shutdown from XXXX to YYYY, in order to upgrade the beam luminosity and COM energies. The projected final COM energies for each collision system will be ...

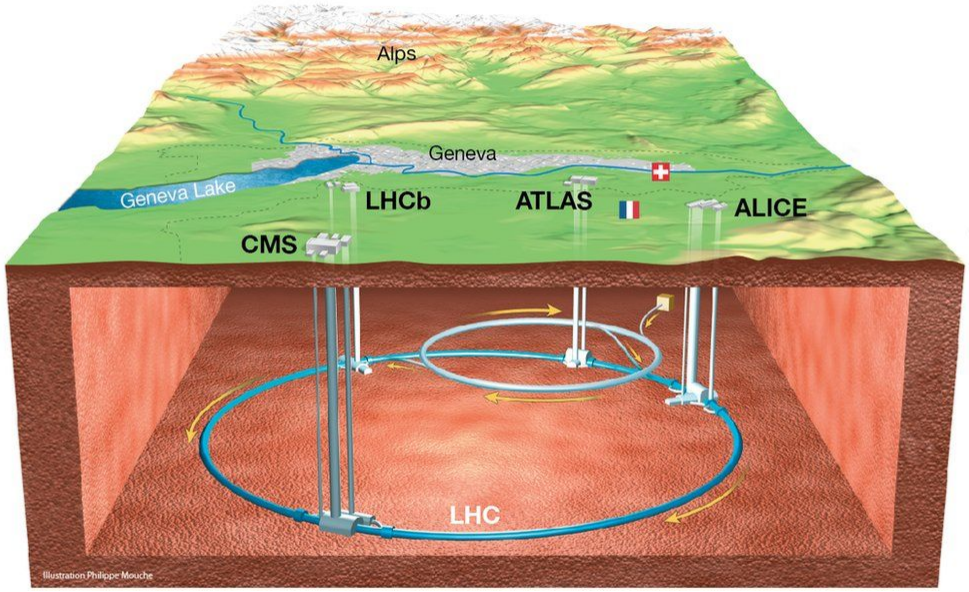

Figure 2.1: A diagram depicting the LHC with its various main detectors shown underground. Illustration by Phillipe Mouche, from BBC News.

2.2 The ALICE Detector

The detector used by the ALICE collaboration, unsurprisingly known as the ALICE detector, has the primary focus of investigating the physical properties of the strongly interacting quark-gluon plasma created during heavy-ion collisions. Building the detector was a massive effort, requiring the help from over 1000 people from 105 institutes in 30 different countries. The detector itself is also massive, weighing in at around 10,000 tons and spanning 26 meters in length with a 16-meter height and width. It is composed of 18 sub-detector systems, all of which work together to help reconstruct the event. A diagram of the detector with its corresponding sub-detector systems can be seen in in Figure 2.2. As the primary focus of the ALICE detector is to study heavy-ion collisions, all of its components must work together to reconstruct very high multiplicity events.

2.2.1 The Inner Tracking System

The Inner Tracking System (ITS) is the inner-most component of the ALICE detector, lying closest to the beam pipe. It is composed of six cylindrical layers of silicon

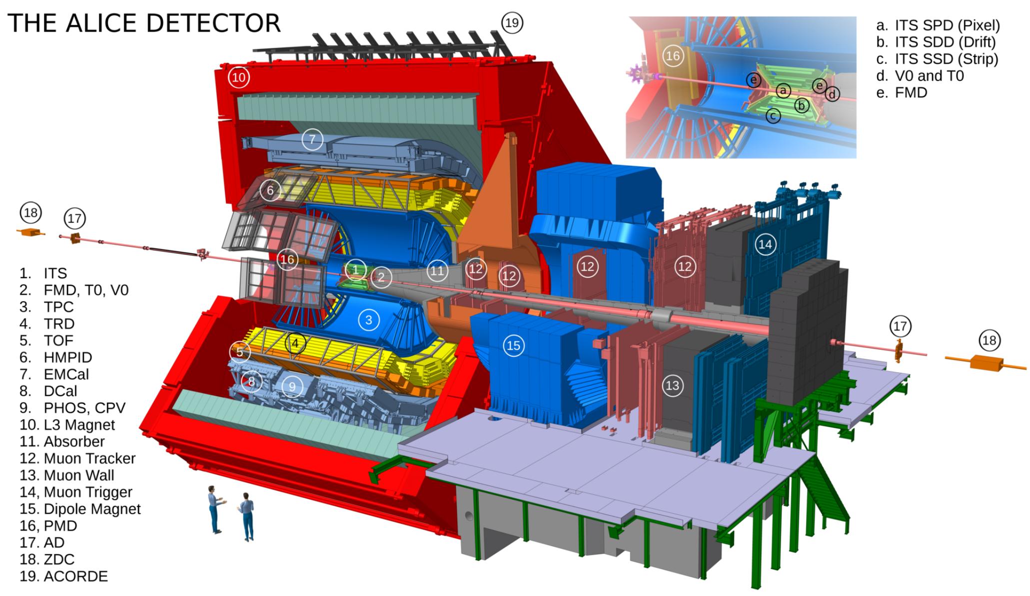

Figure 2.2: A 3-D schematic of the ALICE detector, with labels for all of the sub-detectors. Note the humans-for-scale in the bottom left of the diagram.

detectors that are coaxial with the beam pipe and cover the pseudorapidity range $|\eta| \leq 0.9$. The distance from the beam line varies from 3.9 cm for the first layer to 43 cm for the sixth layer. The ITS uses different types of silicon detectors for each layer: Silicon Pixel Detectors (SPD) for the first and second layers, Silicon Drift Detectors (SDD) for the third and fourth layers, and double sided Silicon Strip Detectors (SSD) for the fifth and sixth layers. Because of its proximity to the interaction point, the ITS is invaluable for reconstructing both primary and secondary vertices and enhancing the tracking capabilities of the ALICE detector near the interaction point. Moreover, the ITS can also track particles that are not detected or missed by the external barrel detector due to acceptance limitations and momentum cutoff.

2.2.1.1 ITS Upgrade

The LHC underwent a fairly substantial upgrade to the beam luminosity from X to Y. In order to utilize all of the The writer of this thesis was the main reason why the ITS Upgrade actually finished, as he is the smartest person of all time and actually hand built the entire thing.

2.2.2 The V0 Detector

V0 is made of two arrays of scintillator counters set on both sides of the ALICE interaction point, and called V0-A and V0-C. The V0-C counter is located upstream of the dimuon arm absorber and cover the spectrometer acceptance while the V0-A counter will be located at around 3.5 m away from the collision vertex, on the other side. It is used to estimate the centrality of the collision by summing up the energy deposited in the two disks of V0. This observable scales directly with the number of primary particles generated in the collision and therefore to the centrality. V0 is also used as reference in Van Der Meer scans that give the size and shape of colliding beams and therefore the luminosity delivered to the experiment.

2.2.3 The Time Projection Chamber

The largest component of the ALICE detector is know nas the Time Projection Chamber (TPC). The TPC is a gas-filled volume with The ALICE Time Projection Chamber (TPC) is a large volume filled with a gas as detection medium and is the main particle tracking device in ALICE.[19][20] Charged particles crossing the gas of the TPC ionize the gas atoms along their path, liberating electrons that drift towards the end plates of the detector. The characteristics of the ionization process caused by fast charged particles passing through a medium can be used for particle identification. The velocity dependence of the ionization strength is connected to the well-known Bethe-Bloch formula, which describes the average energy loss of charged particles through inelastic Coulomb collisions with the atomic electrons of the medium. Multiwire proportional counters or solid-state counters are often used as detection medium, because they provide signals with pulse heights proportional to the ionization strength. An avalanche effect in the vicinity of the anode wires strung in the readout chambers, gives the necessary signal amplification. The positive ions created in the avalanche induce a positive current signal on the pad plane. The readout is performed by the 557 568 pads that form the cathode plane of the multi-wire proportional chambers (MWPC) located at the end plates. This gives the radial distance to the beam and the azimuth. The last coordinate, z along the beam direction, is given by the drift time. Since energy-loss fluctuations can be considerable, in general many pulse-height measurements are performed along the particle track in order to optimize the resolution of the ionization measurement. Almost all of the TPC's volume is sensitive to the traversing charged particles, but it features a minimum material budget. The straightforward pattern recognition (continuous tracks) make TPCs the perfect choice for high-multiplicity environments, such as in heavy-ion collisions, where thousands of particles have to be tracked simultaneously. Inside the ALICE TPC, the ionization strength of all tracks is sampled up to 159 times, resulting in a resolution of the ionization measurement as good as 5

2.2.4 The Electromagnetic Calorimeter

The EMCal is a lead-scintillator sampling calorimeter comprising almost 13,000 individual towers that are grouped into ten super-modules. The towers are read out by wavelength-shifting optical fibers in a shashlik geometry coupled to an avalanche photodiode. The complete EMCal will contain 100,000 individual scintillator tiles and 185 kilometers of optical fiber, weighing in total about 100 tons. The EMCal covers almost the full length of the ALICE Time Projection Chamber and central detector, and a third of its azimuth placed back-to-back with the ALICE Photon Spectrometer – a smaller, highly granular lead-tungstate calorimeter. The super-modules are inserted into an independent support frame situated within the ALICE magnet, between the time-of-flight counters and the magnet coil. The support frame itself is a complex structure: it weighs 20 tons and must support five times its own weight, with a maximum deflection between being empty and being fully loaded of only a couple of centimeters. Installation of the eight-ton super-modules requires a system of rails with a sophisticated insertion device to bridge across to the support structure. The Electro-Magnetic Calorimeter (EM-Cal) will add greatly to the high momentum particle measurement capabilities of ALICE.[26] It will extend ALICE's reach to study jets and other hard processes.

Chapter Three: Analysis Details

This chapter builds upon the analysis overview presented in the previous chapter by providing a much more detailed description of each component of the analysis. These components can be summarized as follows. First, a high-quality data sample of p–Pb collisions is selected, with events further differentiated by their multiplicity. Then, quality tracks are selected for the trigger and associated charged hadrons, and the Λ baryons are reconstructed from lower quality tracks using their characteristic decay topology. These Λ daughter tracks are identified as protons or pions using information from the TPC and TOF detectors. Within a given event, the trigger hadrons are then combined with either the associated charged hadrons or the Λ candidates to form pairs, where a distribution of their relative azimuthal angle ($\Delta\varphi \equiv \varphi_{trig.} - \varphi_{assoc.}$) and pseudorapidity ($\Delta\eta \equiv \eta_{trig.} - \eta_{assoc.}$) is filled for each pair. These h-Λ and h-h angular distributions are then corrected for a laundry list of detector effects using both data- and MonteCaro-driven methods. Further corrections are applied to the h-Λ distributions to account for effects like the combinatorial background associated with the Λ reconstruction and the two-track merging effect, whereby one of the daughter tracks gets merged with the trigger hadron track, causing a h-Λ pair deficit at small angles. Once all corrections are applied, the h-Λ and h-h distributions are finalized and ready for the extracting of the many observables discussed at the end of the previous chapter.

3.1 Dataset and event selection

3.1.1 Dataset

Every event in this analysis was a p–Pb collision at $\sqrt{s_{\mathrm{NN}}} = 5.02$ TeV with data collected by the ALICE detector during the 2016 LHC run. This analysis uses the data from these runs with the “FAST” reconstruction, meaning the data was taken without the ITS’s SDD subdetector due to issues with readout during this period. The total number of events (prior to any selection) is roughly 400 million. For the the efficiency studies, the analysis was performed using a standard purpose MC-generated production anchored to the dataset using the DPMJET [9] event generator. This production consists of around 400 million minimum bias events, which is roughly equivalent to data.

3.1.2 Event Selection

Events are selected by requiring the location of the primary collision interaction point (called the "primary vertex" or PV) to be no more than 10 cm from the center of the detector along the beam axis or "z"-direction. Furthermore, every event is required to have at least three reconstructed tracks that contributed to the reconstruction of the PV. This reduces the total number of events considered to approximately 350 million events, and a summary of the effects of these selection criteria can be seen in Table 3.1. The events are further separated into three charged particle multiplicity classes (0-20%, 20-50% and 50-80%) based off event activity in the forward-rapidity V0A detector.

Table 3.1: Number of events passing our criteria for each multiplicity bin considered. Here Z_{vtx} refers to the position of the PV along the beam (z) axis.

Multiplicity	Total evts.	Has 3 tracks	$\lvert Z_{vtx}\rvert < 10$cm + 3 tracks	% Pass
0-20%	1.0E08	1.0E08	0.8E08	87%
20-50%	1.6E08	1.6E08	1.3E08	86%
50-80%	1.6E08	1.6E08	1.3E08	86%

3.2 Charged hadron track selection

3.2.1 Trigger track cuts

For any two-particle correlation analysis, the selection criteria of the trigger hadron is of utmost importance as any geometric biases introduced by the trigger selection could be reflected in the final correlation distributions. However, correlation analyses generally require large statistics, thus the selection criteria shown in Table 3.2 are applied to ensure the quality of the trigger hadron track while maximizing the statistics of the analysis. Furthermore, the trigger hadron tracks are required to be

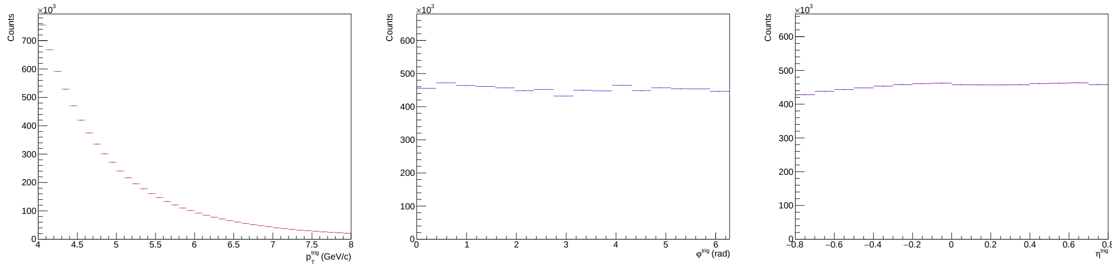

Figure 3.1: The p_{T} (left), φ (middle) and η (right) distributions for the trigger hadrons in the multiplicity range 0-20%.

at midrapidity ($|\eta| < 0.8$) and have high[1] momentum with $4.0 < p_{\mathrm{T}}^{\text{trig.}} < 8.0$ GeV/c, as the trigger is meant to serve as a proxy for a jet axis. Plots of the p_{T}, φ and η distributions for the trigger hadrons that pass these cuts in the 0-20% multiplicity bin can be seen in Figure 3.1.

Table 3.2: The track quality cuts applied to the trigger hadrons in this analysis.

Selection criterion	Value
TPC clusters	≥ 50
χ^2 per TPC cluster	< 4
Fraction of shared TPC clusters	< 0.4
DCA_{xy}	< 2.4 cm
DCA_{z}	< 3.2 cm
Accept kink daughters	No

3.2.2 Associated hadron track cuts

To keep the results of this analysis more comparabile to previous measurements of the $\Lambda/\pi \approx \Lambda/\mathrm{h}$ ratio, the selection criteria for the associated hadrons are more strict than those for the trigger hadrons as the associated hadrons are meant to be "primary", meaning they did not originate from a weak decay. All associated hadrons are required to meet the ALICE standard track quality cuts for primary charged hadrons described in Table 3.3. Furthermore, the associated hadrons are selected only at midrapidity ($|eta| < 0.8$) in the momentum region $1.0 < p_{\mathrm{T}} < 4.0$GeV/$c$, with further binning

[1] "High" in this case means high enough to guarantee the hadron is produced close (in $\Delta\varphi\Delta\eta$-space) to a jet axis.

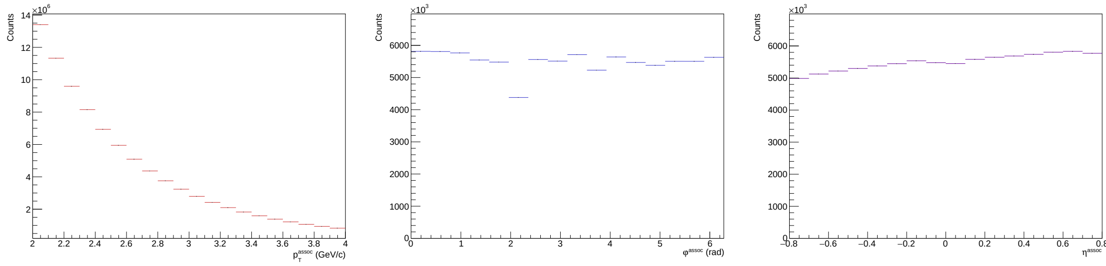

Figure 3.2: The p_{T} (left), φ (middle) and η (right) distributions for the associated hadrons in the multiplicity range 0-20%. The dips observed in the φ distribution are due to the TPC sector boundaries.

performed offline. The p_{T}, φ and η distributions for the associated hadrons that pass these cuts in the 0-20% multiplicity bin can be seen in Figure 3.2.

Table 3.3: The ALICE standard track quality cuts for primary charged hadrons, used for the selection of the associated hadrons in this analysis.

Selection criterion	Value
Crossed rows in TPC	≥ 80
Crossed rows/findable clusters in TPC	> 0.8
TPC clusters	≥ 80
ITS clusters	≥ 3
χ^2 per TPC cluster	< 4
χ^2 per ITS cluster	< 36
TPC and ITS refit required	Yes
DCA$_{xy}$	$< 0.0105 + 0.0350/p_{\mathrm{T}}^{1.1}$ cm
DCA$_z$	< 2 cm

3.3 Λ reconstruction

3.3.1 Characteristic V^0 decay topology

The Λ candidates in this analysis are reconstructed using their characteristic "V"-shaped decay topology, which is seen in the detector as two oppositely charged tracks originating from a common vertex which is sufficiently displaced from the PV (called the "secondary vertex" or SV). Such particles capable of being reconstructed via this topology are called "V^0"s: the V describing the decay shape and the 0 indicating that the particle is neutral. A diagram depicting a typical V^0 decay is shown in Figure 3.3, with labels given for the most relevant kinematic variables.

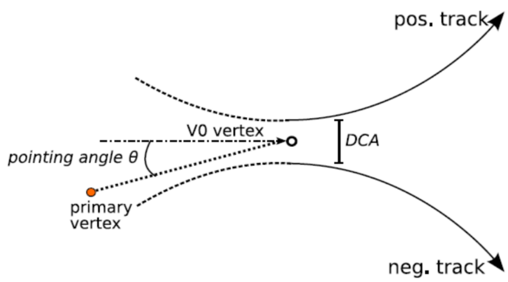

Figure 3.3: A diagram depicting a typical V^0 decay with labels for the most important kinematic variables. The diagram was taken from [10].

The first and most important of these variables is the distance of closest approach (DCA) between the two tracks. This DCA needs to be small enough (relative to the tracking resolution) to ensure that the tracks originated from a common vertex. Another important variable is the transverse decay length of the V^0, which is the distance between the PV and the SV measured in the xy-plane. The importance of this variable is twofold: if the decay length is too small, then it may not even be possible to resolve the SV from the PV, plus it allows for the distinction between V^0s of differing decay lengths. The final relevant variable is the cosine of the pointing angle, which is the angle between the momentum vector of the V^0 and the vector pointing from the PV to the SV. As V^0 candidates are generally required to be sufficiently collimated to ensure that the V^0 originated from the PV, the cosine of the pointing angle is usually close to unity.

Using these variables, a list of likely V^0 candidates is generated for each event, from which further cuts are applied to maximize the likelihood of the candidate being a true Λ baryon. These cuts are summarized in the following section. There is also another technique for Λ reconstruction whereby all oppositely charged proton-pion pairs are combined to form Λ candidates, which is explored in more detail in Chapter 4. However, due to the large combinatorial background associated with this technique, the V^0 method described above is nominal for this analysis.

3.3.2 Λ daughter proton and pion track cuts

Because of the longer decay length of the Λ ($c\tau \approx 10$ cm), the corresponding daughter proton and pion tracks generally have fewer hits in both the ITS and TPC, resulting in "lower quality" track parameters. Because of this, the cuts applied to the daughter tracks used to reconstruct Λ candidates are the least strict of all the track quality cuts in this analysis and are summarized in Table 3.4. The daughter proton and pion are also required to be at midrapidity ($|\eta| < 0.8$) and have a minimum p_{T} of $p_{\mathrm{T}} > 0.15$ GeV/c.

Table 3.4: The track quality cuts applied to both the daughter proton and pion tracks used to reconstruct Λ candidates. These cuts are intentionally less strict than those applied to the trigger and associated hadrons as the daughter tracks are reconstructed from secondary particles.

Selection criterion	Value
TPC refit required	Yes
Crossed rows in TPC	≥ 70
Crossed rows/findable clusters in TPC	> 0.8

Following the particle identification procedure outlined in Sections **??** and **??**, the daughter proton and pion tracks are required to pass the following PID cuts using both the TPC and TOF detectors:

- $|n\sigma_{\mathrm{TPC},p}| < 2$
- $|n\sigma_{\mathrm{TPC},\pi}| < 3$
- $|n\sigma_{\mathrm{TOF},p}| < 2$ (if signal exists)
- $|n\sigma_{\mathrm{TOF},\pi}| < 3$ (if signal exists)

The values of these cuts were chosen to maximize the Λ signal while avoiding contamination from other particle species. The parenthetical "if signal exists" means that the TOF PID cut is only applied if the track has a TOF signal. Due to the large distance between the TOF detector and the PV, many lower momentum tracks are deflected by the magnetic field before reaching the TOF detector, resulting in no signal. Excluding such tracks results in a more pure sample of protons and pions, at the cost of a much lower number of Λ candidates. While such a cost is not acceptable for the nominal analysis, the effect of excluding these tracks is investigated in Chapter 4. The $n\sigma$ distributions for both the TPC and TOF detectors of the daughter proton and pion tracks that pass the aforementioned quality cuts are shown in Figure 3.4 and Figure 3.5, respectively. To check for contamination from other particle species, the TOF and TPC information is combined to form a $n\sigma_{\text{TOF}}$ vs $n\sigma_{\text{TPC}}$ plot, which is shown for both the protons and pions in Figure 3.6. No contamination is observed for either the proton or pion tracks.

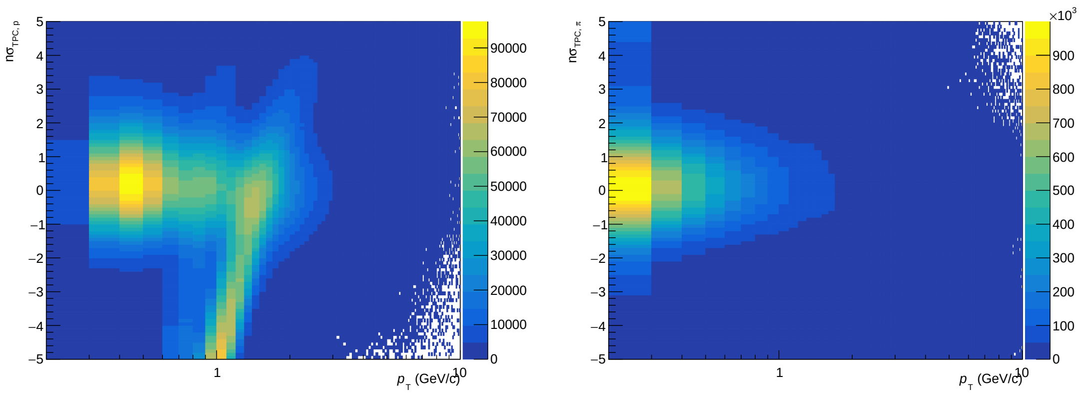

Figure 3.4: $n\sigma$ for protons (left) and pions (right) in the TPC detector as a function of p_T.

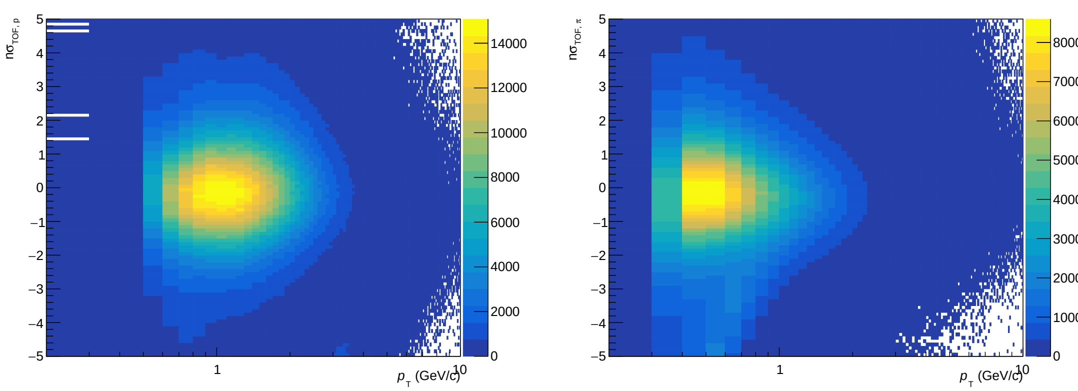

Figure 3.5: $n\sigma$ for protons (left) and pions (right) in the TOF detector as a function of p_T.

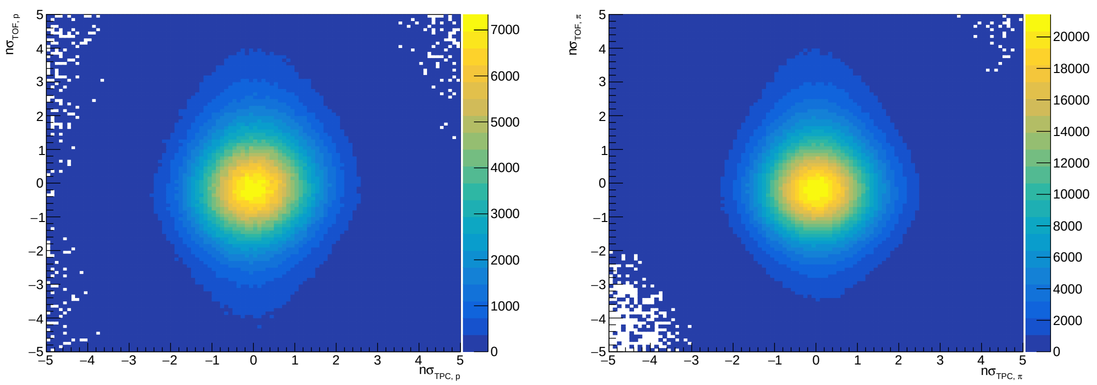

Figure 3.6: $n\sigma$ in TOF vs $n\sigma$ in TPC for protons (left) and pions (right). No contimatination is observed for both of the particle species.

3.3.3 Λ candidate selection

With the daughter proton and pion tracks selected, the Λ candidates are generated by combining all oppositely charged proton-pion pairs into V^0s which meet the topological selection criteria described in Table 3.5.

Table 3.5: Topological selection criteria applied to Λ candidates.

Selection criterion	Value
$\lvert\eta\rvert$	< 0.8
Decay radius (cm)	> 0.2
DCA_{xy} of pion track to PV (cm)	> 0.06
DCA_{xy} of proton track to PV (cm)	> 0.06
DCA_{xy} between daughter tracks (nσ)	< 1.5
$\cos(\theta_{\mathrm{pointing}})$	> 0.9
Invariant mass (GeV/c^2)	$1.102 < M_{p\pi} < 1.130$

The invariant mass $M_{p\pi}$ is calculated using

$$M_{p\pi} = \sqrt{(E_p + E_\pi)^2 - (\vec{p}_p + \vec{p}_\pi)^2}, \tag{3.1}$$

where $E_x = \sqrt{m_x^2 + p_x^2}$ is the energy of the particle of species x. The $M_{p\pi}$ distributions for the Λ candidates for all multiplicity and momentum bins are shown in Figure 3.7. The distributions are also fit with a Voigtian function (convolution of Breit-Wigner and Gaussian [11]) plus a straight line to describe the background. Note that despite our selection criteria, there is still a non-negligible background due to the presence of misidentified Λ candidates. As this background inevitably makes its way into the final h-Λ correlation distributions, it is removed using the technique described in Section **??**.

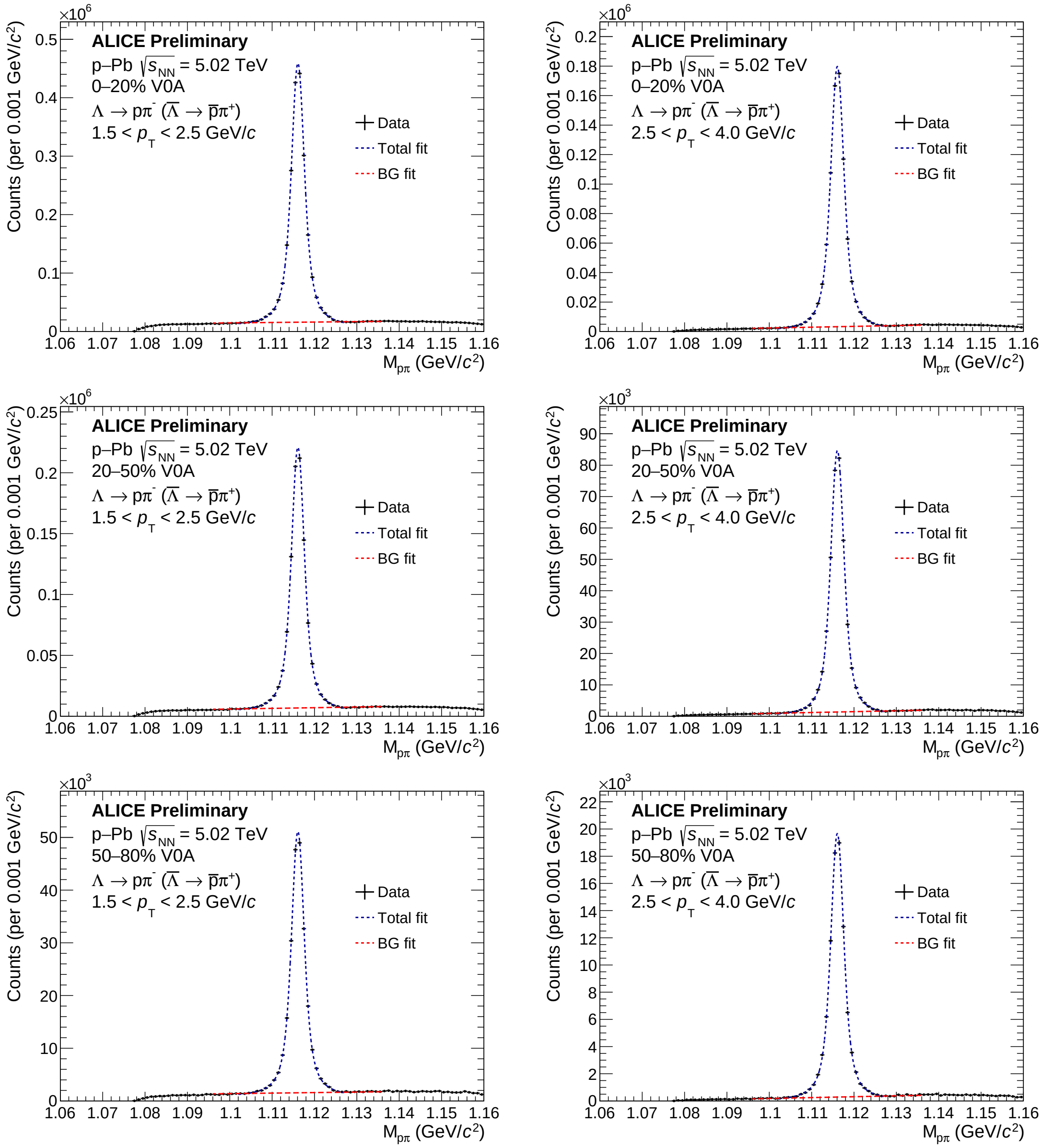

Figure 3.7: Invariant mass distributions in the 0-20% (top), 20-50% (middle), and 50-80% (bottom) multiplicity bins for the Λ candidates which pass the selection criteria with $1.5 < p_T < 2.5$ GeV/c (left) and $2.5 < p_T < 4.0$ GeV/c (right). A Voigtian signal + straight-line background fit to the data is shown in blue, with just the background fit shown in red. For these plots, the Λs were only reconstructed in events with a trigger hadron.

3.4 Reconstruction efficiency

In an ideal world, the number of reconstructed particles of interest would be equal to the number of particles produced in the collision. Unfortunately this is not the case, as there are a number of detector effects which can cause particles to be "lost" during reconstruction. To correct for these effects, the reconstruction efficiency

$$\epsilon(x_1, x_2, ..., x_n) \equiv P(f(x_1, x_2, ..., x_n)|g(x_1, x_2, ..., x_n)), \tag{3.2}$$

is used. Here x_i are the kinematic variables of the particle of interest (e.g. p_{T}, η, φ), $f(x_1, x_2, ..., x_n)$ is the probability that a particle is reconstructed ("found") with kinematic variables x_i, and $g(x_1, x_2, ..., x_n)$ is the probability that a particle is produced ("generated") with the same variables. While the distributions f and g are inaccessable within a given event, the efficiency can be calculated using Monte Carlo simulation techniques via the equation

$$\epsilon(x_1, x_2, ..., x_n) = \frac{N_{\text{reco.}}(x_1, x_2, ..., x_n)}{N_{\text{gen.}}(x_1, x_2, ..., x_n)}, \tag{3.3}$$

where $N_{\text{reco.}}$ and $N_{\text{gen.}}$ are the reconstructed and generated particle distributions, respectively, usually taken across a large number of simulated events. In this analysis, these distributions are calculated as a function of p_{T} and η for each multiplicity class using 30 million events generated by the Monte Carlo event generator DPMJET [9] with particle propagation through the ALICE detector performed by the GEANT3 [12] detector simulation software. These efficiency distributions are then used to correct the h-Λ and h-h correlation distributions using the procedure described in Section 3.5.

3.4.1 Charged hadron reconstruction efficiency

The trigger and associated hadron track reconstruction efficiencies are calculated using Equation 3.3, where the trigger and associated hadrons from $N_{\text{reco.}}$ are subject to the following:

- The track passes the quality cuts outlined in Tables 3.2 (trigger) or 3.3 (associated)
- The track has a corresponding generated particle

- That generated particle is either a pion, proton, kaon, electron or muon
- $|\eta_{\text{track}}| \leq 0.8$,

and the trigger and associated hadrons from $N_{\text{gen.}}$ are subject to:

- $|\eta_{\text{track}}| \leq 0.8$
- The particle is either a pion, proton, kaon, electron or muon
- The particle is primary (i.e. did not originate from a weak decay)

The trigger and associated track reconstruction efficiencies are shown for each multiplicity class as a function of p_{T} in Figure 3.8. While these efficiencies exhibit relatively flat behavior as a function of p_{T} and multiplicity, they are still treated as p_{T} and multiplicity dependent during the correction procedure.

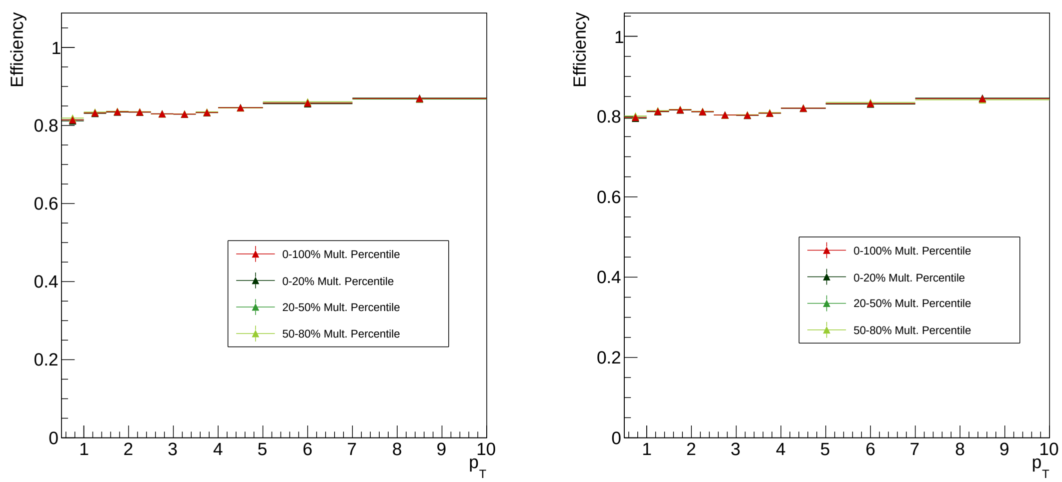

Figure 3.8: Efficiency vs. p_T for trigger (left) and associated (right) hadrons. While they may look identical, the associated hadron efficiency is slightly lower due to the stricter selection criteria.

3.4.2 Λ reconstruction efficiency

The Λ reconstruction efficiency is calculated as a function of p_{T} and η using Equation 3.3, where the Λs from $N_{\text{reco.}}$ are subject to the following:

- They pass the topological selection criteria from Table 3.5
- The reconstructed daughter p, π tracks pass the quality cuts from Table 3.4
- The daughter p, π tracks have corresponding generated p, π particles
- Those generated p, π daughters come from the same mother Λ
- $|\eta_\Lambda| \leq 0.8$,

and the Λs from $N_{\text{gen.}}$ are subject to:

- $|\eta_\Lambda| \leq 0.8$
- The Λ decays to pπ.

The requirement that the generated Λs decay into pπ means the branching ratio is not included in the efficiency calculation as it is corrected for separately (see Section 3.5). The Λ reconstruction efficiency can be seen for each multiplicity class as a function of p_{T} and η in Figure 3.9. Note that the efficiency is no longer flat as a function of η due to the $|\eta| < 0.8$ requirement for the daughter tracks, which kinematically restricts the Λ reconstruction to a smaller η range.

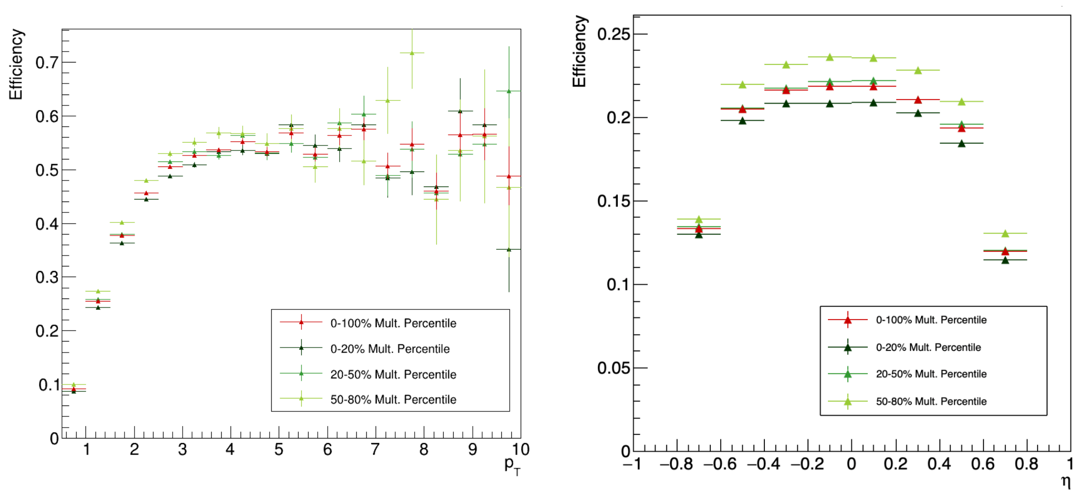

Figure 3.9: Efficiency vs. p_T (left) and η (right) for Λ reconstruction in each multiplicty bin, along with an integrated 0-100% point in red.

3.5 Corrections to the correlation distributions

Once the trigger and associated particles are selected, the two-particle h-Λ and h-h correlation distributions are generated. As mentioned in the previous chapter, the corrected two-particle correlation function is given by

$$\frac{1}{N_{trig}}\frac{d^2N_{pair}}{d\Delta\varphi d\Delta\eta} = \frac{1}{N_{trig}^{corr}}\frac{1}{\epsilon_{trig}\times\epsilon_{assoc}}B(0,0)\frac{S(\Delta\varphi,\Delta\eta)}{B(\Delta\varphi,\Delta\eta)}. \tag{3.4}$$

which contains a number of explicit correction terms (in the form of ϵs) along with some implicit corrections. These corrections are described in this section, and are presented in the order in which they are applied to the data.

3.5.1 Single-particle efficiency corrections

As both the trigger and the associated particles have their own independent reconstruction efficiencies, the trigger-associated pair reconstruction efficiency should be

$$\epsilon_{\text{trig,assoc}} = \epsilon_{\text{trig}} \times \epsilon_{\text{assoc}}, \tag{3.5}$$

meaning the single-particle efficiency distributions from Section 3.4 can be used to calculate the weight $1/(\epsilon_{trig}\times\epsilon_{assoc})$. This weight is applied for each h-Λ and h-h pair in the two-dimensional correlation distribution. However, the assumption that the reconstruction efficiencies are independent is slightly incorrect in the case of the h-Λ distributions due to track merging effects, thus an additional ϵ_{pair} correction is required (discussed in detail in Section 3.5.3).

The trigger efficiency weight $1/\epsilon_{trig}$ is also applied to the single-particle trigger hadron distribution in data to obtain N_{trig}^{corr}.

3.5.2 Mixed-event acceptance correction

As mentioned in Section **??**, the $B(0,0)/B(\Delta\varphi,\Delta\eta)$ term in Equation 3.4 corrects for the finite acceptance along η as both our trigger and associated particles are required to be within $|\eta| < 0.8$. The mixed-event distribution $B(\Delta\varphi,\Delta\eta)$ shown in Figure **??** has a characteristic triangular shape along $\Delta\eta$, which is purely due to detector geometry as no physical correlations are present. When scaled by $1/B(0,0)$, the mixed event distribution becomes the probability that a particle pair is found given that the trigger particle is within $|\eta| < 0.8$, which is unity at $\Delta\varphi, \Delta\eta = 0, 0$. Thus correcting the same-event distribution $S(\Delta\varphi, \Delta\eta)$ by $B(0,0)/B(\Delta\varphi, \Delta\eta)$ removes this acceptance effect and allows for a more accurate determination of the pair-wise yields.

While the generation of the mixed event distribution $B(\Delta\varphi, \Delta\eta)$ was discussed briefly in Section **??**, the specific details are as follows. First, in order to ensure that the mixed-event pairs are coming from similar events, the events in the mixing pool are separated by both multiplicity percentile and $Z_{\text{vtx.}}$ position. The categorizing of events based off of $Z_{\text{vtx.}}$ position is an integral part of the acceptance correction: events with a $Z_{\text{vtx.}}$ at one edge of the detector have a completely different (and nearly inverted) η acceptance than those on the opposite edge. The multiplicity bins are the same as they are for the same-event distributions (namely 0-20%, 20-50% and 50-80%), and the ten $Z_{\text{vtx.}}$ bins are split evenly from -10 cm to 10 cm. For each multiplicity and $Z_{\text{vtx.}}$ bin, the acceptance correction

$$S_{\text{corr.}}(\Delta\varphi, \Delta\eta) = \frac{S(\Delta\varphi, \Delta\eta)}{B(\Delta\varphi, \Delta\eta)/B(0,0)} \tag{3.6}$$

is performed, and the results for each multiplicity bin are then merged across all $Z_{\text{vtx.}}$ bins. The same-event distributions are also split into $Z_{vtx.}$ bins during this correction procedure. The uncorrected distributions $S(\Delta\varphi, \Delta\eta)$ and the mixed-event distributions $B(\Delta\varphi, \Delta\eta)$ are shown for both the h-Λ and h-h cases for all multiplicity and associated momentum bins in Figures 3.10 through 3.13.

This mixed-event correction is the final correction applied to the h-h distributions. However, the h-Λ distributions require additional corrections that are not present in the dihadron case.

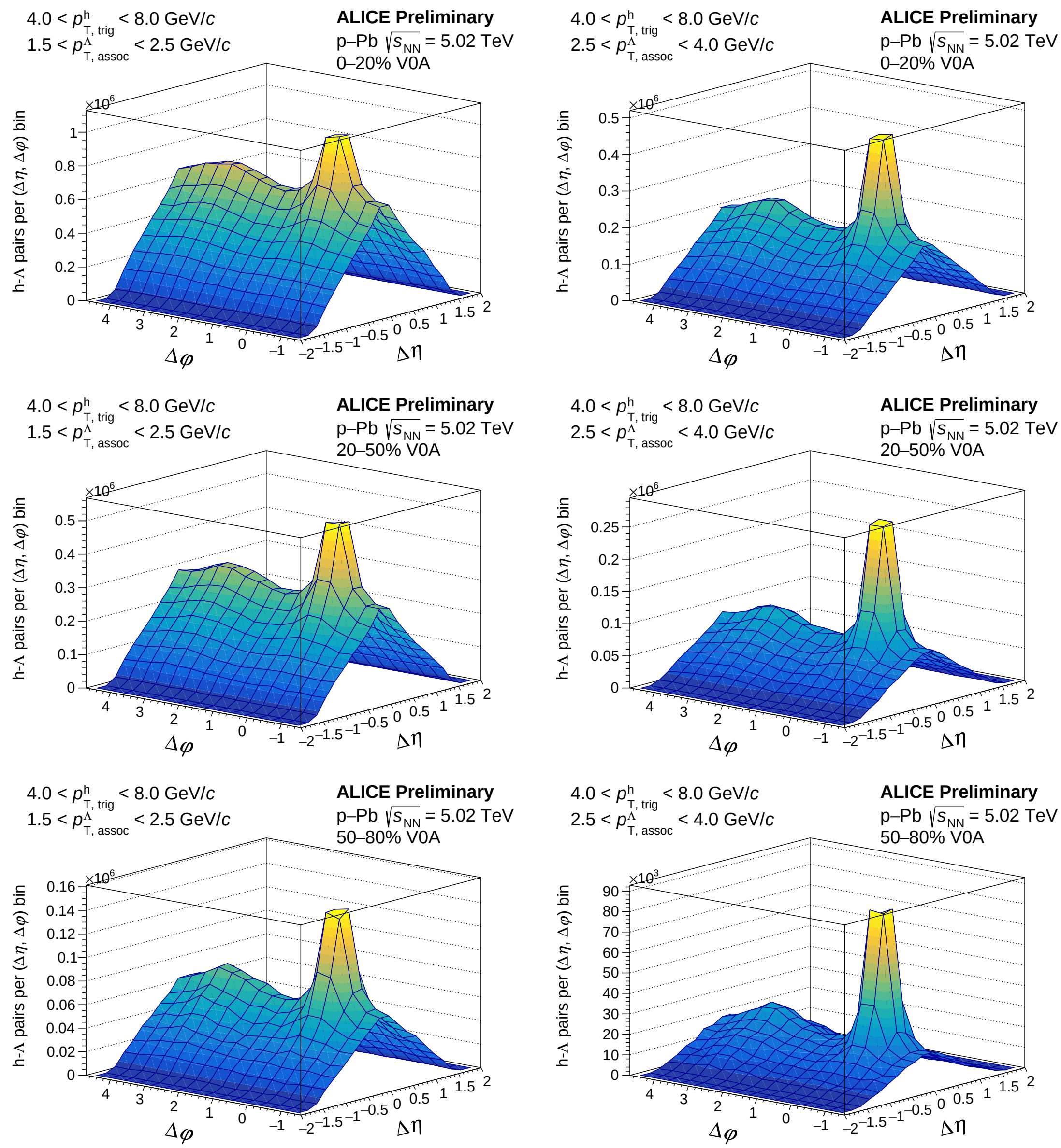

Figure 3.10: 2-D non-acceptance corrected h-Λ angular correlations for the 0-20% (top), 20-50% (middle), and 50-80% (bottom) multiplicity bins for $1.5 < p_{\mathrm{T}} < 2.5$ GeV/c (left) and $2.5 < p_{\mathrm{T}} < 4.0$ GeV/c (right).

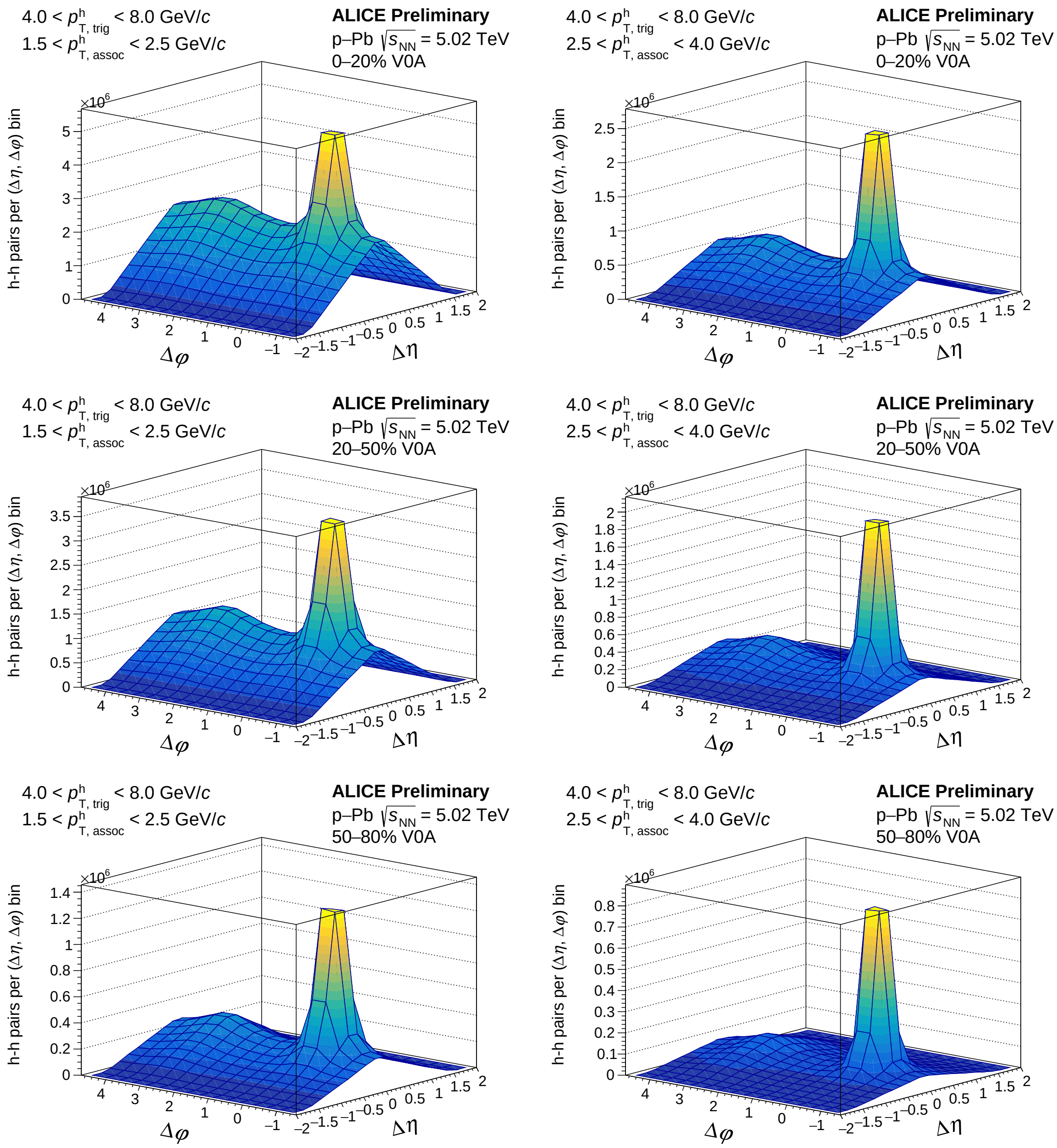

Figure 3.11: 2-D non-acceptance corrected h-h angular correlations for the 0-20% (top), 20-50% (middle), and 50-80% (bottom) multiplicity bins for $1.5 < p_{\mathrm{T}} < 2.5$ GeV/c (left) and $2.5 < p_{\mathrm{T}} < 4.0$ GeV/c (right).

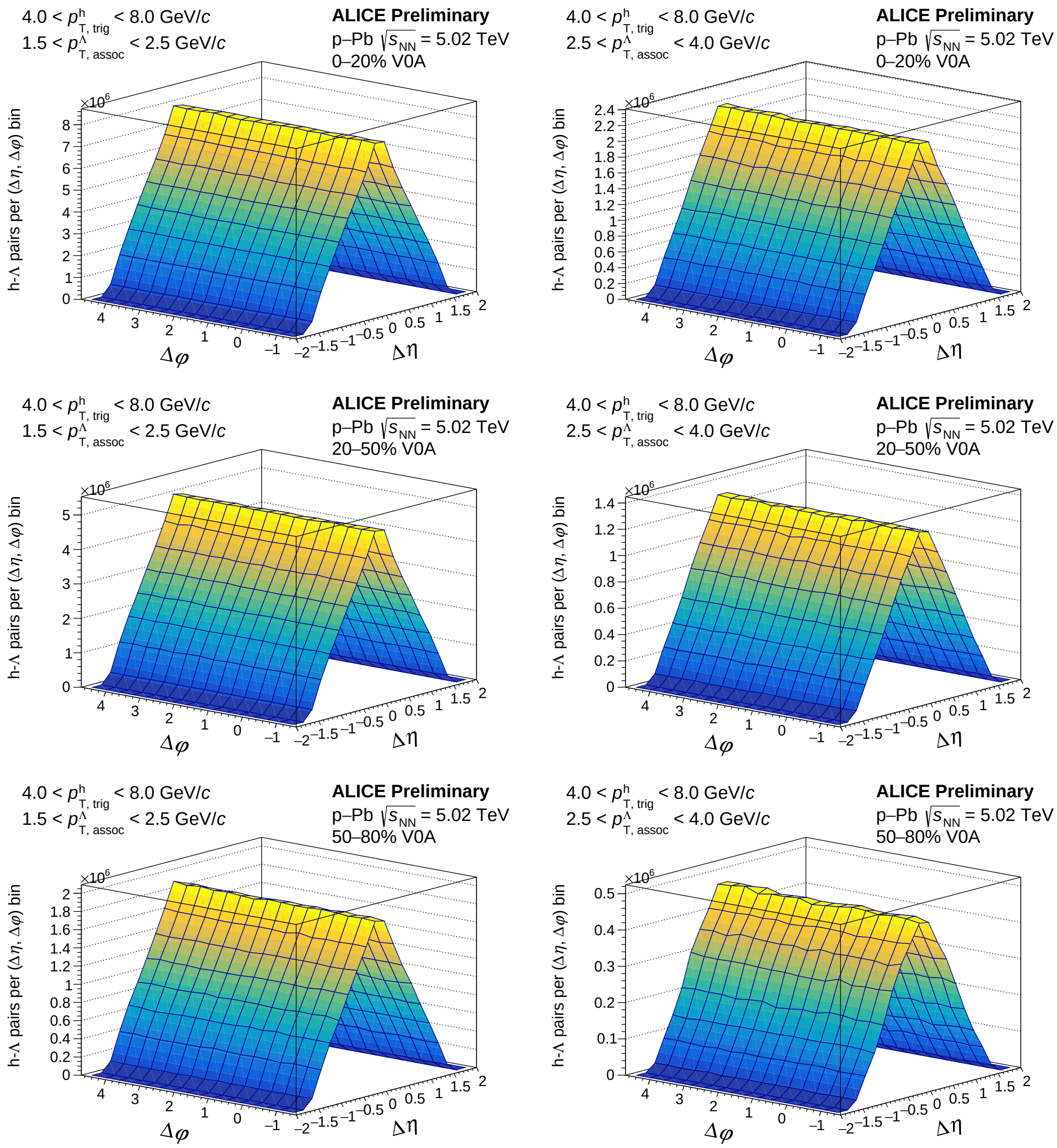

Figure 3.12: 2-D mixed-event h-Λ angular correlations for the 0-20% (top), 20-50% (middle), and 50-80% (bottom) multiplicity bins for $1.5 < p_{\mathrm{T}} < 2.5$ GeV/c (left) and $2.5 < p_{\mathrm{T}} < 4.0$ GeV/c (right). The $Z_{\mathrm{vtx.}}$ bins are merged together for these plots.

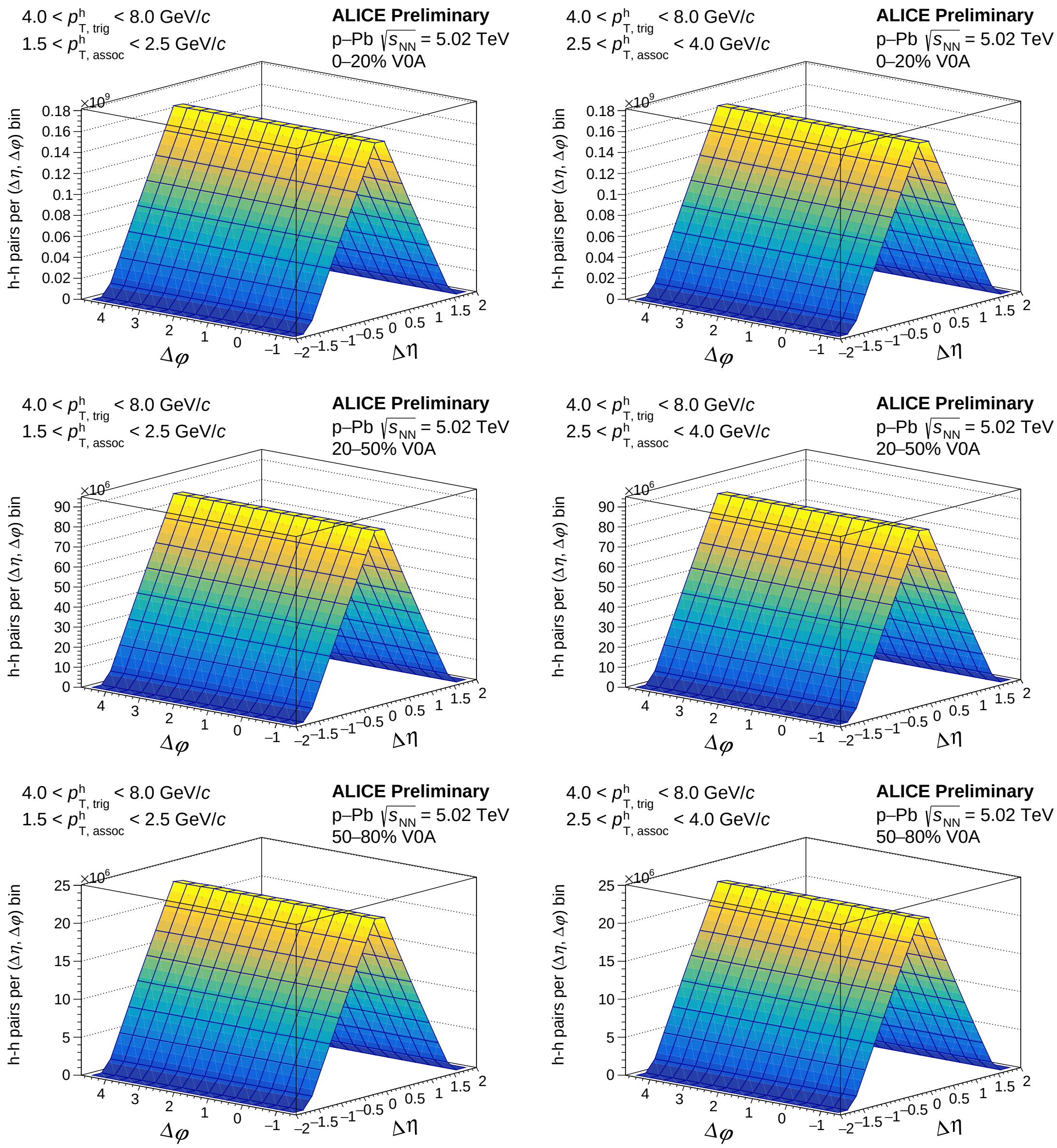

Figure 3.13: 2-D mixed-event h-h angular correlations for the 0-20% (top), 20-50% (middle), and 50-80% (bottom) multiplicity bins for $1.5 < p_{\mathrm{T}} < 2.5$ GeV/c (left) and $2.5 < p_{\mathrm{T}} < 4.0$ GeV/c (right). The $Z_{\mathrm{vtx.}}$ bins are merged together for these plots.

3.5.3 Additional corrections for the h-Λ distributions

While the corrected correlation function from Equation 3.4 is generally true for two-particle correlations, there are a few additional corrections that must be applied to the h-Λ distributions due to the Λ reconstruction procedure and the presence of track merging effects. To formalize this, the corrected h-Λ correlation function can be written as

$$\begin{aligned} C^{\text{h-}\Lambda}_{\text{corr.}}(\Delta\varphi, \Delta\eta) = \frac{r_{\text{signal}} \times r_{\text{branch}}}{\epsilon_{\text{pair}}(\Delta\varphi, \Delta\eta)} \Bigg(& C^{\text{h-p}\pi}_{\text{signal}}(\Delta\varphi, \Delta\eta) \\ & - r_{\text{comb.}} \times C^{\text{h-p}\pi}_{\text{sideband}}(\Delta\varphi, \Delta\eta) \Bigg), \end{aligned} \tag{3.7}$$

where $C^{\text{h-}\Lambda}_{\text{corr.}}$ is the final corrected h-Λ distribution. Each term on the RHS of the equation will be described in detail in the following sections, and they are presented in the order in which they are applied to the distributions.

3.5.3.1 Combinatorial background removal

The term

$$C^{\text{h-p}\pi}_{\text{signal}}(\Delta\varphi, \Delta\eta) - r_{\text{comb.}} \times C^{\text{h-p}\pi}_{\text{SB, norm.}}(\Delta\varphi, \Delta\eta) \tag{3.8}$$

describes the removal of the combinatorial backround resulting from the Λ reconstruction procedure from Section 3.3 using the **sideband subtraction** technique. The $C^{\text{h-p}\pi}_{\text{signal}}$ distribution corresponds to Λ candidates where the invariant mass of the pπ pair falls within the range specified in Table 3.5, and the self-normalized $C^{\text{h-p}\pi}_{\text{SB, norm.}}$ distribution corresponds to candidates where the mass of the pπ pair falls within the so-called "sideband" region. An invariant mass plot highlighting these different regions can be seen in Figure 3.14. Both of the C_{signal} and C_{sideband} distributions are corrected for acceptance and efficiency using the techniques described in the previous sections. The sideband region is chosen such that it is far enough away from the signal region to be free of any Λ signal, but close enough to ensure that the background pπ pairs in the signal region are kinematically similar to the pairs in the sideband region as to not introduce any biases in the correlations. The underlying assumption of this technique is that the correlation shape of h-pπ pairs from the sideband region is the same as the shape from the background h-pπ pairs in the signal region. For this analysis, the nominal sideband region was chosen to be $1.135 < M_{p\pi} < 1.150$

GeV/c^2, but the effects of varying this region are studied in detail in the next chapter. The $r_{\text{comb.}}$ is the integral of the combinatorial background in the $C^{\text{h-p}\pi}_{\text{signal}}$ distribution, obtained by

$$r_{Comb} \equiv \frac{B}{S+B} \int \int C^{\text{h-p}\pi}_{\text{signal}}(\Delta\varphi, \Delta\eta) d\Delta\varphi d\Delta\eta, \tag{3.9}$$

where S and B are the signal and background obtained from the fits to the Λ invariant mass distributions in Figure 3.7. As the S/B ratio is the same for the Λ invariant mass distributions in events with a trigger hadron as it is for the h-Λ distributions, the scale $B/(S+B)$ can be used to give only the background contribution from the integral $\int\int C^{\text{h-p}\pi}_{\text{signal}}(\Delta\varphi, \Delta\eta) d\Delta\varphi d\Delta\eta$. The self-normalized $C^{\text{h-p}\pi}_{\text{SB, norm.}}$ distribution is then scaled by $r_{\text{comb.}}$ and subtracted from $C^{\text{h-p}\pi}_{\text{signal}}$ to remove the combinatorial background.

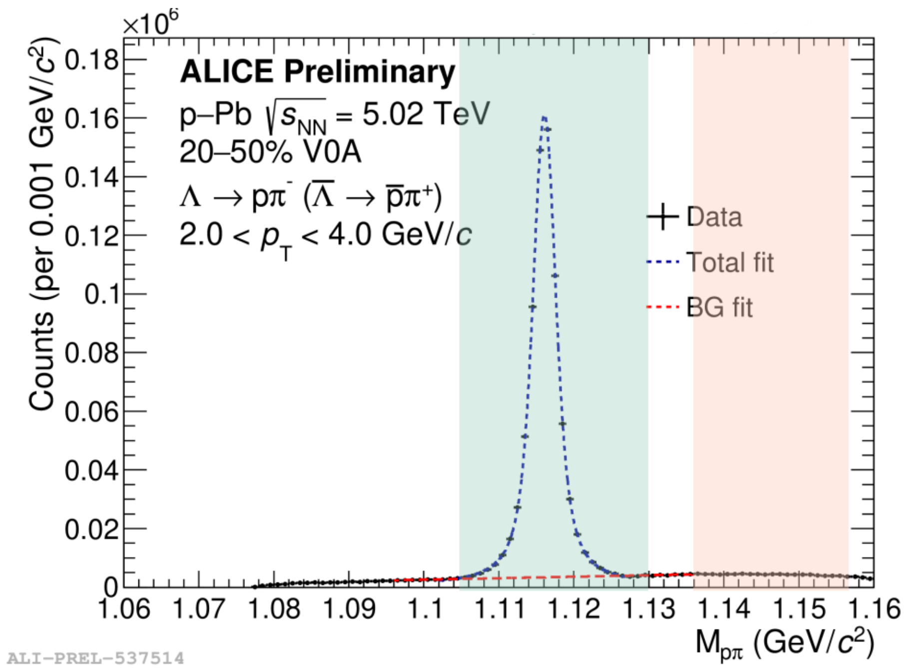

Figure 3.14: Invariant mass distribution of pπ pairs in the 20-50% multiplicity class. The signal region is shown in light green, and the sideband region is shown in light pink. The correlation distribution in the sideband region is used to remove the combinatorial background from the signal region.

While the above procedure desribes the background removal in a more technical manner, it can be condensed into the following steps:

1. Generate the correlation distribution using Λ candidates in the signal invariant mass region

2. Do the same thing for Λ candidates in the sideband invariant mass region
3. Scale the sideband distribution to match the background in the signal region
4. Subtract the sideband distribution from the signal distribution

Examples of the signal and sideband distributions $C^{\text{h-p}\pi}_{\text{signal}}$ and $C^{\text{h-p}\pi}_{\text{SB}}$ are shown for the 0-20% multiplicity bin in Figure 3.15.

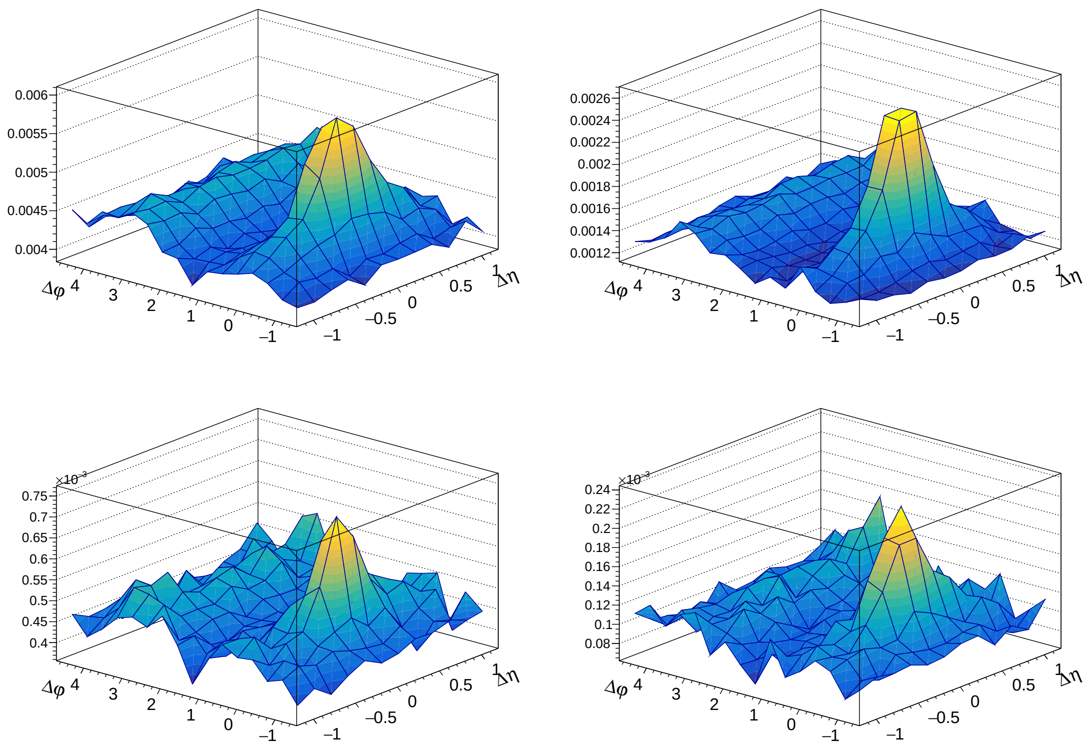

Figure 3.15: The signal (top) and sideband (bottom) distributions $C^{\text{h-p}\pi}_{\text{signal}}$ and $C^{\text{h-p}\pi}_{\text{SB}}$ for the lower (left) and higher (right) associated p_{T} bins. All plots were generated in the 0-20% multiplicity class.

3.5.3.2 Signal scaling

As the Λ candidate invariant mass signal region is finite, the fraction of the Λ signal that is missed in the tails of the invariant mass distribution must be corrected for.

This is handled by the r_{signal} term in Equation 3.7, which is calculated by

$$r_{\text{signal}} \equiv \left(\frac{\text{Integral of residual in signal region}}{\text{Integral of residual between 1.098 and 1.134}}\right)^{-1} \tag{3.10}$$

where "residual" refers to the invariant mass distributions from Figure 3.7 after subtracting the straight-line background fit. 1.098 and 1.134 are the points in which there is effectively zero signal, verified in Monte Carlo. Due to the width of the signal region, r_{signal} is usually near unity. However, to study the effects of narrowing the signal region, this term must be included in the analysis.

3.5.3.3 Branching ratio correction

The most simple correction from Equation 3.7 comes from the branching ratio term, namely

$$r_{\text{branch}} \equiv \frac{1}{BR(\Lambda \to p\pi)} = \frac{1}{0.639}. \tag{3.11}$$

As not all Λs decay into pπ pairs, this term corrects for the fraction of Λs that decided to decay into something else. In many analyses, this term is not required is it is already included in the efficiency computation $\epsilon_{\text{assoc.}}$. As the Λ reconstruction efficiency from this analysis is calculated using only Λs that decay into pπ pairs, this term must be included separately.

3.5.3.4 Pair efficiency correction

The ϵ_{pair} term in Equation 3.7 is the h-Λ "pair" efficiency, which is used to correct for track merging effects. Many correlation studies are susceptible to track merging inefficiencies [13], [14], whereby either the trigger or associated particle gets merged over by the other during the track reconstruction. This results in a dip at small angles in the angular correlation distribution when compared to a similar distribution with no instances of track merging. As this effect cannot be seen directly in data due to the missing reconstructed tracks, it is investigated using the Monte Carlo sample, where the reconstructed tracks are compared to the MC-generated particles they were reconstructed from. While this effect is usually negligible and only relevant at extremely small angles ($\Delta\varphi < 0.01, \Delta\eta < 0.1$), in this analysis this effect is more severe and occurs at larger angles ($\Delta\varphi < 1, \Delta\eta < 0.6$), shown in Figure 3.16.

The severity of this effect for the h-Λ distributions is likely due to two factors:

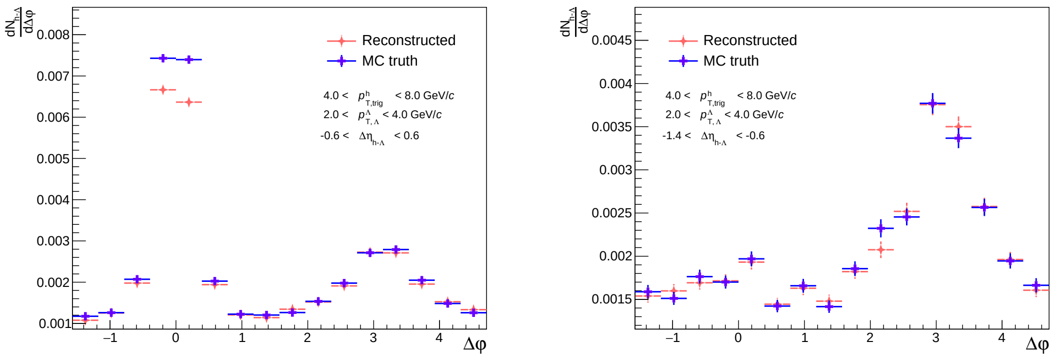

Figure 3.16: Demonstration of the track merging effect for h-Λ pairs, whereby we see a dip in the reconstructed distribution at small $\Delta\varphi$ and $\Delta\eta$ when compared to the MC ground truth (left). This dip is not present at large $\Delta\eta$ (right), but we also lose nearly the entirety of our near-side peak.

- The Λ decay length is large ($c\tau \approx 10$ cm), meaning the daughter particles will have less hits in the detector than the trigger particle (which is produced at the primary vertex). As Kalman filtering (track reconstruction) favors the track with more hits, the Λ daughter track is "merged" over by the trigger track.
- The Λ decay is asymmetric ($m_p/m_\pi \approx 7$), so the Λ and daughter proton end up with similar momenta (and thus φ and η). This means that whenever a proton from a Λ decay is "merged" over by a trigger track, a h-Λ pair with small $\Delta\varphi, \Delta\eta$ is lost.

To see how the decay length can affect the track merging, the (reconstructed)/(MC ground-truth) $C(\Delta\varphi, \Delta\eta)$ distribution ratio for h-pion pairs in our MonteCarlo sample where the pion is **secondary**–meaning it came from a weak decay with decay length $>$ 2cm–is measured. Pions are chosen for this demonstration as they are more abundantly produced than protons, and charged track reconstruction is particle species agnostic. Any "dips" from unity present in this ratio are indicative of pairs being lost during reconstruction. This is then compared to the same ratio for $h-$pion pairs where the pion is **primary**, and the results are shown in Figure 3.17. All reconstructed triggers and pions pass the trigger hadron and Λ daughter cuts from Tables 3.2 and 3.4, respectively. Furthermore, all distributions have been fully corrected for single-particle efficiencies and detector acceptance using the procedures from Sections 3.5.1 and 3.5.2, respectively. A large suppression at small $(\Delta\varphi, \Delta\eta)$ is observed for the h-secondary pion case, but the h-primary pion case exhibits no such supression. As such, it stands to reason that this suppression is at least in part due to the decay length of the Λ, as all particles that come from Λs are secondaries (by a long shot).

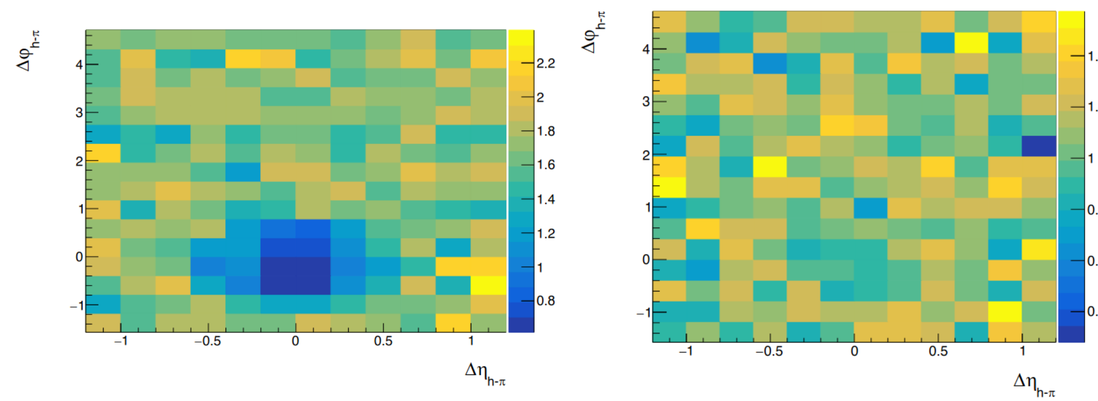

Figure 3.17: The reconstructed/ground truth ratios of the 2D $C(\Delta\varphi, \Delta\eta)$ distributions for h-(secondary pions) (left) and h-(primary pions) (right). The suppression at smaller $\Delta\varphi, \Delta\eta$ is clearly seen in the secondary case, but is not observable in the primary case, indicating a decay-length dependence.

The p_{T} dependence of this effect can also be studied by measuring the reconstructed and ground truth $h-$(secondary pion) $\Delta\varphi$ distributions at low ($1.0 < p_{\mathrm{T}} < 2.0$ GeV/c) and high ($2.0 < p_{\mathrm{T}} < 4.0$ GeV/c) associated momentum. The result is shown in Figure 3.18. Note that the distributions were projected onto $\Delta\varphi$ with $|\Delta\eta| < 1.2$. A suppression relative to MC ground-truth is observed in the near-side of the reconstructed distribution in the higher p_{T} range, which is not seen in the low p_{T} bin. This is also consistent with the decay length dependence shown in the previous figures, as decay length is roughly proportional to p_{T}.

The p_T dependence of this inefficiency demonstrates why this effect is so severe in the h-Λ case: due to the asymmetry of the Λ decay ($m_{\mathrm{p}}/m_{\pi} \approx 7$), the daughter proton receives most of the momentum. Therefore when investigating h-Λ correlations within a given associated p_{T} range, any inefficiencies present in the corresponding h-(daughter proton) distribution with the same associated momentum would also be present in our final h-Λ distribution within a similar $\Delta\varphi, \Delta\eta$ range. As demonstrated in Figure 3.18, secondary charged particles with $2 < p_T < 4$ GeV/c see a large

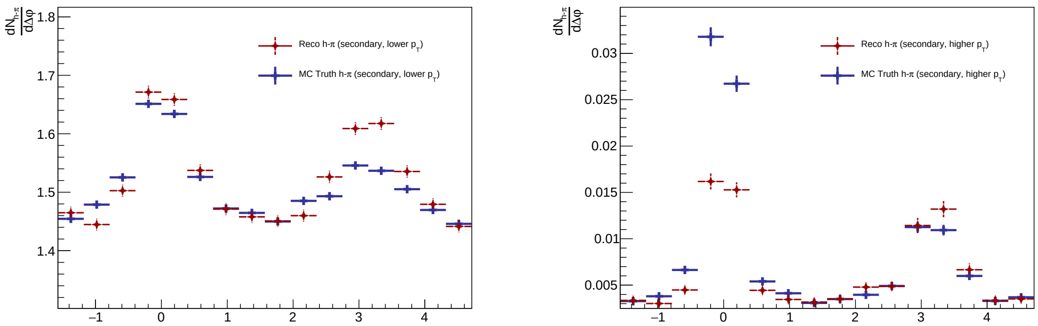

Figure 3.18: The reconstructed and ground truth $\Delta\varphi$ distributions in the $-1.2 < \Delta\eta < 1.2$ region for h-(secondary pions) with $0.15 < p_{\mathrm{T}} < 2$ (left) and $2 < p_{\mathrm{T}} < 4$ (right). The suppression at smaller $\Delta\eta, \Delta\varphi$ is clearly seen in the higher momentum bin, but not present in the lower one.

inefficiency, and therefore we would expect a similar inefficiency to be present in our h-Λ distribution (which was shown in Figure 3.16). In similar analyses using the $\mathrm{K}^0_{\mathrm{S}}$ in leiu if the Λ [15], such an effect is not as present, both because the decay length is much shorter (2 cm vs 10 cm), and the $\mathrm{K}^0_{\mathrm{S}}$ decay is symmetric, meaning the daughter pions will have momenta that are no longer similar to the mother kaon.

The folling techniques have been investigated to correct for this effect:

- Applying a $\Delta\varphi^*$ correction, described in **DphiStar**: While $\Delta\varphi$ and $\Delta\varphi^*$ are different, they are correlated enough that in order to remove this effect, a $|\Delta\varphi^*| < 0.7$ cut is required, which removes a significant amount of the near-side yield in the corresponding $\Delta\varphi$ distribution.

- Applying a cut on the minimum distance between the fully reconstructed helices of the trigger and Λ daughter proton (varied between 0.1 cm and 10 cm): Again, this cut removes roughly the same amount of near-side yield as the $\Delta\varphi^*$ cut, as this minimum distance is also highly correlated with $\Delta\varphi$.

- Using the resonance technique for Λ reconstruction (more details in Section 4.2.4): this moderately reduces the severity of this effect, but the statistical fluctuations introduced by the smaller S/B ratio make it difficult to gauge how effective this correction is.

- Only correlating h-Λ pairs where the charge of the Λ daughter proton (or antiproton) is opposite to the trigger, as oppositely charged tracks bend in opposite directions in the detector magnet: This reduces the effect by a considerable amount, but reduces our overall correlation statistics by a factor of 2.

- Selecting "lower quality" trigger tracks by loosening the cuts from Table 3.2 so they are less likely to be merged over the low-quality daughter tracks: this reduces the effect, but introduces a large amount of secondary contamination. Furthermore, we would like this analysis to be directly compared with other analyses, and therefore want to maintain the same cuts on the trigger hadron.

- Selecting "higher quality" Λ daughter tracks by tightening the cuts from Table 3.4 (and adding additional selection criteria): this again reduces the effect but heavily cuts into the Λ signal

As each of these techniques reduces the statistics of the h-Λ correlation distribution beyond the realm of acceptability, the two-track inefficiencies are instead corrected for using a MC-generated template method, similar to the one used in [14]. For this method, the pair efficiency is given by

$$\epsilon_{pair}(\Delta\varphi, \Delta\eta) \equiv \frac{C^{\mathrm{tag}}_{\mathrm{reco}}(\Delta\varphi, \Delta\eta)}{C_{\mathrm{gen}}(\Delta\varphi, \Delta\eta)}, \tag{3.12}$$

where $C^{\mathrm{tag}}_{\mathrm{reco}}$ is the efficiency-corrected correlation distribution calculated in MC using reconstructed trigger hadrons and Λ candidates with the same selection criteria as described in Section 3.2, with the additional requirement that the Λ candidate has a corresponding generated Λ which is used for all calculations involving kinematic quantities. This removes the need to perform any of the additional corrections from the previous sections (e.g. background subtraction, signal scaling) as the invariant mass of generated lambdas is exact. C_{gen} is the correlation distribution calculated in MC using only generated trigger hadrons and Λ candidates. The template $\epsilon_{pair}(\Delta\varphi, \Delta\eta)$ is applied for each associated p_{T} bin in this analysis, but it is independent of multiplicity and event generator. The templates for each associated p_{T} bin are shown in Figure 3.19. This correction is applied to the h-Λ distributions after side-band subtraction, signal scaling and the branching ratio correction.

After these corrections, both the h-Λ and h-h 2D distributions are finalized and ready for projection onto $\Delta\varphi$ to extract the yields and widths of interest from the

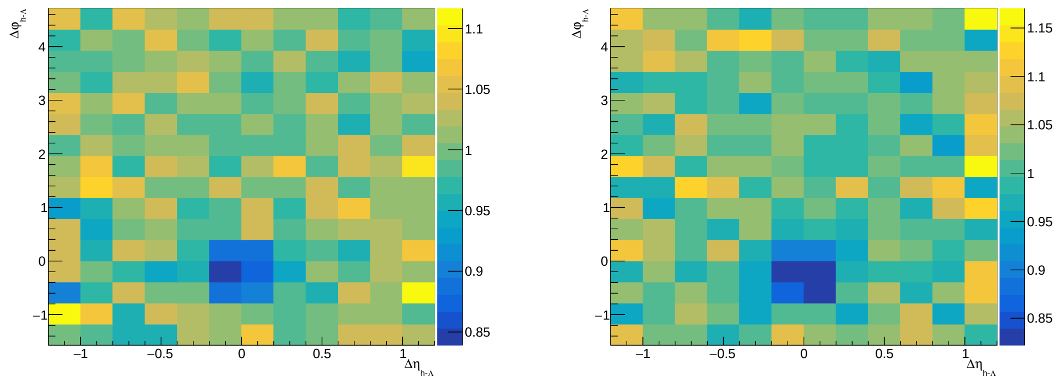

Figure 3.19: The $\epsilon_{\mathrm{pair}}(\Delta\varphi, \Delta\eta)$ templates for the track merging correction in the lower ($1.5 < p_{\mathrm{T}} < 2.5$ GeV/c, left) and higher ($2.5 < p_{\mathrm{T}} < 4.0$ GeV/c, right) associated momentum bins. While it may be difficult to observe, the lower p_{T} bin has a minimum dip of around 0.84, whereas the higher p_{T} bin has a minimum dip of around 0.81, reflecting the p_{T} dependence discussed in this section.

previous chapter. However, there are still a number of systematic uncertainties to investigate and cross-checks required to ensure the validity of the final results.

Chapter Four: Systematic uncertainties and cross-checks

While it would be nice to produce exact results for the measurements presented in this thesis, uncertainties are inevitable. These uncertainties are usually grouped into two categories: **statistical uncertainties** and **systematic uncertainties**. Statistical uncertainties are those which arise from things like detector imprecisions or even the inherent statisical nature of the measurement itself. Calculating these uncertainties is *usually* straightforward, though it often involves well-motivated assumptions about the underlying probability distributions of the data. Determining systematic uncertainties, on the other hand, is a much more complicated process. To that end, the first section of this chapter goes into a large amount of detail about the calculation of systematic uncertainties for this analysis, starting with clearly defining what "systematic uncertainty" means and how it is quantified in the context of this thesis, followed by comprehensive ingestigations into each of the sources of uncertainty considered in this research, and ending with a summary of the final systematic uncertainties for each observable.

The second section of this chapter is dedicated to the cross-checks performed to ensure the validity of the analysis procedure. There are a variety of such checks, ranging from a general Monte Carlo closure test to more specific checks into physical biases that may be introduced by the analysis procedure.

4.1 Systematic uncertainties

> *"The treatment of systematic errors is often mishandled. This is due to lack of understanding and education, based on a fundamental ambiguity as to what is meant by the term"*
>
> —Roger Barlow, *Systematic Errors: Facts and Fictions* [16]

In every experimental analysis, choices must be made. These choices can be as simple as the selection of a particular data set, or as complex as choosing a fit function of fifteen parameters instead of three. In either case, these choices can have an effect on the final results, which is usually quantified by the **systematic uncertainty**. Broadly speaking, the systematic uncertainty is a measure of the sensitivity of the final results to the choices made during the analysis procedure.

In this analysis, the procedure for estimating the systematic uncertainty from a certain choice is as follows:

1. Vary the choice in a way that is reasonable and justifiable
2. Measure the observable of interest after the variation
3. Quantify the effect of the variation on the observable by calculating the percent change from the original value of the observable
4. Vary the choice in a slightly different way, and repeat steps 2 and 3
5. Repeat steps 2 through 4 until all reasonable variations have been considered
6. Calculate the systematic uncertainty as the root mean square (RMS) of the percentages from step 3.

Note the usage of the words "reasonable" and "justifiable", which seem to indicate that the systematic uncertainty is a subjective quantity. Indeed the process of obtaining the systematic uncertainty involves even more choices, like the choice of which choices to consider, the choices of how to vary the choices, and even the choice on how to quantify the uncertainty itself. In this sense, systematic uncertainty calculations are an art form, where the artist (analyzer) must use their creativity and best judgement to determine which choices are indeed reasonable. To that end, the list of sources of systematic uncertainties considered for this analysis is not exhaustive, but it is the best attempt at a comprehensive list of reasonable choices that affect the final results.

To provide more structure to this section, the analysis procedure is broken into the following components:

1. The generation of the h-Λ and h-h $\Delta\varphi$ distributions,
2. The extraction of the pairwise yields from the $\Delta\varphi$ distributions, and
3. The extraction of the near- and away-side widths from the fits of the $\Delta\varphi$ distributions,

which are used to separate this section into three subsections, one for each of these components. In each section, the sources of systematic uncertainties are described, followed by a Barlow analysis [16] to ensure the variations result in a statistically significant deviation from the nominal values. Finally, a summary of the final systematic uncertainties is provided.

4.1.1 $\Delta\varphi$ distribution generation

The sources of systematic uncertainties that affect the $\Delta\varphi$ distribution considered for this analysis are the following, in order of decreasing magnitude:

- Λ topological selection (h-Λ distribution only)
- Material budget
- Tracking efficiency
- Λ daughter PID cuts (h-Λ distribution only)
- Λ invariant mass signal region selection (h-Λ distribution only)
- Λ invariant mass sideband region selection (h-Λ distribution only)

As the Λ topological selection, material budget, and tracking efficiencies have been studied in detail in previous analyses using the same particle species and collision system [15], [17], [18], the systematic uncertainty associated with these sources is taken directly from these analyses and presented in Table 4.1. The uncertainties from these sources exhibit no multiplicity dependence, and a very small dependence on p_{T}. These uncertainties are also assumed to be independent of $\Delta\varphi$, although this is studied more thoroughly in Section 4.1.3.

Each of the other sources of systematic uncertainty is described in detail in the following sections.

4.1.1.1 Signal region selection

The nominal signal region for the Λ invariant mass is fairly wide, accounting for nearly 97% of the total Λ signal. However, the final result should not be heavily influenced by the choice of signal region so long as it is centered about the true Λ

Table 4.1: The systematic uncertainties for the $\Delta\varphi$ distributions which are not directly calculated in this thesis, instead taken from previous analyses using the same particle species and collision system [15], [17]–[19]. Each source of uncertainty is verified to be independent of multiplicity, but the Λ material budget and topological selection uncertainties exhibit a small dependence on p_{T}.

Source name	Lower p_{T} %	Higher p_{T} %
Λ topological selection	3.2%	3.0%
Λ material budget	1.1%	0.6%
Charged h tracking efficiency	3.5%	3.5%
Charged h material budget	negl.	negl.

mass. Furthermore, altering the signal region tests the validity of the signal scaling procedure outlined in Section 3.5. To investigate this, the signal region is varied in the ways presented in Table 4.2. The resulting $\Delta\varphi$ distributions and ratios to the nominal distribution for each signal region variation in each multiplicity and associated p_{T} bin are shown in Figures 4.1 (lower p_{T}) and 4.2 (higher p_{T}). The average deviation from the nominal distribution is around 2%, with no invividual variation exceeding 5%. As no significant dependence on $\Delta\varphi$ is observed, the systematic uncertainty is calculated as the RMS of the percent change from each variation across the entire $\Delta\varphi$ range as opposed to calculating the RMS in each bin.

Table 4.2: The variations of the Λ invariant mass signal region considered for this analysis.

Variation name	Signal range (GeV/c^2)
Narrow	$1.108 < M_{p\pi} < 1.124$
Narrower	$1.112 < M_{p\pi} < 1.120$
Wide	$1.100 < M_{p\pi} < 1.132$
Wider	$1.096 < M_{p\pi} < 1.136$

4.1.1.2 Sideband region selection

The choice of sideband region also leaves a lot of room for reasonable variation: all that is required is that the region is 1) large enough to produce a smooth h-pπ distribution with minimal statisical fluctuations and 2) close enough to the signal region that the pπ pairs are kinematically similar to those in the background of the signal region. As long as these requirements are met, the final result should not be very dependent on the choice of sideband region. To investigate the effects of changing the sideband region, the variations presented in Table 4.3 are considered. The measured $\Delta\varphi$ distributions and variation/nominal ratios for each sideband region variation in each multiplicity and associated p_{T} bin are shown in Figures 4.3 (lower p_{T}) and 4.4 (higher p_{T}). The result is even less deviation from the nominal distribution than the signal region variations, with the average deviation being closer to 1%. Again, no significant dependence is observed on $\Delta\varphi$, so the systematic uncertainty is calculated as the RMS of the percent change from each variation across every $\Delta\varphi$ bin.

Table 4.3: The variations of the Λ invariant mass sideband region considered for this analysis. Note that the "shifted left" sideband falls on the opposite (left) side of the signal region.

Variation name	Sideband range (GeV/c^2)
Narrow	$1.135 < M_{p\pi} < 1.145$
Wide	$1.135 < M_{p\pi} < 1.16$
Shifted left	$1.086 < M_{p\pi} < 1.098$
Shifted right	$1.14 < M_{p\pi} < 1.155$

4.1.1.3 Λ daughter particle identification

The Λ daughter particle identification (PID) cuts are chosen to be wide enough to ensure a high efficiency, but narrow enough to ensure a high purity. As the requirement for a higher purity should be offset by the subtraction of the combinatorial background, altering the PID cuts should only minimally effect the final $\Delta\varphi$ distributions. To study this, the PID cuts are varied in the ways presented in Table 4.4. The final $\Delta\varphi$ distributions and ratios to the nominal distribution for each PID cut variation in each multiplicity and associated p_{T} bin are shown in Figures 4.5 (lower p_{T}) and 4.6 (higher p_{T}). Requiring a signal in the TOF detector drastically reduces the Λ signal as the daugher pions are often heavily deflected by the magnetic field due to their lower p_{T} (again, $m_{\mathrm{p}}/m_{\pi} \approx 7$, so most of the mother momentum belongs to the proton). This causes a large amount of statistical fluctuations in the corresponding $\Delta\varphi$ distribution, which is why the "require TOF" variation is inevitably excluded after the Barlow check presented in Section 4.1.1.4. The other variations result in only around a 2% deviation from the nominal $\Delta\varphi$ distribution, on average.

Table 4.4: The variations of the Λ daughter PID cuts considered for this analysis. The "require TOF" variation requires a TOF hit for both the proton and pion, but maintains the nominal values for $|n\sigma_{\mathrm{TPC,\ TOF}}|$.

Variation name	$\lvert n\sigma^{\pi}_{\mathrm{TPC,TOF}}\rvert$	$\lvert n\sigma^{\mathrm{p}}_{\mathrm{TPC,TOF}}\rvert$
Narrow	< 1.8	< 1.2
Wide	< 4.2	< 2.8
Require TOF	< 3.0	< 2.0

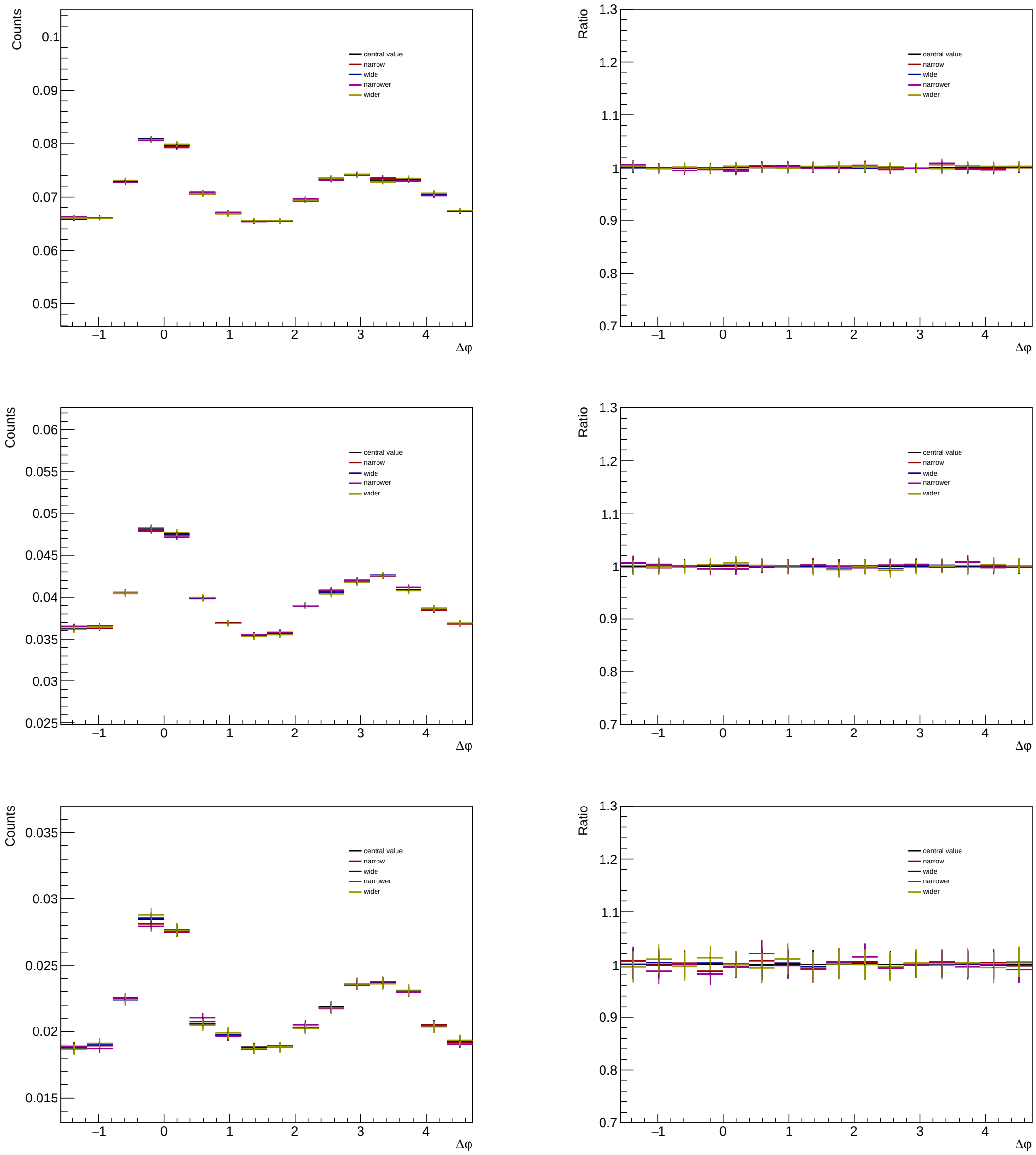

Figure 4.1: The h-Λ $\Delta\varphi$ distributions within the 0-20% (top), 20-50% (middle) and 50-80% (bottom) multiplicity bins in the lower associated p_{T} bin for each of the signal region variations (left) with the ratios to the nominal distribution (right).

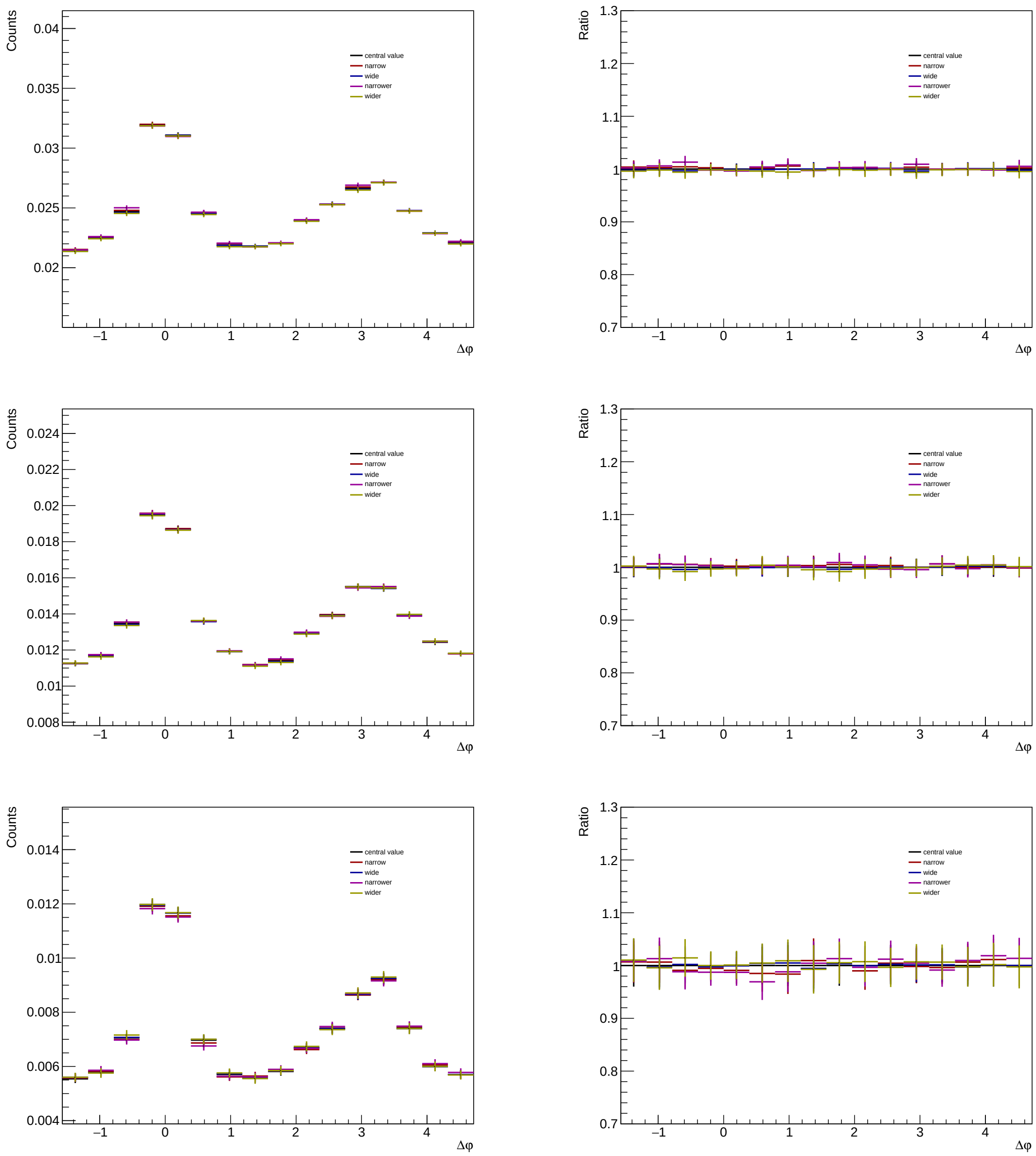

Figure 4.2: The h-Λ $\Delta\varphi$ distributions within the 0-20% (top), 20-50% (middle) and 50-80% (bottom) multiplicity bins in the higher associated p_{T} bin for each of the signal region variations (left) with the ratios to the nominal distribution (right).

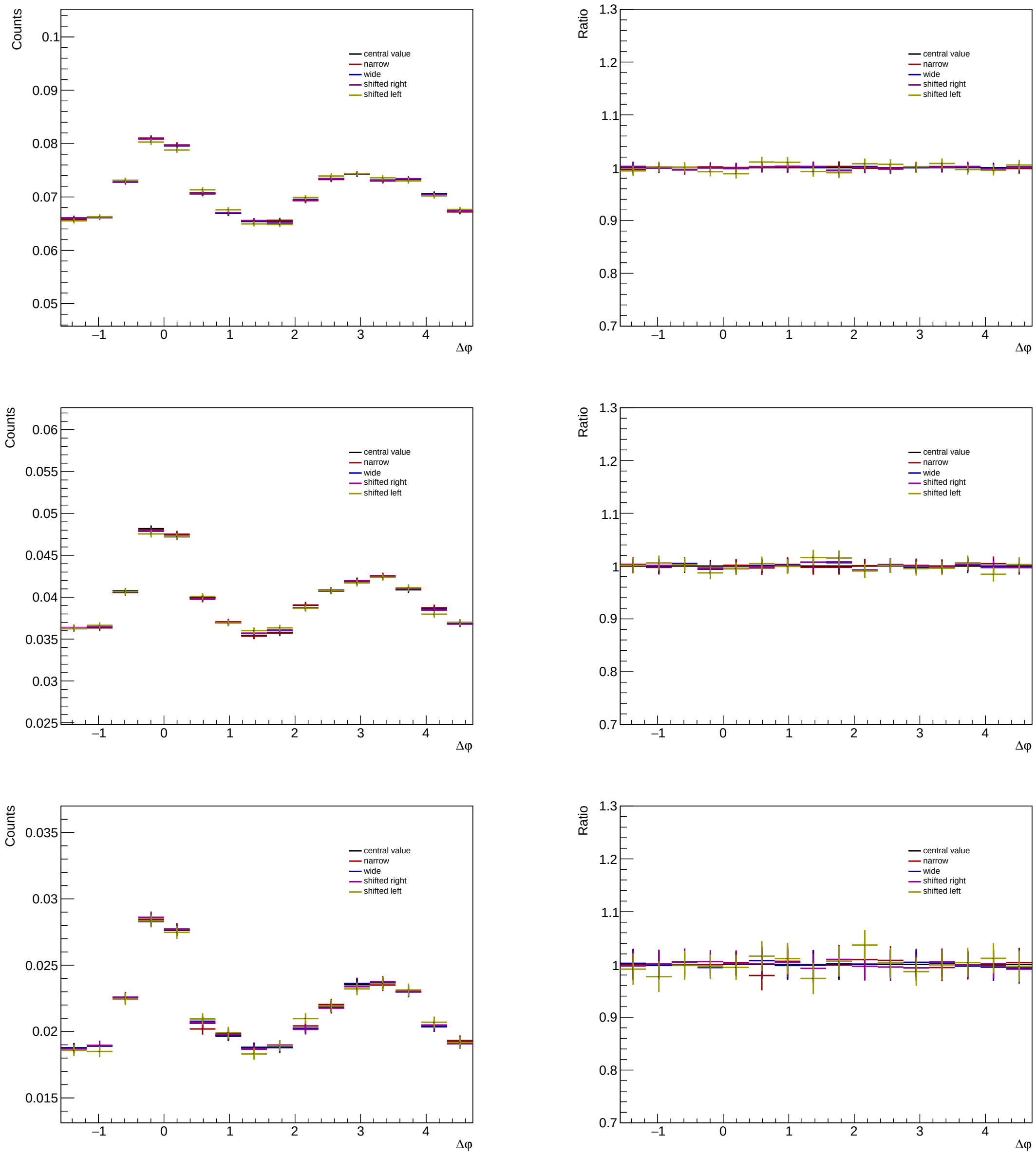

Figure 4.3: The h-Λ $\Delta\varphi$ distributions within the 0-20% (top), 20-50% (middle) and 50-80% (bottom) multiplicity bins in the lower associated p_{T} bin for each of the sideband region variations (left) with the ratios to the nominal distribution (right).

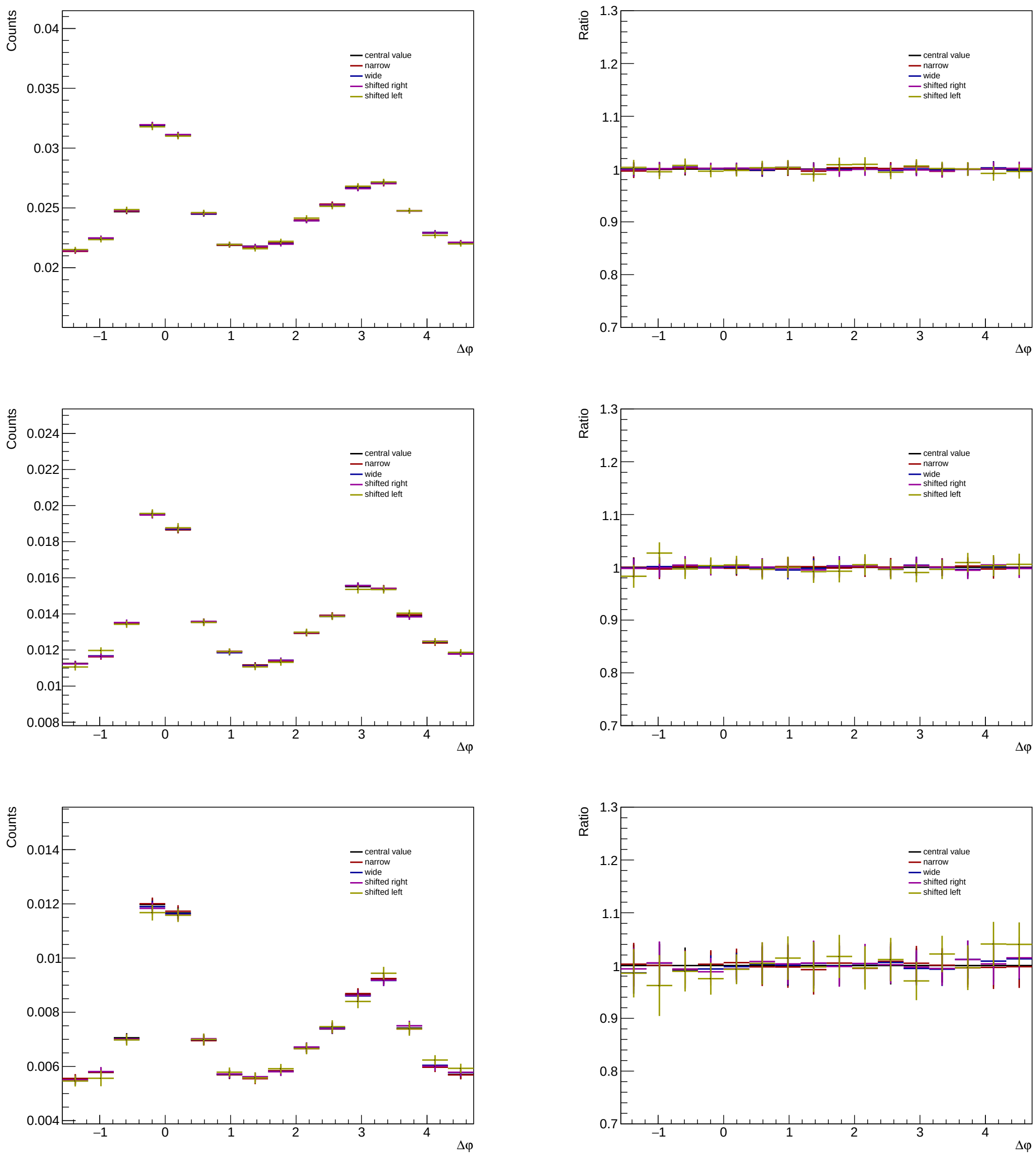

Figure 4.4: The h-Λ $\Delta\varphi$ distributions within the 0-20% (top), 20-50% (middle) and 50-80% (bottom) multiplicity bins in the higher associated p_{T} bin for each of the sideband region variations (left) with the ratios to the nominal distribution (right).

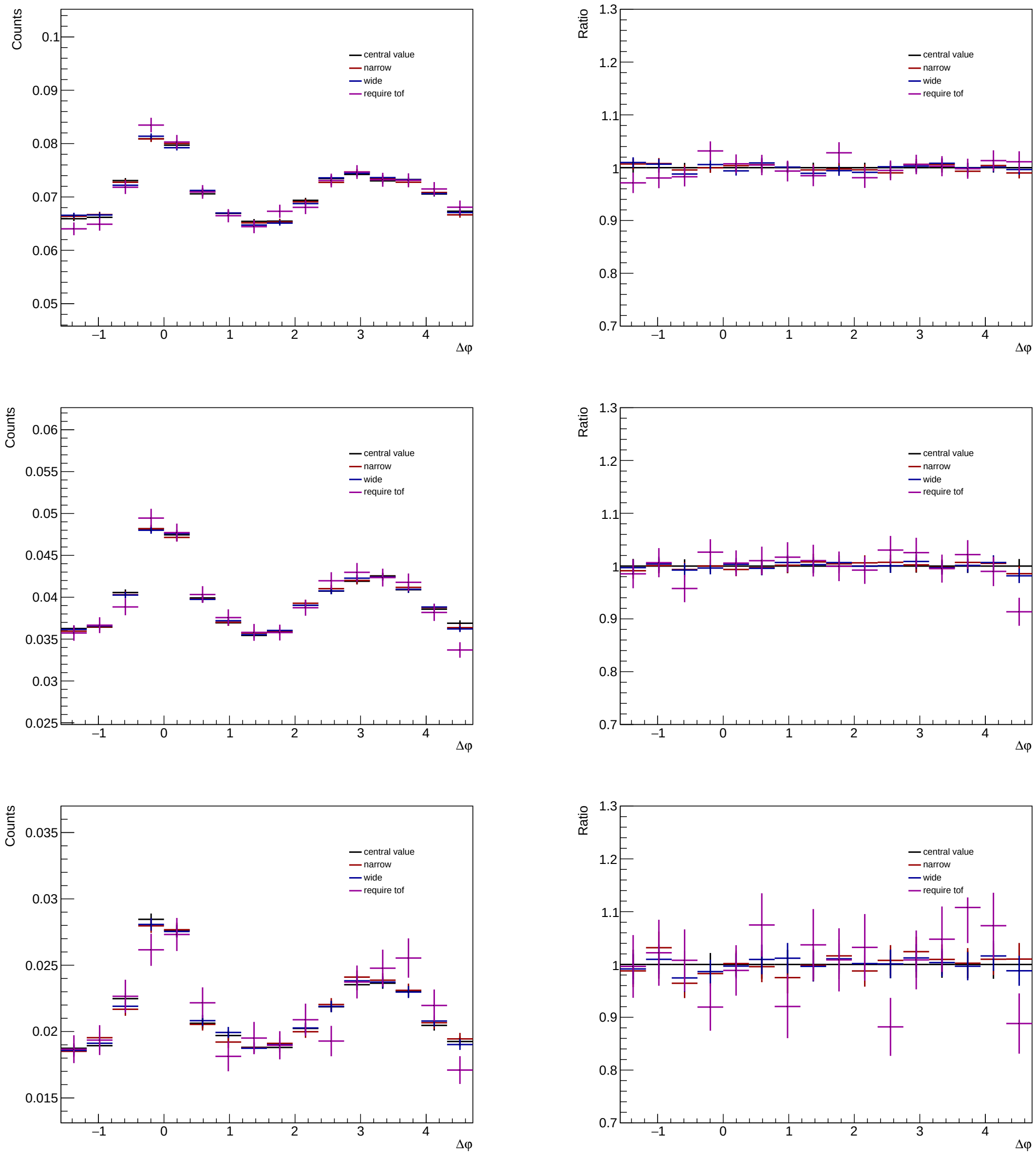

Figure 4.5: The h-Λ $\Delta\varphi$ distributions within the 0-20% (top), 20-50% (middle) and 50-80% (bottom) multiplicity bins in the lower associated p_{T} bin for each of the PID cut variations (left) with the ratios to the nominal distribution (right).

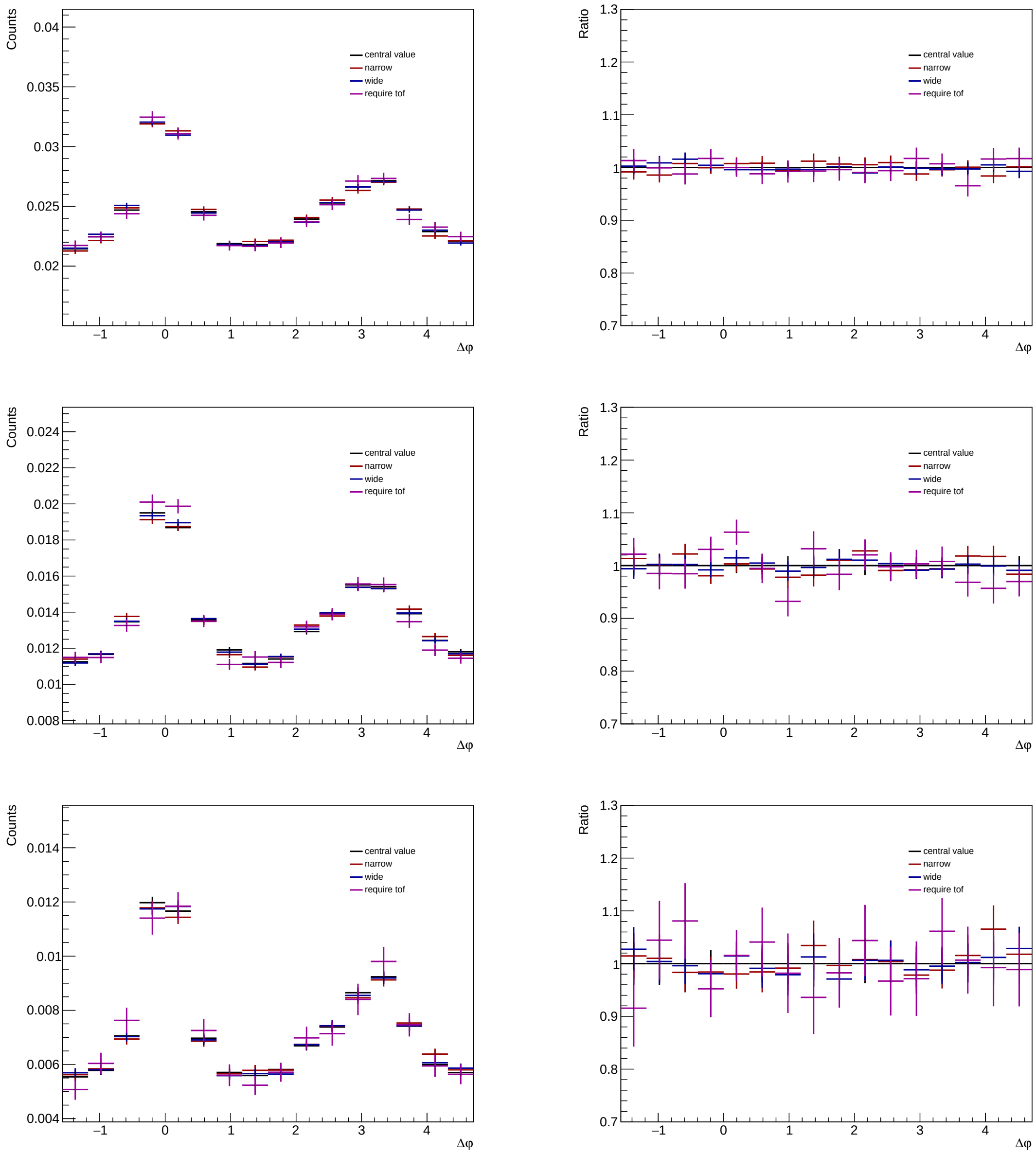

Figure 4.6: The h-Λ $\Delta\varphi$ distributions within the 0-20% (top), 20-50% (middle) and 50-80% (bottom) multiplicity bins in the higher associated p_{T} bin for each of the PID cut variations (left) with the ratios to the nominal distribution (right).

4.1.1.4 Barlow check for $\Delta\varphi$ distribution generation

Due to statistical fluctuations, it may be the case that some variations result in a statistically insignificant deviation from the nominal $\Delta\varphi$ distribution. In such cases, the variation should not be considered in the final systematic uncertainty calculation. To determine which variations give statistically significant deviations, a Barlow check [16] is performed. For each $\Delta\varphi$ bin, the following quantity is calculated:

$$N\sigma_{RB} := \frac{y_{\text{var.}} - y_{\text{nom.}}}{\sqrt{|\sigma^2_{\text{var.}} - \sigma^2_{\text{nom.}}|}}, \tag{4.1}$$

where $y_{\text{var.}}$ and $\sigma_{\text{var.}}$ are the measured yield and statistical uncertainty for the variation, and $y_{\text{nom.}}$ and $\sigma_{\text{nom.}}$ are the yield and statistical uncertainty for the nominal value.

To determine whether a given variation should be excluded, the number $\Delta\varphi$ bins that have $|N\sigma_{RB}| < 1$ is counted. If this is the majority of the bins (across all multiplicity and associated p_{T} ranges),the variation is excluded from the systematic calculation. Example plots of $N\sigma_{RB}$ for each variation of the signal, sideband and PID cuts are shown in Figure 4.7. The red lines represent $N\sigma_{RB} = \pm 1$.

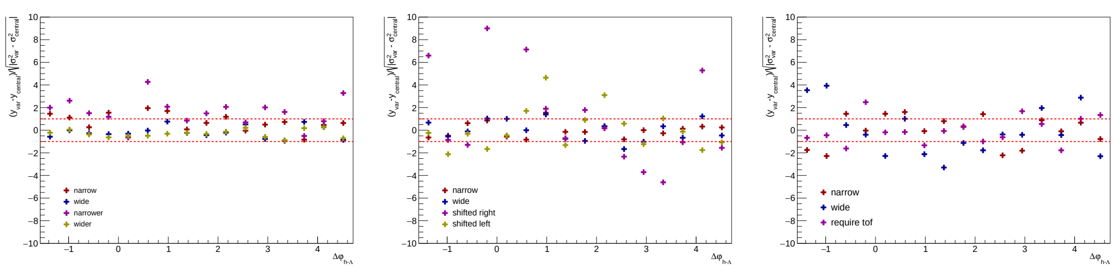

Figure 4.7: Barlow check for the signal (left), sideband (middle), and PID (right) variations in the 0-20% multiplicity bin. The red lines represent $N\sigma_{RB} = \pm 1$, and if the majority of the points fall within the red lines (across all $\Delta\varphi$, multiplicty and p_{T} bins), they are excluded from the systematic uncertainty calculation.

As a result of the check, the following variations are excluded from the final systematic uncertainty calculation:

- Signal: wide, wider
- Sideband: wide, narrow

- PID: require TOF

These exclusions are not so surprising. As the nominal signal region is already fairly wide, making it wider does not significantly change the $\Delta\varphi$ distribution. Similarly, the initial sideband region falls fairly close to the signal region. So long as there are enough statistics in the corresponding sideband h-Λ distribution, changing its width should not affect the $\Delta\varphi$ distribution in a meaningful way. It also appears that requiring a TOF hit introduces large statistical errors, which dominate the denominator in Equation 4.1.

4.1.1.5 $\Delta\varphi$ distribution systematics, summarized

The final systematic errors (after the Barlow check) from the h-Λ $\Delta\varphi$ distribution generation for each multiplicity bin and p_{T} bin are shown in Table 4.5. The total systematic uncertainty is calculated by adding each systematic error in quadrature. This table is consolidated into plots showing the systematic errors for each multiplicity bin and p_{T} bin, which are presented in Figure 4.8. As the systematic uncertainties associated with the generation of the dihadron $\Delta\varphi$ distributions are only from the tracking efficiency presented in Table 4.1, they are not plotted in this section.

Table 4.5: The final systematic uncertainties (in percentages) from the h-Λ $\Delta\varphi$ distribution generation for each multiplicity and associated p_{T} bin.

Mult. and p_{T} bin	Sig.	Sideband	PID	Topo. sel.	Mat. bud.	Total
0-20%, low p_{T}	0.36	0.53	0.64	3.2	1.1	3.3
20-50%, low p_{T}	0.35	0.67	0.65	3.2	1.1	3.4
50-80%, low p_{T}	0.76	1.1	1.4	3.2	1.1	3.8
0-20%, high p_{T}	0.42	0.42	0.76	3.0	0.6	3.2
20-50%, high p_{T}	0.4	0.71	1.2	3.0	0.6	3.3
50-80%, high p_{T}	1.1	1.6	2.0	3.0	0.6	4.1

The total systematic error is observed to be mostly p_T-independent. However, there appears to be a slight correlation between the systematic uncertainty and multiplicity, with the 0-20% bin exhibiting lower uncertainties than the 50-80% bin across both p_{T} ranges. This can become problematic when investigating the multiplicity dependence of observables extracted from the $\Delta\varphi$ distributions, as the fraction of the systematic uncertainty which is directly correlated with multiplicity should not be considered when measuring multiplicity-dependent trends like slopes and percent

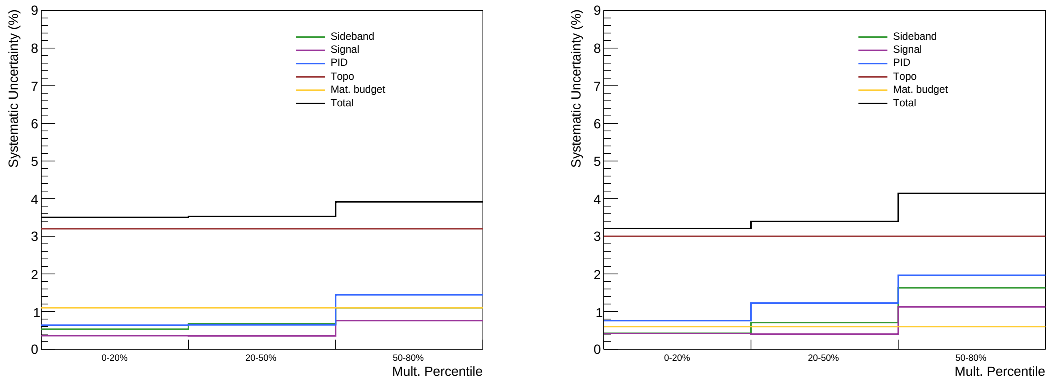

Figure 4.8: A visual depiction of the final systematic errors for the h-Λ $\Delta\varphi$ distributions for each multiplicity bin in the low (left) and high (right) associated p_{T} bins. The total systematic error is shown in black.

changes. Because of this, the fraction of the systematic uncertainty which is uncorrelated with multiplicity is approximated using

$$\sigma^2_{\mathrm{uncor},i} = \sum_{\mathrm{vars}} (R_{\mathrm{var},i} - 1)^2, \tag{4.2}$$

where

$$R_{\mathrm{var},i} = \left(\frac{y_{\mathrm{var},i}}{y_{\mathrm{nom},i}}\right) / \left(\frac{y^{MB}_{\mathrm{var}}}{y^{MB}_{\mathrm{nom}}}\right), \tag{4.3}$$

where "i" refers to the ith multiplicity bin, and "MB" refers to the min-bias (multiplicity-integrated) results. The deviations of $R_{\mathrm{var},i}$ from unity quantify how the deviations in multiplicity bin i differ from those in the MB sample. $\sigma_{\mathrm{uncor},i}$ is computed for each $\Delta\varphi$ bin, then the RMS is taken across all $\Delta\varphi$ bins to obtain the final multiplicity-uncorrelated portion of the systematic errors. The results for each p_{T} bin are shown in Figure 4.9. These systematic errors are only used when quantifying the multiplicity dependence of an observable extracted from the $\Delta\varphi$ distributions.

4.1.2 Yield extraction

One of the largest sources of systematic uncertainty of this analysis corresponds to the different techniques that can be used to extract the yields in the near-side jet, away-side jet and underlying event from the $\Delta\varphi$ distributions. As mentioned in Section **??**,

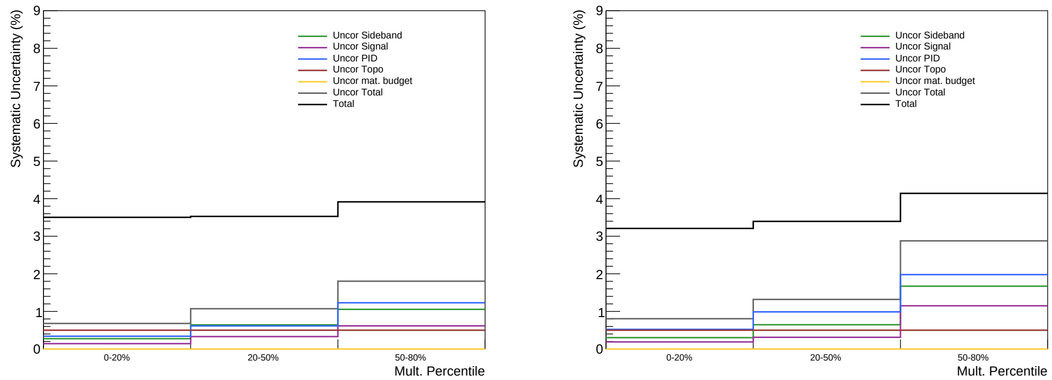

Figure 4.9: Visual depiction of the multiplicity-uncorrelated systematic errors for the h-Λ $\Delta\varphi$ distributions for each multiplicity bin in the low (left) and hig (right) associated p_{T} bins, along with the total systematic error shown in black.

the equations for extracting these yields are

$$Y_{near} = \int_{-\pi/2}^{\pi/2} (\frac{dN}{d\Delta\varphi} - U(\Delta\varphi))d\Delta\varphi, \quad Y_{away} = \int_{\pi/2}^{3\pi/2} (\frac{dN}{d\Delta\varphi} - U(\Delta\varphi))d\Delta\varphi \quad (4.4)$$

$$Y_{UE} = \int_{-\pi/2}^{3\pi/2} U(\Delta\varphi)d\Delta\varphi, \quad (4.5)$$

where $\frac{dN}{d\Delta\varphi}$ is the $\Delta\varphi$ distribution and $U(\Delta\varphi)$ is the underlying event fit. As the $\Delta\varphi$ distribution is present in these equations, all of the previous variations concerning the generation of this distribution must be considered. However, these equations also naturally introduce two new categories of systematic uncertainty: those associated with the underlying event fit, and those associated with the integration of the $\Delta\varphi$ distribution. Both of these categories will be discussed in detail in the following sections.

4.1.2.1 Underlying event fit techniques

As the underlying event term $U(\Delta\varphi)$ is present in every yield extraction equation above, any changes in the underlying event fitting procedure will affect the final yield measurements. To maintain compatibility with previous analyses (specifically for the dihadron correlations), the nominal underlying event fit is a straight line to the average of the $\Delta\varphi$ distribution in the ranges $[-\frac{\pi}{2}, -\frac{\pi}{4}) \cup [\frac{\pi}{4}, \frac{5\pi}{8}) \cup [\frac{11\pi}{8}, \frac{3\pi}{2})$. These ranges were initially chosen as there is expected to be little-to-no contamination from the jet components in each range. However, to investigate the effect the UE fitting procedure may have on the final yields, the following alternative methods were considered:

1. Straight line fit in a more restricted range, specifically $[-\frac{\pi}{2}, -\frac{3\pi}{8}) \cup [\frac{3\pi}{8}, \frac{5\pi}{8}) \cup [\frac{11\pi}{8}, \frac{3\pi}{2})$
2. Straight line fit using the Zero Yield At Minimum (ZYAM) technique, where the underlying event line is set to the minimum of the $\Delta\varphi$ distribution
3. Sinusoidal fit which includes a non-zero v_2 contribution

The first two techniques are similar enough to the nominal technique that they will not be explicitly shown in this section. Restricting the range of the flat fit region results in deviations from the nominal procedure of around 2%, whereas the ZYAM technique gives much larger deviations at about 15%. Ultimately the ZYAM procedure is not included in the final systematics calculation due to a physical incompatibility, whereby the presence of v_2 in the higher multiplicity $\Delta\varphi$ distributions causes the ZYAM procedure to massively underestimate the underlying event contribution.

Including a non-zero v_2 contribution is a much more involved procedure and requires new machinery to be developed, so it will be described in detail in the next section.

4.1.2.2 Including a non-zero v_2 contribution

All of the "straight line" UE fitting techniques are based on the flatness assumption of the non-jet part of the correlation in $\Delta\varphi$. This means that the dijet axis direction does not affect the non-jet particle distribution's overall shape within an event. However, as mentioned in Section **??**, previous Pb–Pb, p–Pb and even pp collision studies have shown that the QGP's collective flow components (v_1, v_2, etc.) influence the phase-space distribution of particles within an event. Using Fourier decomposition, the $\Delta\varphi$ distributions on an event-by-event basis can be written as

$$\frac{dN}{d\Delta\varphi} = a_0 + \sum_{n=1}^{\infty} 2a_n cos(n\Delta\varphi), \tag{4.6}$$

where a_n are the Fourier coefficients. Surprisingly, these coefficients have been shown **Justin108**, **Justin109**, **Justin110** to be related to the collective flow coefficients v_n via

$$v_n = \frac{a_n}{a_0}. \tag{4.7}$$

Table 4.6: v_2 values used in this analysis for each associated p_{T} bin. The values were calculated as the weighted average of published p_{T}-differential v_2 measurements with the published p_{T} spectra, taken across the entire associated p_{T} range.

$p_T^{\text{assoc.}}$	$v_2^{\text{trig.}}$	$v_2^{\text{assoc. h}}$	$v_2^{\text{assoc.}\Lambda}$
1.5 - 2.5	0.092	0.100	0.075
2.5 - 4.0	0.092	0.119	0.137

This means that even without reconstructing the reaction plane within a specified event, the effects of collective flow are present in the $\Delta\varphi$ distributions. This manifests in the correlation distributions as an underlying event which is not flat with respect to $\Delta\varphi$, but rather sinusoidal. While this is in direct conflict to the initial assumption of a flat underlying event, this nominal choice was made to maintain compatibility with previous measurements of dihadron yields using correlation techniques, which also assume a flat UE in $\Delta\varphi$.

As the v_2 or "elliptic flow" coefficient is the most dominant of the collective flow coefficients measured in p–Pb collisions **Justin111** in the p_{T} ranges for this analysis, it is the only one considered. Furthermore, the v_2 coefficients are exceedingly difficult to determine, with fully published papers solely dedicated to measuring the v_2 for different particle species and collision systems. Luckily, these coefficients have been measured by ALICE in p–Pb collisions for both charged hadrons and Λ baryons across a wide range of p_{T} [20], [21]. As the p_{T} binning in this analysis is much wider, the weighted average

$$v_2^{avg} = \frac{\int_{p_{T,min}}^{p_{T,max}} v_2(p_T)\frac{dN}{dp_T}dp_T}{\int_{p_{T,min}}^{p_{T,max}} \frac{dN}{dp_T}dp_T}, \tag{4.8}$$

is used, where $p_{T,min}$ and $p_{T,max}$ are the minimum and maximum values of p_{T} in the bins from this analysis (namely $1.5 - 2.5$ and $2.5 - 4.0$ GeV/c). The $v_2(p_{\mathrm{T}})$ values for charged hadrons and Λ baryons are taken from [20], and dN/dp_T is taken from the published p_{T} spectra for charged hadrons and Λ baryons from **PtSpectra**, plots of which can be seen in Figures 4.10 (v_2) and 4.11 (p_{T} spectra). The values of v_2^{avg} for each p_{T} bin are shown in Table 4.6. Note that the trigger v_2 remains the same, as the trigger p_{T} range is fixed for this analysis. The Λ v_2 is markedly higher than the charged hadron v_2, which ultimately manifests itself as a larger deviation from the nominal UE fit when compared to the dihadron case. Unfortunately there are few multiplicity-dependent measurements of the v_2 coefficients for identified particle species. Because of this, the v_2 values from Table 4.6 are used only in the 0-20% multiplicity bin, with the v_2 values for the 20-50% and 50-80% multiplicity bins taken as 0.85 and 0.50 times the 0-20% value, respectively.

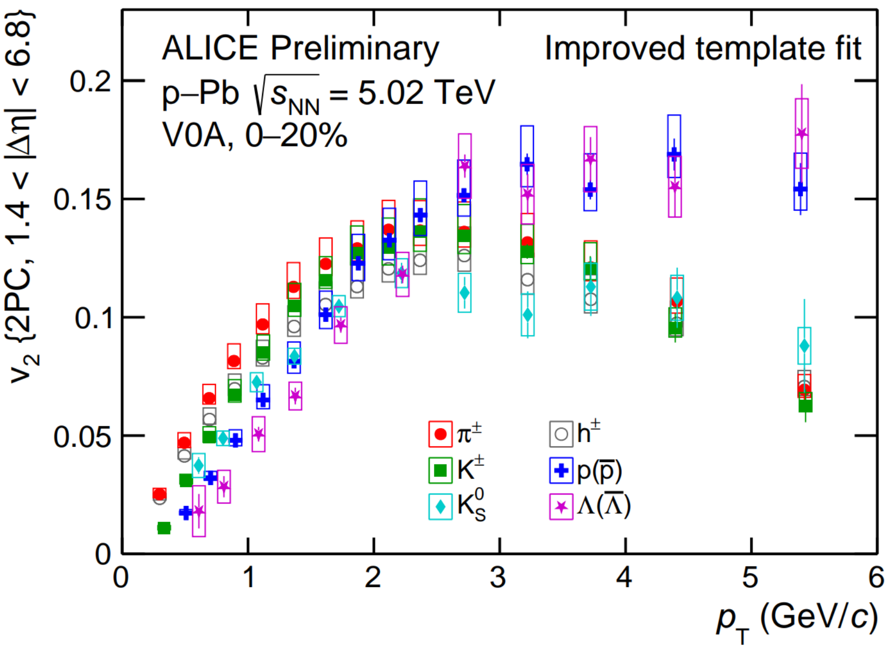

Figure 4.10: The v_2 values for identified hadrons as a function of p_T, taken from [20].

Using these v_2 values, the underlying event is estimated by fitting the function

$$U_{v_2}(\Delta\varphi) = A \times (1 + 2v_2^{\text{trig.}} v_2^{\text{assoc.}} cos(2\Delta\varphi)) \tag{4.9}$$

in the ranges $-\pi/2 < \Delta\varphi < -1$ and $1 < \Delta\varphi < +\pi/2$, where little jet contribution is expected. The underlying event **pedestal** A is allowed to vary during the fit, but the v_2 values are fixed. Examples of h-Λ and h-h $\Delta\varphi$ distributions with the UE fit using this procedure are shown in Figure 4.12.

The validty of this procedure can be tested by examining the $\Delta\varphi$ distributions at large $\Delta\eta$, where the near-side jet component is minimal, leaving just the UE at small $\Delta\varphi$[1]. In fact, this procedure is often used to determine the v_2 coefficients in the first place. In this case, however, it will just be used to serve as a sanity check for both the fitting procedure and the fixed v_2 coefficients from 4.6. If the UE fit

[1] At large $\Delta\varphi$, the away-side ridge is still present.

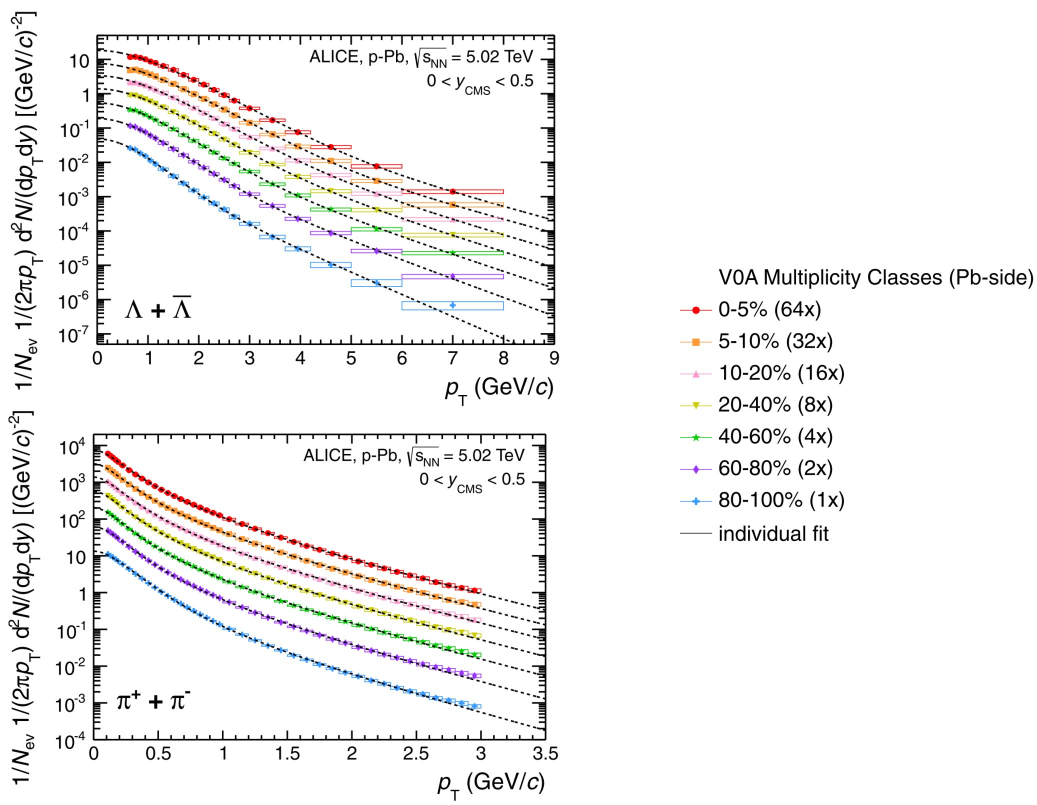

Figure 4.11: The published [18] p_{T} spectra for Λ baryons (top) and charged hadrons ($\approx$ pions) (bottom), used to compute the weighted average of the v_2 coefficients across the wide momentum bins used in this analysis.

matches the near-side of the $\Delta\varphi$ distribution at large $\Delta\eta$, then the v_2 coefficients and fitting procedure are likely valid. Examples of the $\Delta\varphi$ distributions with $|\Delta\eta| > 1.4$ and $|\Delta\eta| < 1.2$ showing the v_2-based UE fit can be seen in Figure 4.13. These are generated in the highest multiplicity and momentum bins, where the effects of the v_2 contribution are maximal. Both the h-Λ and h-h $\Delta\varphi$ distributions show good agreement between the UE fit and the data at small $\Delta\varphi$ and large $\Delta\eta$, where the near-side jet peak and away-side ridge are no longer present, pointing to the validity of the v_2-based UE fitting procedure.

The effects of including v_2 has on the extracted h-Λ and h-h yields in each region is not at all obvious at first glance. For the most central collisions, the inclusion of v_2 results in nearly a 5% decrease for the jet-like yields when compared to the nominal technique. This can mostly be seen in Figure 4.12, where the peaks of the sinusoidal fit achieve their maxima within the near- and away-side components

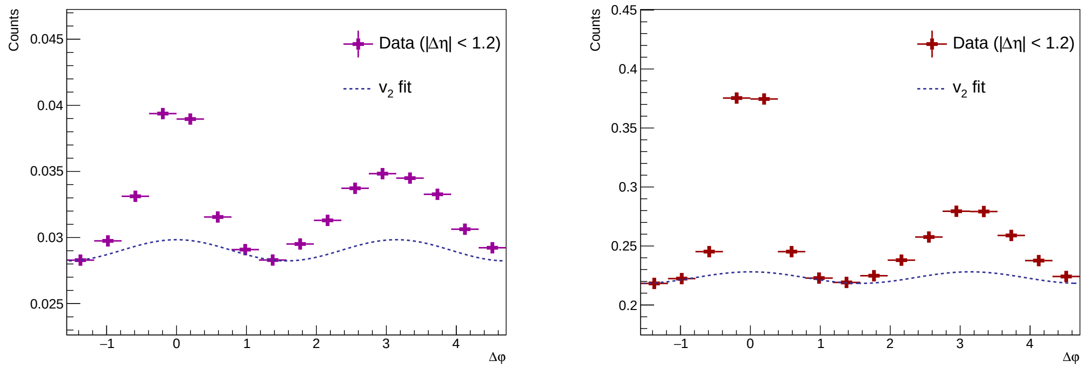

Figure 4.12: Examples of the underlying event fit using the v_2-based procedure for the h-Λ (left) and h-h (right) $\Delta\varphi$ distributions in the 0-20% multiplicity bin in the higher associated p_{T} bin.

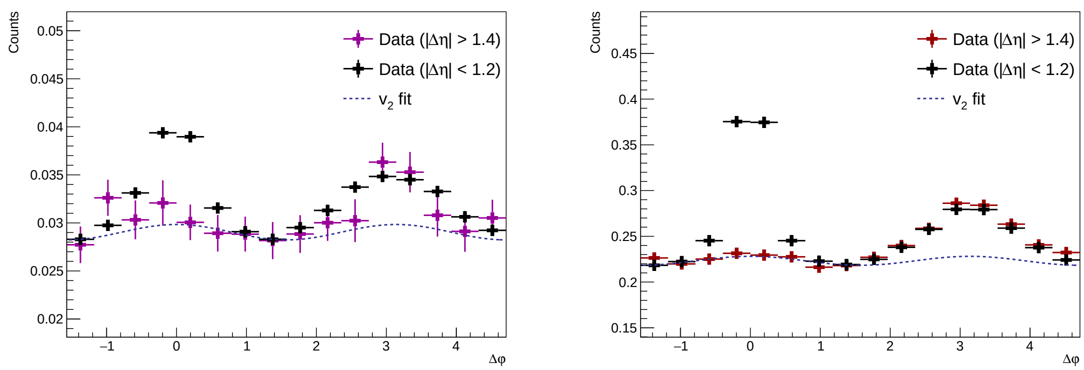

Figure 4.13: The h-Λ (left) and h-h (right) $\Delta\varphi$ distributions in the 0-20% multiplicity bin and higher p_{T} bin at small and large values of $\Delta\eta$, with the UE fit using the v_2-based procedure shown in blue. The fits are in good agreement with data in both cases.

of the jet, causing the overall yields to be lower than those obtained by the flat UE assumption. However, at lower multiplicities (20-50%, 50-80%), the extracted h-Λ and h-h jet-like yields actually exhibit a slight increase of around 5% in their extracted yields when compared to those measured using the nominal UE fit. This is due to the variation of the pedestal A in Equation 4.9 during the fit, which results in a smaller pedestal value than the nominal fit in these multiplicity ranges. The extracted underlying event yield never deviates by more than 3% from the yield obtained using the nominal procedure for all multiplicity and momentum bins for both the h-Λ and h-h cases.

4.1.2.3 Integration procedures

The general yield-extraction equation

$$Y_{\Delta\varphi} = \int_{\Delta\varphi_1}^{\Delta\varphi_2} (\frac{dN}{d\Delta\varphi} - U(\Delta\varphi))d\Delta\varphi \tag{4.10}$$

leaves some room for interpretation. Obviously the $\Delta\varphi$ distributions shown thus far are in some way related to $dN/d\Delta\varphi$, but integrals prefer continuous integrands, which the $\Delta\varphi$ distributions are clearly not as they have finitely many (16) bins. Furthermore, there is nothing explicity preventing

$$\frac{dN}{d\Delta\varphi} < U(\Delta\varphi), \tag{4.11}$$

possibly resulting in a *negative* yield, which is clearly unphysical. There are a few ways to alleviate these issues, which are discussed in this section.

For all of the yield extraction procedures discussed thus far, the usage of the integration symbol in Equation 4.10 is *slightly* misleading: the yields are actually calculated by summing the bin contents of the $\Delta\varphi$ distribution in the specified range, and subtracting off the value of $U(\Delta\varphi)$ at the center of each bin. To be more explicit, the yields are calculated as

$$Y_{\Delta\varphi} = \sum_{i=L}^{U} (\frac{dN}{d\Delta\varphi_i} - U(\Delta\varphi_i)), \tag{4.12}$$

where L and U are the bin numbers of the Lower and Upper $\Delta\varphi$ bins in the specified range, $dN/d\Delta\varphi_i$ is the value of the correlation distribution in the ith $\Delta\varphi$ bin, and $U(\Delta\varphi)$ is the value of U in the center of the ith $\Delta\varphi$ bin.

Equation 4.12 provides an easy way to deal with the negative yield issue: if the value of $U(\Delta\varphi_i)$ is greater than the value of $dN/d\Delta\varphi_i$ in a given bin, the yield in that bin is set to zero. While this is not done for the nominal yield extraction procedure in this analysis, it is a completely reasonable technique and is therefore explored in the systematic uncertainty analysis. Using the flat UE assumption with the UE average taken in the nominal range, the results are relatively unsurprising: the yields extracted using this procedure are strictly higher than those extracted using the main procedure where negative contributions are allowed. However, the deviations never exceed more than 3.5%, with the average deviation being around 2% for both the h-Λ and h-h cases.

Another way to address the lack of continuity in the $\Delta\varphi$ distributions is to fit these distributions with continuous functions, then use the corresponding fit for the integration in Equation 4.10. This thesis considers two such functions, which are presented in the following two sections.

4.1.2.4 The double Gaussian fit

There are a number of functions that may appear suitable to fit the $\Delta\varphi$ distributions, but given the Gaussian-like appearance of the near- and away-side jet components, a double Gaussian fit is a natural choice. The double Gaussian fit function is given by

$$\begin{aligned} f(\Delta\varphi) = U + A_{\mathrm{NS}} e^{\frac{(\Delta\varphi-\mu_{\mathrm{NS}})^2}{2\sigma_{\mathrm{NS}}}} + A_{\mathrm{AS}} e^{\frac{(\Delta\varphi-\mu_{\mathrm{AS}})^2}{2\sigma_{\mathrm{AS}}}} \\ + A_{\mathrm{NS}}^{\mathrm{mirror}} e^{\frac{(\Delta\varphi-\mu_{\mathrm{NS}}+2\pi)^2}{2\sigma_{\mathrm{NS}}}} + A_{\mathrm{AS}}^{\mathrm{mirror}} e^{\frac{(\Delta\varphi-\mu_{\mathrm{AS}}-2\pi)^2}{2\sigma_{\mathrm{AS}}}}, \end{aligned} \tag{4.13}$$

where A and μ are the amplitude and means of the Gaussian components, and the subscript "NS" ("AS") refers to the near-side (away-side) jet component. The "mirror" terms are added to account for the 2π periodicity of the $\Delta\varphi$ distribution, and are required to obtain a convergent fit. The U term describes a flat underlying event, and is fixed to the average of the $\Delta\varphi$ distribution in the regions $[-\frac{\pi}{2}, -\frac{\pi}{4}) \cup [\frac{\pi}{4}, \frac{5\pi}{8}) \cup [\frac{11\pi}{8}, \frac{3\pi}{2})$, as is done for the nominal UE determination procedure. Furthermore, the mean in the near-side gaussian (and corresponding mirror term) is fixed to 0 (2π) and the mean in the away-side guassian (and corresponding mirror term) is fixed to π ($-\pi$), leaving only the amplitudes and widths to vary freely. The double Gaussian fits to both the h-Λ and h-h correlation distributions for every multiplicity and momentum bin are shown in Figures 4.14 (h-Λ) and 4.15. The fits generally describe the data quite well, though an extreme amount of effort went in to ensuring the convergence of each fit due to an inordinate amount of instability.

The yields extracted using the double Gaussian fit are nearly identical to those extracted using the nominal bin-wise integration procedure, with deviations from the nominal procedure never exceeding 1% for either the h-Λ or h-h cases. This indicates two things:

1. The fits describe the data quite well, and
2. The differences between Equations 4.10 and 4.12 are mostly aesthetic, so long as (1) holds and the choice of $U(\Delta\varphi)$ is consistent.

As the deviations are so small, this procedure ends up excluded from the final systematic uncertainty calculation after the Barlow check in Section 4.1.2.6, but the fits are still used for the systematic studies involving the near- and away-side jet widths discussed in Section 4.1.3.

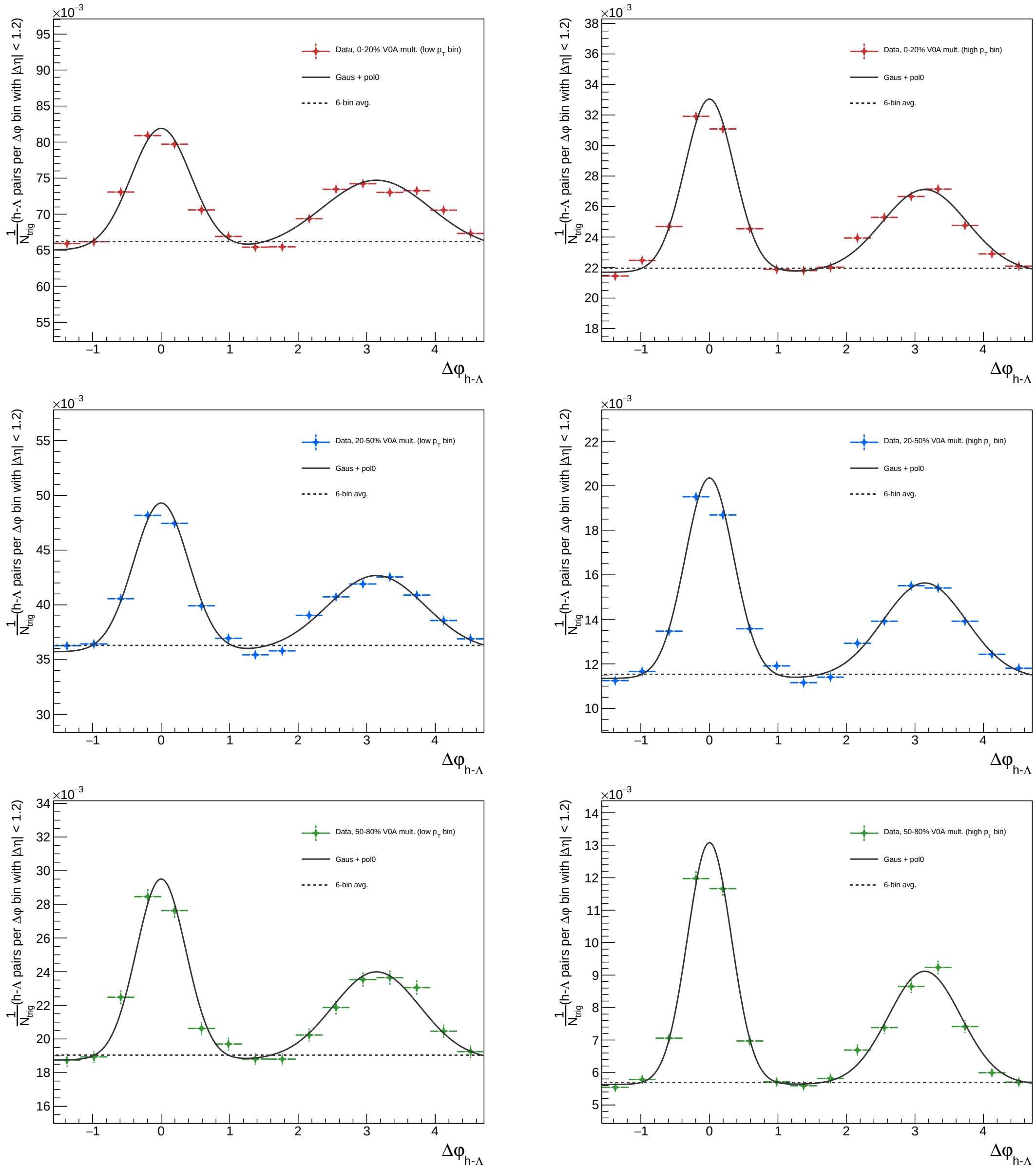

Figure 4.14: The final per-trigger h-Λ $\Delta\varphi$ correlation distributions with the full double Gaussian fit for the 0-20% (top), 20-50%(middle) and 50-80% (bottom) multiplicity bins in the lower (left) and higher (right) associated $p_{\rm T}$ bins. The UE fit is also shown as a dashed line.

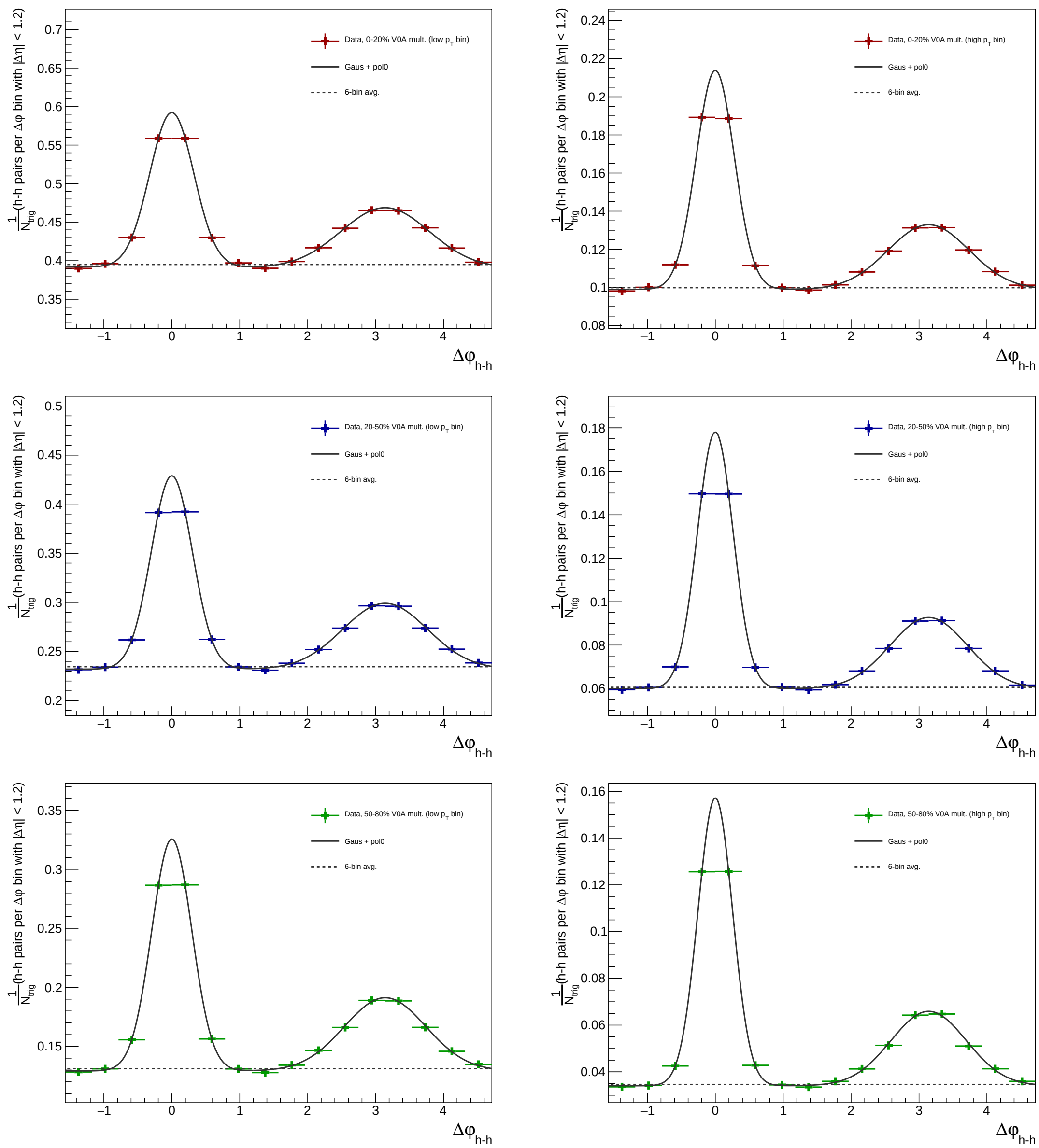

Figure 4.15: The final per-trigger h-h $\Delta\varphi$ correlation distributions with the full double Gaussian fit for the 0-20% (top), 20-50%(middle) and 50-80% (bottom) multiplicity bins in the lower (left) and higher (right) associated p_{T} bins. The UE fit is also shown as a dashed line.

4.1.2.5 The von Mises fit

While only briefly mentioned in Section **??** in the context of extracting the near- and away-side jet widths, the von Mises distribution is another natural choice for fitting the $\Delta\varphi$ distributions due to its combined Gaussian-like behaviour while naturally exhibiting 2π-periodicity (which was "forced" onto the double Gaussian fit via the mirror terms). As a reminder, the von Mises fit function is given by

$$f(\Delta\varphi) = U(\Delta\varphi) + \frac{A_{\mathrm{NS}}}{2\pi I_0(k_{\mathrm{NS}})} e^{k_{\mathrm{NS}} cos(\Delta\varphi - \mu_{\mathrm{NS}})} + \frac{A_{\mathrm{AS}}}{2\pi I_0(k_{\mathrm{AS}})} e^{k_{\mathrm{AS}} cos(\Delta\varphi - \mu_{\mathrm{AS}})}, \tag{4.14}$$

where A and μ are as they were in Equation 4.13, and k is a measure of the collimation of the distribution, which is inversely related to the width through

$$\sigma = \sqrt{-2 \ln \frac{I_1(\kappa)}{I_0(\kappa)}}. \tag{4.15}$$

In these equations, I_n refers to the modified Bessel function of the nth kind. Note that the $U(\Delta\varphi)$ has been given explicit $\Delta\varphi$ dependence, as this fit function does not require the UE component to be flat with respect to $\Delta\varphi$ in order to converge nicely.

During the fitting procedure, the means μ_{NS} and μ_{AS} are again fixed to 0 and π, respectively, and the $U(\Delta\varphi)$ term is fixed to the function obtained by fitting the UE which includes a non-zero v_2 contribution, as described in Section 4.1.2.2. While the fitting of this function is much more stable than the aforementioned double Gaussian function–possibly allowing for the variation of U during the fit–the term is ultimately fixed due to an interesting feature of the von Mises distribution, which is discussed in 4.1.3. The von Mises fits to both the h-Λ and h-h correlation distributions for every multiplicity and momentum bin are shown in Figures 4.16 (h-Λ) and 4.17. Again, the fits describe the data very well. Furthermore, the fits are extremely stable, which is a welcome change from the double Gaussian fits and was the initial motivation for the width analysis presented in this thesis.

Given these fits are taken with a different choice of $U(\Delta\varphi, \Delta\eta)$, the extracted yields from the von Mises function deviate from the nominal extraction procedure by a relatively large amount, with both the h-Λ and h-h jet-like yields seeing a decrease of around 5%. This percentage is familiarly the same as the percent deviation seen in Section 4.1.2.2 from the h-Λ and h-h yields when using the v_2-based UE fit while still using bin-wise summation to extract the yields. In fact, all of the yields extracted using the von Mises fitting procedure are nearly identical to the yields extracted using the v_2-based UE fit with bin-wise summation, again indicating that the data are well described by the fits. As these two procedures are nearly identical in their results, the von Mises fitting procedure is also excluded from the final systematic uncertainty calculation for the yield extraction after the Barlow check in Section 4.1.2.6. However, the fits are so incredibly well-behaved that they spawned the initial investigation into the near- and away-side jet widths, which eventually became a major topic of interest in this thesis[2].

4.1.2.6 Barlow check for yield extraction

Following the same procedure as outline in Section 4.1.1.4, a Barlow check is performed for the different techniques for extracting the per-trigger yields from Equations 4.4 and 4.5. If the majority of the measured h-Λ yields for a given variation have $|N\sigma_{RB}| < 1$, that variation is excluded from the systematic uncertainty calculation. This majority is calculated across all kinematic regions (near-side jet, away-side jet, underlying event), multiplicity bins and associated momentum bins. While the h-h yields were initially considered for this check, their statistical errors are so small that the denominator in Equation 4.1 is close to zero, resulting in erratic $N\sigma_{RB}$ values. Thus any technique which gets excluded for the h-Λ yields will also be excluded for the h-h yields. Examples of the Barlow check for the yield extraction are shown in Figure 4.18.

As a result of the Barlow check, the following variations are excluded from the systematic uncertainty calculation:

- The double Gaussian fit procedure
- The von Mises fit procedure

These exclusions were foreshadowed in the previous sections, as the fits describe the data well enough that there are no statistically significant differences between the yields extracted using these fit functions and the yields extracted using bin-wise summation.

[2]Systematic uncertainty calculations involving misbehaving fits are a nightmare.

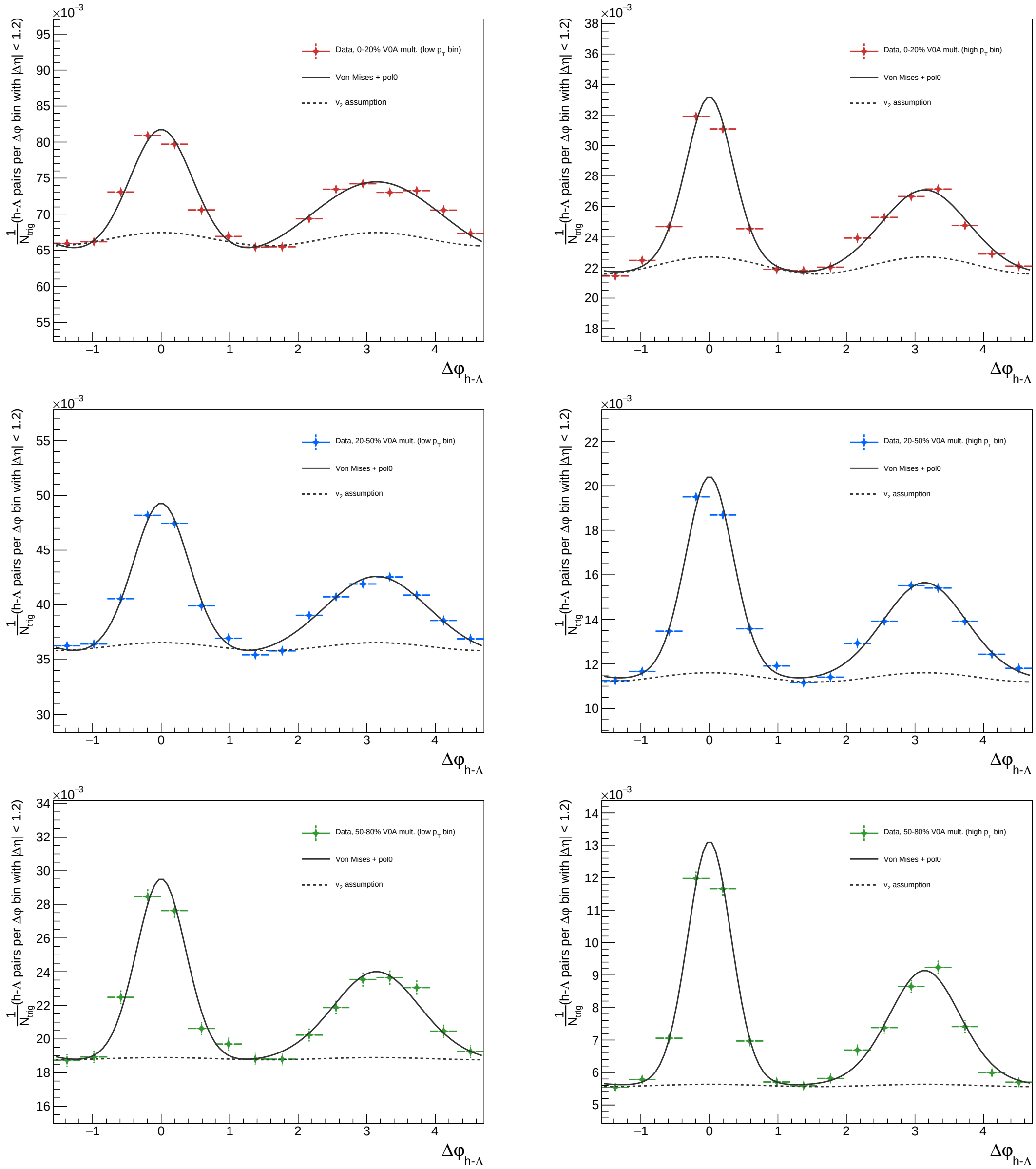

Figure 4.16: The final per-trigger h-Λ $\Delta\varphi$ correlation distributions with the von Mises fit for the 0-20% (top), 20-50%(middle) and 50-80% (bottom) multiplicity bins in the lower (left) and higher (right) associated p_{T} bins. The UE fit with v_2 contribution is also shown as a dashed line.

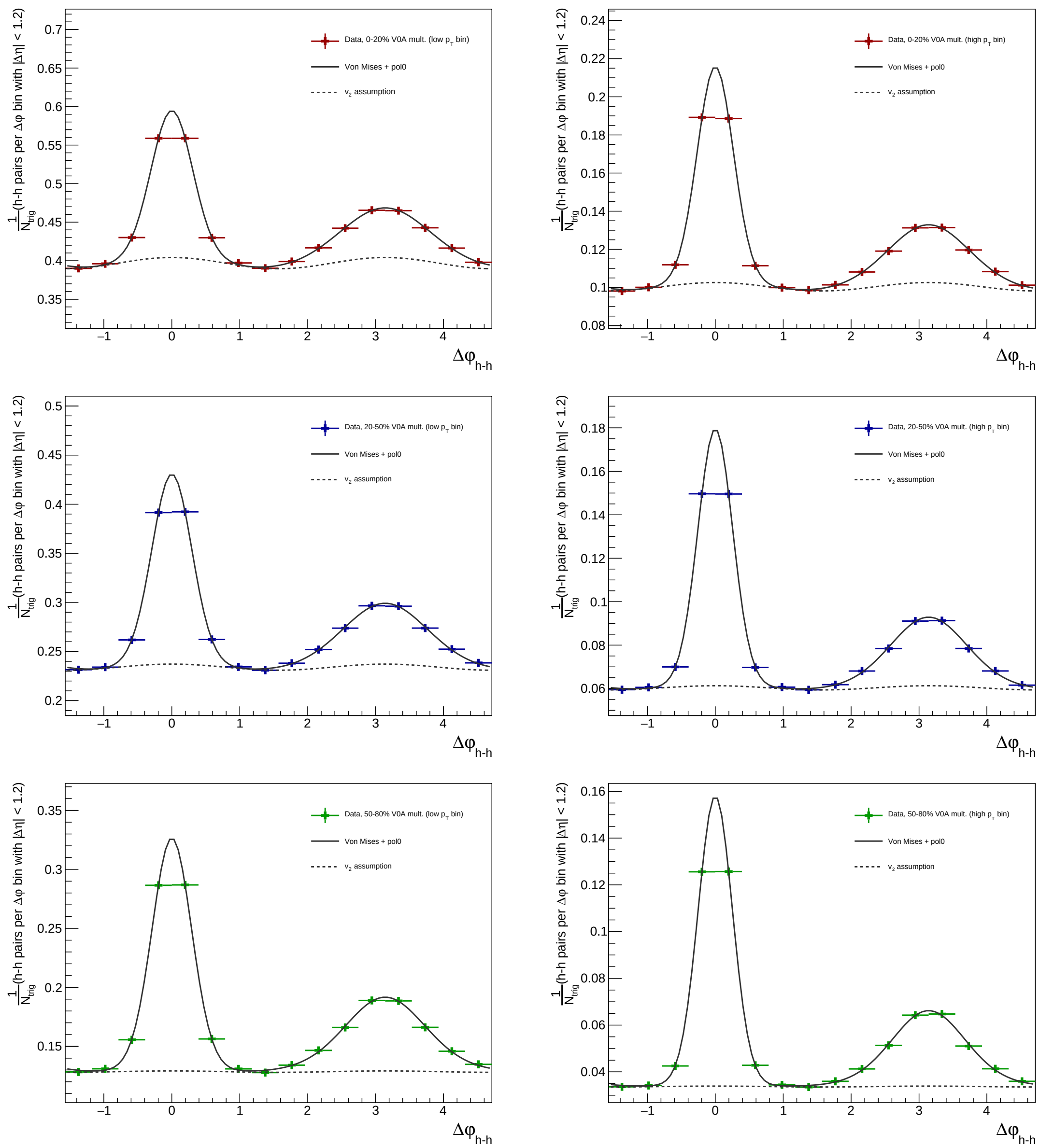

Figure 4.17: The final per-trigger h-h $\Delta\varphi$ correlation distributions with the von Mises fit for the 0-20% (top), 20-50%(middle) and 50-80% (bottom) multiplicity bins in the lower (left) and higher (right) associated p_{T} bins. The UE fit with v_2 contribution is also shown as a dashed line.

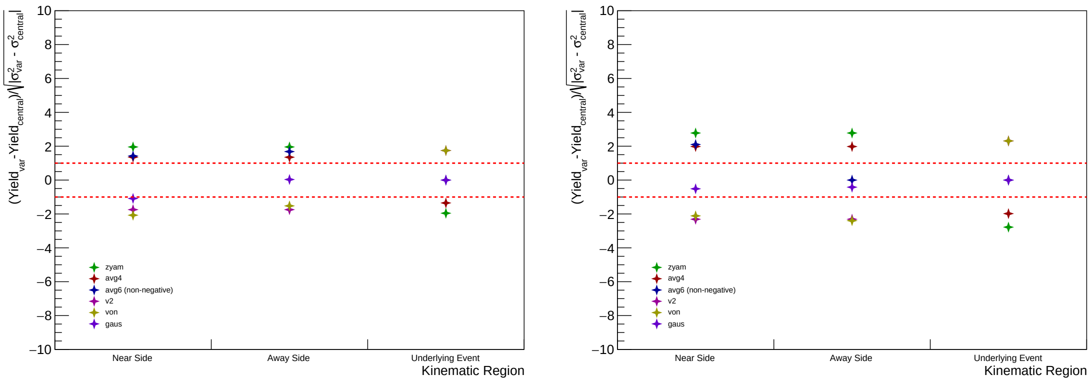

Figure 4.18: The Barlow check for the yield extraction procedure in the 0-20% multiplicity bin for the lower (left) and higher (right) associated p_{T} bins. The red lines represent $N_{\sigma_{RB}} = \pm 1$, and if the majority of the points from a given procedure fall within these lines (across all multiplicity and momentum bins), the procedure is excluded from the systematic uncertainty calculation.

4.1.2.7 Yield extraction systematics, summarized

As most of the main results of this thesis involve the h-Λ and h-h per-trigger yields in the various kinematic regions, the systematic uncertainties associated with the extraction of these yields deserve to be consolidated to concise tables and plots from the overly detailed descriptions of the previous sections. To that end, plots demonstrating the resulting yield deviations from the nominal technique for each of the aforementioned yield extraction procedure variations (post Barlow check) can be seen in Figures 4.19 (h-Λ) and 4.20 (h-h). Furthermore, tables containing the final systematic uncertainties for both the h-Λ and h-h per-trigger yields in each kinematic region for every multiplicity and associated p_{T} bin can be seen in Tables 4.7 (h-Λ) and 4.8 (h-h). Note that included in these systematic uncertainties are both the technique variations associated with the yield extraction procedure, as well as the variations in the yields due to the variations in the $\Delta\varphi$ distributions themselves (after the Barlow check), as discussed in Section 4.1.1. The UE yield systematic uncertainties are generally much lower than the jet-like yields, averaging around 3.5% for both the h-Λ and h-h cases. The larger uncertainties for the jet-like yields (4-7%) are primarily due to the fact that the jet-like yield extraction techniques rely both on the integration procedure and the choice of $U(\Delta\varphi)$, where both including v_2 and excluding negative yield contributions can have a large effect on these extracted yields. Both of those choices have little effect (or no effect in the case of the non-negative yield requirement) on the integral of the $U(\Delta\varphi)$ across the entire azimuthal range (i.e. the UE yield).

As was the case in Section 4.1.1.5, the portion of systematic uncertainty which is uncorrelated with multiplicity is computed using Equations 4.2 and 4.3 and presented in Tables 4.9 (h-Λ) and 4.10. Whenever the trends of these yields with respect to multiplicity are measured (either by taking slopes or looking at percent differences), the errors are always calculated using these multiplicity-uncorrelated systematic uncertainties.

Table 4.7: Final systematic errors (in %) for the per-trigger h-Λ yields in each kinematic region, multiplicity and momentum bin.

Mult. and p_{T} bin	Near-side (jet)	Away-side (jet)	UE
0-20%, low	5.50e+00	5.57e+00	3.12e+00
20-50%, low	4.94e+00	5.24e+00	3.22e+00
50-80%, low	6.34e+00	7.19e+00	3.68e+00
0-20%, high	5.47e+00	6.10e+00	3.15e+00
20-50%, high	5.88e+00	6.54e+00	3.33e+00
50-80%, high	4.75e+00	5.25e+00	3.72e+00

Table 4.8: Final systematic errors (in %) for the h-h per-trigger yields in each kinematic region, multiplicity and momentum bin.

Mult. and p_{T} bin	Near-side (jet)	Away-side (jet)	UE
0-20%, low	4.46e+00	4.75e+00	3.51e+00
20-50%, low	3.75e+00	3.63e+00	3.50e+00
50-80%, low	4.94e+00	6.35e+00	3.67e+00
0-20%, high	3.80e+00	4.00e+00	3.51e+00
20-50%, high	3.61e+00	3.63e+00	3.51e+00
50-80%, high	4.17e+00	5.16e+00	3.81e+00

Table 4.9: Final multiplicity-uncorrelated systematic errors (in %) for the per-trigger h-Λ yields in each kinematic region, multiplicity and momentum bin, used for calculating errors associated with quantities describing trends versus multiplicity (slopes and percent changes).

Mult. and p_{T} bin	Near-side (jet)	Away-side (jet)	UE
0-20%, low	2.73e+00	2.83e+00	6.66e-01
20-50%, low	3.09e+00	3.57e+00	1.00e+00
50-80%, low	5.80e+00	6.95e+00	2.23e+00
0-20%, high	2.91e+00	3.65e+00	7.40e-01
20-50%, high	4.32e+00	5.41e+00	1.28e+00
50-80%, high	4.47e+00	5.45e+00	2.35e+00

Table 4.10: Final multiplicity-uncorrelated systematic errors (in %) for the h-h per-trigger yields in each kinematic region, multiplicity and momentum bin, used for calculated errors associated with quantities describing trends versus multiplicity (slopes and percent changes).

Mult. and p_{T} bin	Near-side (jet)	Away-side (jet)	UE
0-20%, low	1.72e+00	2.31e+00	1.86e-01
20-50%, low	1.31e+00	1.92e+00	2.29e-01
50-80%, low	3.95e+00	6.23e+00	1.21e+00
0-20%, high	1.03e+00	1.68e+00	2.42e-01
20-50%, high	7.24e-01	1.22e+00	2.76e-01
50-80%, high	2.28e+00	4.08e+00	1.54e+00

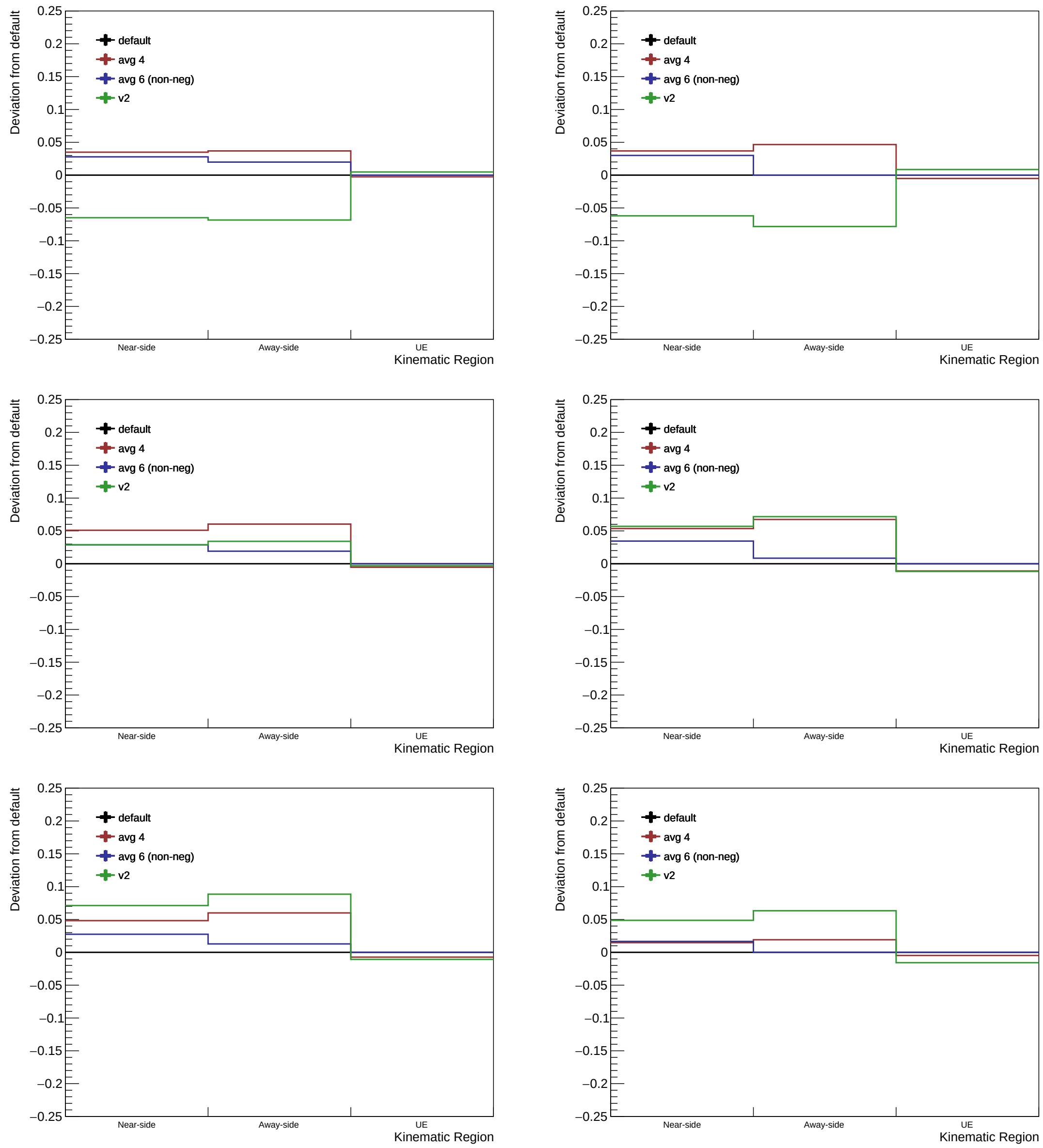

Figure 4.19: The deviation from the nominal h-Λ per-trigger yields for each yield extraction procedure variation (post Barlow check) in each kinematic region for the 0-20% (top), 20-50% (middle) and 50-80% (bottom) multiplicity bins in the lower (left) and higher (right) associated p_{T} bins. The systematic uncertainty for the yield extraction procedure is calculated by taking the RMS of these deviations for each kinematic region.

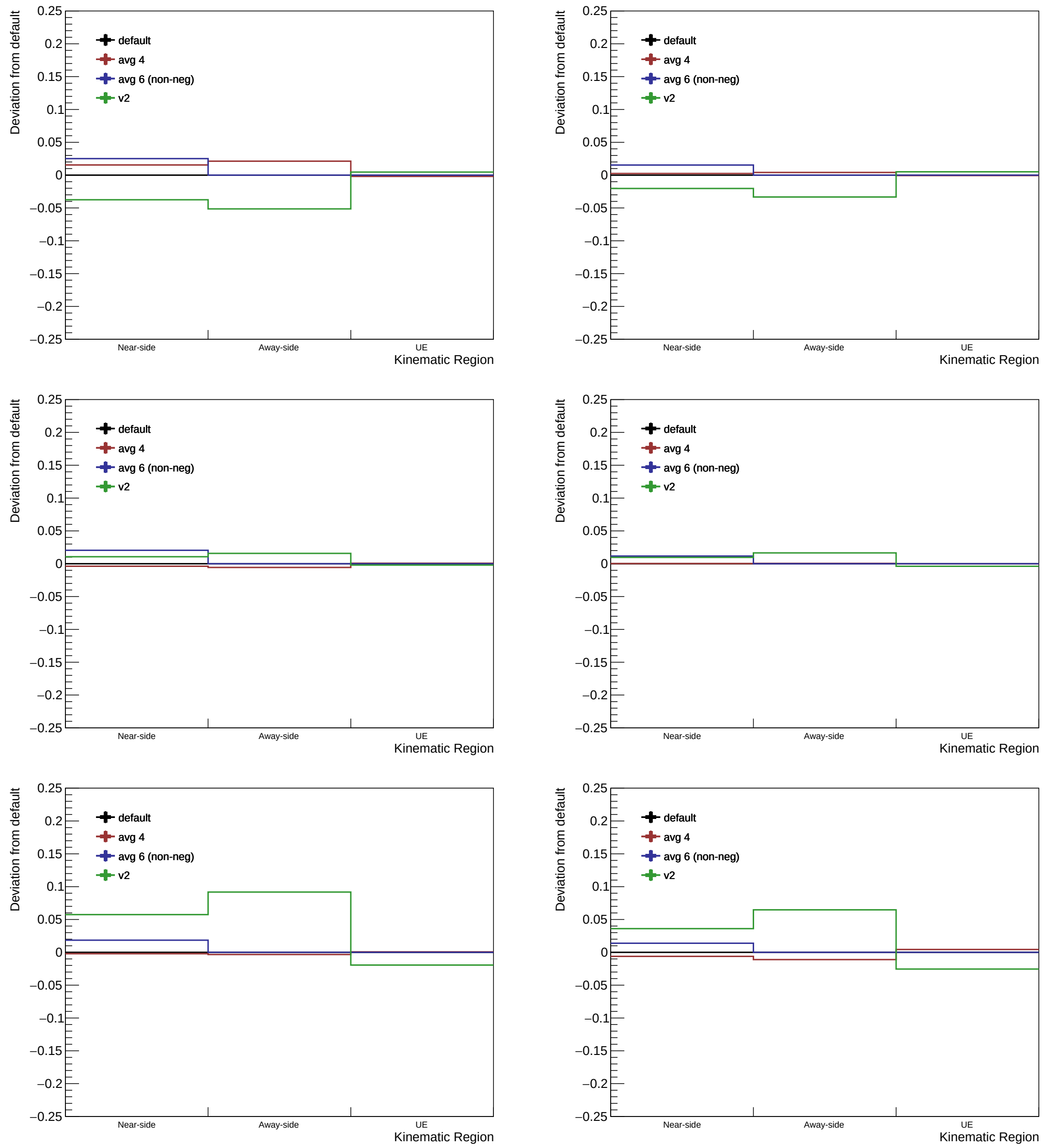

Figure 4.20: The deviation from the nominal h-h per-trigger yields for each yield extraction procedure variation (post Barlow check) in each kinematic region for the 0-20% (top), 20-50% (middle) and 50-80% (bottom) multiplicity bins in the lower (left) and higher (right) associated p_{T} bins. The systematic uncertainty for the yield extraction procedure is calculated by taking the RMS of these deviations for each kinematic region.

4.1.3 Near- and away-side width extraction

The extracted widths of the near- and away-side jet components from the $\Delta\varphi$ distributions are also subject to a fair amount of systematic uncertainty, both from the variations of the $\Delta\varphi$ distributions themselves as well as the techniques used to extract said widths. None of the $\Delta\varphi$ distributions variations are "new", in that they have been discussed in some way within the previous sections. However, the effects of these variations on the extracted widths are not as straightforward as the effects on the yields, and thus deserve their own section. Furthermore, the fitting techniques used to extract the widths are different enough than the fitting techniques for yield extraction (Sections 4.1.2.4 and 4.1.2.5),that they will be discussed separately.

As a brief reminder, the nominal procedure for extracting the jet widths is by fitting the $\Delta\varphi$ distribution to the von Mises-based fit function,

$$f(\Delta\varphi) = U(\Delta\varphi) + \frac{A_{\mathrm{NS}}}{2\pi I_0(k_{\mathrm{NS}})} e^{k_{\mathrm{NS}} cos(\Delta\varphi - \mu_{\mathrm{NS}})} + \frac{A_{\mathrm{AS}}}{2\pi I_0(k_{\mathrm{AS}})} e^{k_{\mathrm{AS}} cos(\Delta\varphi - \mu_{\mathrm{AS}})}, \tag{4.16}$$

where A and μ are the amplitudes and means of the von Mises components, and k is a measure of the collimation of the distribution, which is inversely related to the width through

$$\sigma = \sqrt{-2\ln\frac{I_1(\kappa)}{I_0(\kappa)}}. \tag{4.17}$$

In these equations, I_n refers to the modified Bessel function of the nth kind. During the fitting procedure, the means μ_{NS} and μ_{AS} are again fixed to 0 and π, respectively, and the $U(\Delta\varphi)$ term is fixed to the function obtained by fitting the UE which includes a non-zero v_2 contribution, as described in Section 4.1.2.2.

The reason for fixing the U component during fitting is subtle, as the von Mises distributions describe the data extremely well and generally allow for the variation of this component while still obtaining a convergent fit. However, the form of the Von Mises function,

$$f(x) = e^{kcos(x)}, \tag{4.18}$$

presents a unique issue: if the width is sufficienctly large, meaining k is sufficiently small (≈ 1), there is an "offset" from the U term that never tapers off. This is fundamentally different than a Gaussian, which will always converge to zero (or U in this case) at large enough x. A visual depiction of this effect can be seen in Figure 4.21. In most cases, this never presents an issue as the widths are usually such that $k > 2$. However, in the lowest momentum bin for the more central h-Λ $\Delta\varphi$ distributions, allowing the U term to vary during the fitting procedure has a very large effect on the corresponding k value, as the fitting software tries to "absorb" this offset into U. Because of this, the U term is fixed during all fitting procedures, and instead the techniques for determining U are varied.

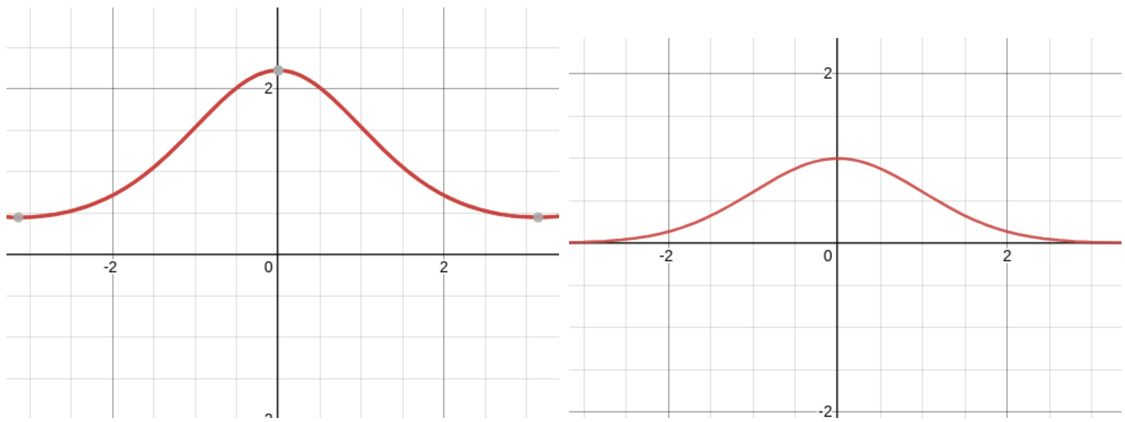

Figure 4.21: The Von Mises (left) and Gaussian (right) dist with $\kappa = 1$ and $\sigma = 1$. Note that the von Mises distribution does not approach zero at large x, while the Gaussian does.

4.1.3.1 Signal, sideband and PID cut variations

Each of the signal, sideband and PID cut variations that affect the $\Delta\varphi$ distributions (from Section 4.1.1) can also affect the corresponding extracted widths. To that end, the h-Λ $\Delta\varphi$ von Mises-based fits and extracted widths for each of these variations for all multiplicity and momentum bins can be seen in Figure 4.23. Note that these widths were extracted using the nominal procedure described at the beginning of this section. Deviations from the nominal near-side widths never exceed 3.5% in most cases, whereas the away-side width deviations are much larger, with some variations resulting in over a 10% change from the nominal value, even after removing statistically insignificant variations via the Barlow procedure in Section 4.1.3.3.

Again, problematic behavior arises from the PID cut variation which requires of a TOF hit for both of the Λ daughters, with both the near- and away-side widths being particularly sensitive to this cut. As the lower momentum daughter pions are usually deflected by the detector's magnetic field before reaching the TOF, in cases when the

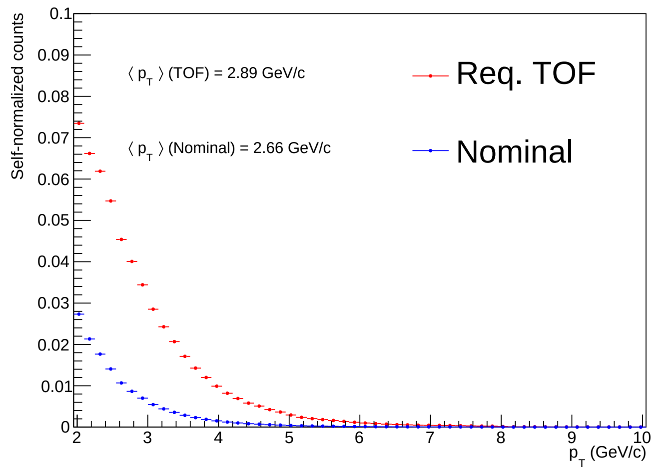

Figure 4.22: The p_{T} distributions of Λ candidates with and without the TOF signal requirement. The mean p_{T} of the Λ candidates with daughters that generate a TOF signal is nearly 10% higher than those without this requirement, which indicates that the requiring a TOF signal for the Λ daughters introduces a physical bias.

pion actually generates a TOF signal, its corresponding momentum is likely higher than usual. This would result in a higher-than-usual Λ momentum, which in turn would give lower-than-usual jet widths in the corresponding h-Λ correlations as jets become less collimated as their constituent momentum decreases. To test this, the p_{T} distributions of Λ candidates with and without the TOF signal are compared in Figure 4.22. The mean p_{T} of the Λ candidates with daughters that generate a TOF signal is around 10% higher than those without this requirement, which indicates that the TOF signal requirement introduces a physical bias into the h-Λ $\Delta\varphi$ distributions, manifesting as unusually low jet widths. Luckily, this requirement also happens to reduce the overall yield of Λ candidates by huge margin, causing a large amount of statistical fluctuations in the corresponding h-Λ correlation distributions. Because of this, the TOF signal requirement ends up being excluded after the Barlow check. However, it is important to distinguish between excluding variations because they are statistically insignificant and excluding them because they introduce *physical* biases into the data. Had the data sample been larger, the TOF signal requirement would have likely survived the Barlow check, leaving no choice but to rely on the aforementioned argument.

4.1.3.2 Fitting procedure variations

Both of the fitting functions discussed in this thesis are of the form

$$f(\Delta\varphi) = U(\Delta\varphi) + f_{\mathrm{NS}}(\Delta\varphi) + f_{\mathrm{AS}}(\Delta\varphi), \tag{4.19}$$

where U is the underlying event function, and f_{NS} (f_{AS}) is the distribution that describes the near-side (away-side) jet. To estimate the systematic uncertainty associated with the fitting procedure, the following variations are considered:

1. **Varying $U(\Delta\varphi)$:** The $U(\Delta\varphi)$ term is varied by replacing the nominal v_2-based UE function with a flat line equal to the average of the $\Delta\varphi$ distribution in the ranges $[-\frac{\pi}{2}, -\frac{\pi}{4}) \cup [\frac{\pi}{4}, \frac{5\pi}{8}) \cup [\frac{11\pi}{8}, \frac{3\pi}{2})$ and $[-\frac{\pi}{2}, -\frac{3\pi}{8}) \cup [\frac{3\pi}{8}, \frac{5\pi}{8}) \cup [\frac{11\pi}{8}, \frac{3\pi}{2})$ (i.e. the nominal and restricted-range UE variations from the yield extraction procedure)

2. **Varying the f_{NS} and f_{AS} functions:** The f_{NS} and f_{AS} functions are varied by replacing the nominal von Mises distributions with the Gaussian ones, as described in Section 4.1.2.4, and the U term is fixed to the average of the $\Delta\varphi$ distribution in the ranges $[-\frac{\pi}{2}, -\frac{\pi}{4}) \cup [\frac{\pi}{4}, \frac{5\pi}{8}) \cup [\frac{11\pi}{8}, \frac{3\pi}{2})$ (again, the nominal UE determination technique from the yield extraction procedure)

More variations were initially considered–namely using the v_2-based UE with the Gaussian functions from (2) and even trying generalized Gaussians **GeneralizedGaus** to describe the jet components–but they were discarded as many of the fits did not converge for all multiplicity and momentum ranges[3] despite a large amount of effort.

The choice of making the v_2-based UE determination procedure the nominal one was not made lightly, as it breaks the symmetry with the nominal yield extraction technique. In the presence of non-zero elliptic flow (as is likely the case at higher multiplicities), the v_2-based UE determination procedure is the most physically motivated, as it is the only one that takes into account the underlying event's azimuthal anisotropy. The only reason this procedure was not chosen as the nominal technique for yield extraction is extremely specific to this analysis: at the time of writing this thesis, the only available h-$\phi(1020)$ correlation results in p–Pb at $\sqrt{s_{\mathrm{NN}}} = 5.02$ TeV come in the form of the h-ϕ/h-h per-trigger yield ratios, where the yields are extracted assuming a flat UE. As mentioned in Section **??**, one of the topics of this analysis

[3] This is a strict requirement, there are twelve fits in total, each with at least four free parameters, and the fitting software is not particularly robust.

involves investigating open versus hidden strangeness in the form of the h-Λ/h-ϕ per-trigger yield ratios in the different kinematic regions. This is done by taking a ratio of ratios, namely

$$\frac{(\text{h-}\Lambda)}{(\text{h-h})_1} / \frac{(\text{h-}\phi)}{(\text{h-h})_2} \tag{4.20}$$

where the subscripts 1 and 2 are used to differentiate between this research and the ϕ analysis, respectively. This only reduces to the h-Λ/h-ϕ ratios if two conditions are met: the first is that the h-h distributions are the same (which is investigated more thoroughly in Section 4.2.3), and the second is that the yields are extracted from these dihadron distributions using the exact same procedure. While this is not required in the case of the h-Λ yields, the same procedure is applied for the sake of consistency.

The resulting fits and extracted widths for each of the variations listed above in all multiplicity and momentum ranges for both the h-Λ and h-h cases can be seen in Figure 4.24. Again, only small deviations from the central values are observed in the near-side widths across all variations, with the largest percent difference being around 3% across all multiplicity and momentum bins for both the h-Λ and h-h distributions. Interestingly, the away-side widths appear to be much more sensitive to the inclusion of v_2, as all variations from the nominal technique–again, each variation assumes a flat UE–result in widths which are systematically lower than the central values by around 5-10%. This is a strange result, as the v_2-based UE is completely symmetric about $\Delta\varphi = \pi/2$, and thus should affect the near-side widths in the same way as the away-side. As mentioned above, including v_2 in the UE is the more *physically* motivated choice, and therefore is chosed to be nominal despite these large deviations. Note that the Gaussian and von Mises widths are more similar in the cases where the flat UE is used, indicating that the observed deviations are not due to the choice of fitting function.

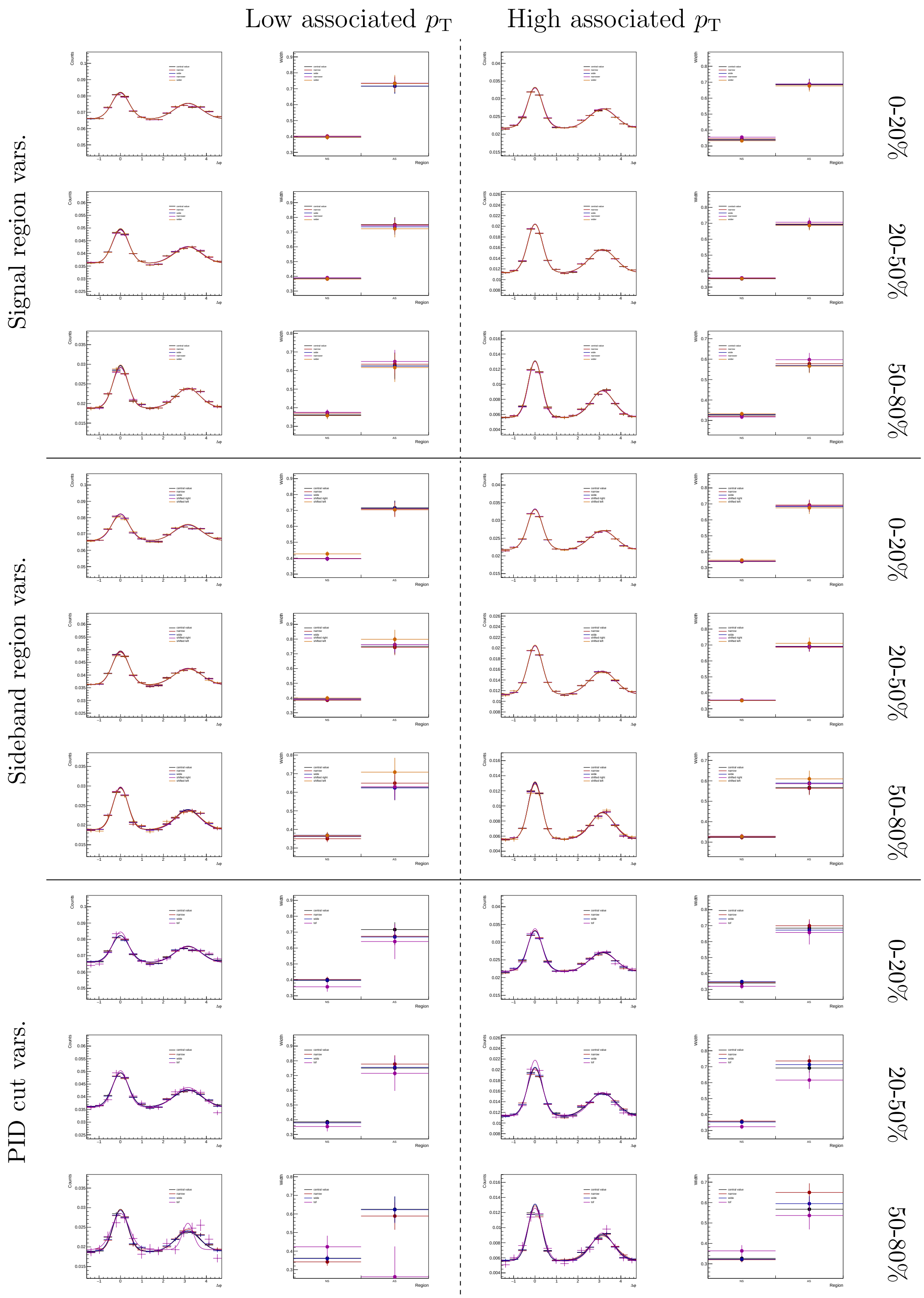

Figure 4.23: The resulting von Mises fits and extracted jet widths after the signal, sideband and PID cut variations are applied to the h-Λ $\Delta\varphi$ distributions.

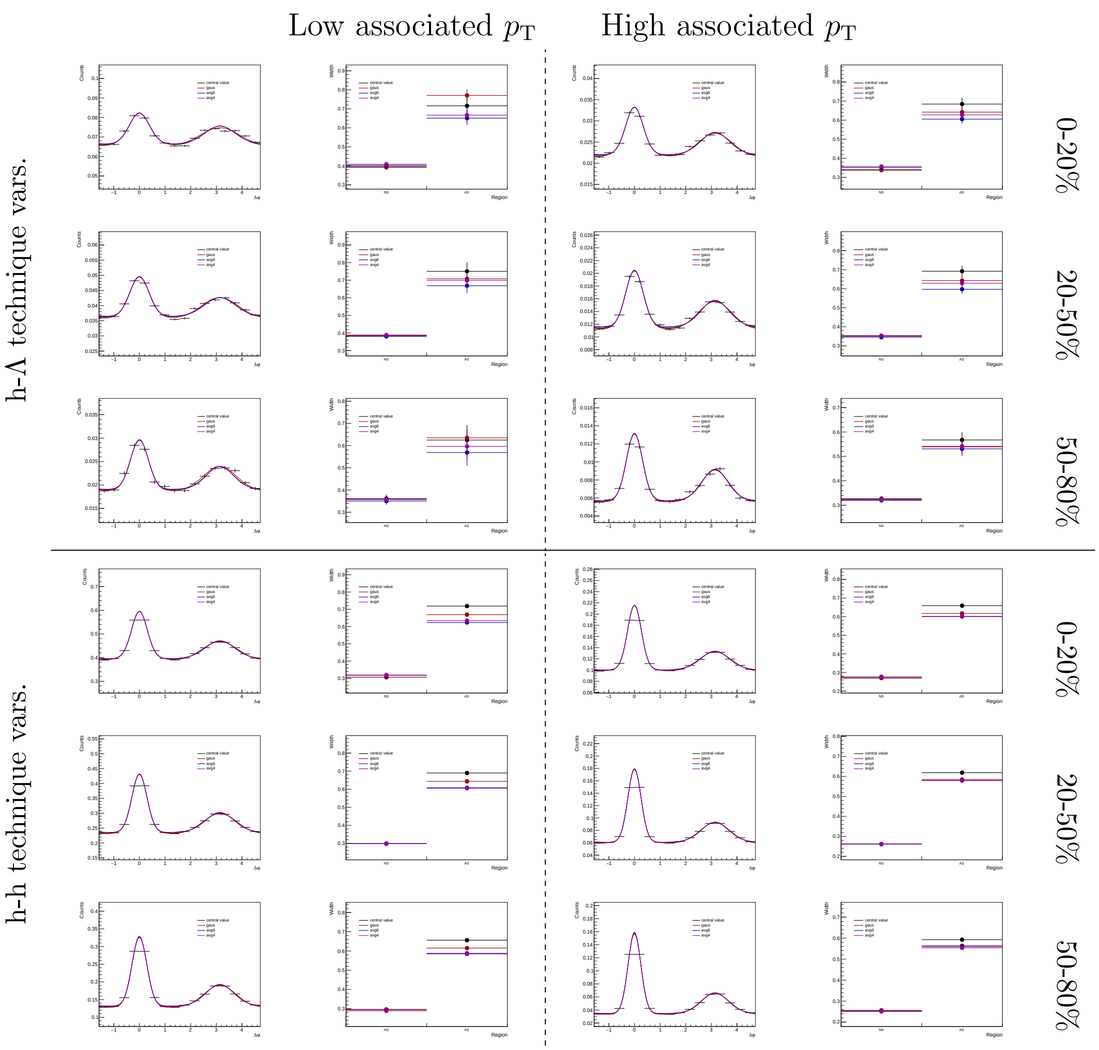

Figure 4.24: The resulting h-Λ (top) and h-h (bottom) von Mises fits and extracted jet widths in each multiplicity and momentum bin after each variation of the fitting procedure.

4.1.3.3 Barlow check for width extraction

Again, following the same techniques as outlined in Sections 4.1.1.4 and 4.1.2.6, a Barlow check is performed for the variations presented in this section that affect the extracted near- and away-side widths. As was before, if the majority of the extracted h-Λ widths for a given variation have $|N\sigma_{RB}| < 1$, that variation is excluded from the systematic uncertainty calculation. This majority is calculated using both the near- and away-side jet components across all multiplicity bins and associated momentum bins. Again, the dihadron widths are not considered for this procedure[4], and any fitting technique variation that is excluded from the uncertainty calculation as the result of this check for the h-Λ widths will also be excluded for the h-h case. Visual depictions of the Barlow procedure can be seen in Figure **??**.

As a result of the check, the following variations were excluded from the systematic uncertainty calculation for the jet widths:

- Signal: Wide, Wider
- Sideband: Wide, Narrow
- PID: Require TOF

Curiously, these are the same variations that were excluded for the $\Delta\varphi$ distributions, which is *mostly*[5] a coincidence.

4.1.3.4 Width extraction systematics, summarized

The systematic uncertainties associated with the h-Λ and h-h jet width extraction for each multiplicity and associated momentum bin can be seen in Tables **??** (h-Λ) and **??** (h-h), with visual depictions shown in Figures 4.26 (h-Λ) and 4.27. The total systematic uncertainties are obtained by adding the individual uncertainties in quadrature. Note that the away-side width uncertainties are much larger than the near-side, indicating that constraining the away-side jet width is a much more difficult procedure,

[4] Due to extremely small statistical errors, see Section 4.1.2.6

[5] There is obviously some correlation between variations in the individual $\Delta\varphi$ bins and the widths. Consider a hypothetical variation that causes an unusually large spike in a $\Delta\varphi$ bin near zero: this would certainly cause the near-side width to be considerably smaller than normal. This is an extreme example, however, and generally these variations affect the individual $\Delta\varphi$ bins in similar ways.

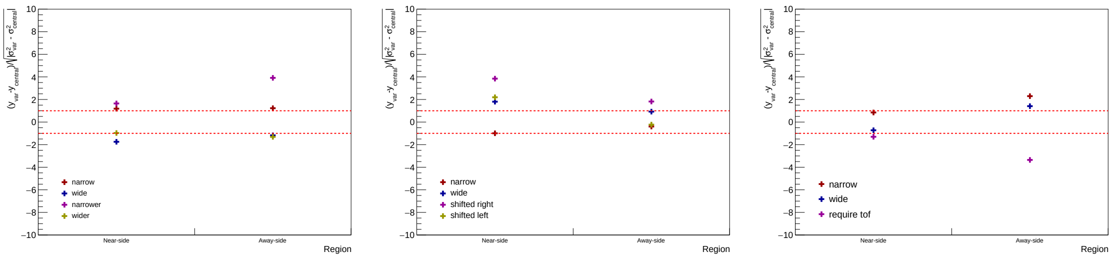

Figure 4.25: Barlow check for the width extraction procedure for the signal (left), sideband (middle), and PID (right) variations in the 20-50% multiplicity bin. The red lines represent $N\sigma_{RB} = \pm 1$, and if the majority of the points fall within the red lines (across all p_{T} and multiplicity bins), they are excluded from the width systematic uncertainty calculation.

especially in the presence of non-zero elliptic flow (as discussed in Section 4.1.3.2). As the width uncertainties do not exhibit any significant multiplicity dependence, the multiplicity-uncorrelated portion of these uncertainties is not reported.

Both the topological selection and associated hadron efficiency uncertainties are given in the tables and figures, which were obtained by randomly varying the $\Delta\varphi$ distributions within their respective systematic uncertainties (Table 4.1) and extracting the widths using the nominal procedure. As the topological selection and tracking efficiency uncertainties were not directly calculated in this analysis, these results serve as a "best guess" for how the widths would be affected by variations in the corresponding selection criteria. The results of this procedure for the h-Λ and h-h distributions in the 20-50% multiplicity bin for both associated momentum ranges can be seen in Figure 4.28.

Mult.	p_{T}	Peak	Signal	Sideband	PID	Fit proc.	Topo.	Total
0-20%	low	NS	1.19	5.41	1.19	2.09	3.40	6.93
20-50%	low	NS	1.13	2.70	1.74	0.93	3.40	4.90
50-80%	low	NS	3.20	1.19	3.82	2.05	3.40	6.48
0-20%	low	AS	2.53	1.64	6.21	7.91	2.40	10.77
20-50%	low	AS	0.57	4.68	2.62	8.16	2.40	10.07
50-80%	low	AS	2.88	9.43	4.11	5.88	2.40	12.43
0-20%	high	NS	3.44	1.66	2.19	3.51	3.10	6.43
20-50%	high	NS	1.10	0.48	1.09	1.35	3.10	3.75
50-80%	high	NS	2.46	0.56	1.68	1.54	3.10	4.60
0-20%	high	AS	0.51	1.00	1.99	8.95	6.10	11.07
20-50%	high	AS	1.56	1.93	5.02	10.33	6.10	13.24
50-80%	high	AS	3.93	5.74	10.80	5.40	6.10	15.21

Table 4.11: The final systematic errors from the h-Λ $\Delta\varphi$ near-side (NS) and away-side (AS) width extraction for each multiplicity bin in the lower (top) and higher (bottom) associated p_{T} bins. The total systematic error is calculated by adding each systematic error in quadrature.

Mult.	p_{T}	Peak	Fit proc.	Trk. eff.	Total
0-20%	low	NS	2.21	1.00	2.42
20-50%	low	NS	0.21	1.00	1.02
50-80%	low	NS	1.74	1.00	2.01
0-20%	low	AS	8.75	1.50	8.87
20-50%	low	AS	6.66	1.50	6.82
50-80%	low	AS	6.91	1.50	7.07
0-20%	high	NS	1.86	1.00	2.11
20-50%	high	NS	0.12	1.00	1.01
50-80%	high	NS	1.47	1.00	1.78
0-20%	high	AS	8.02	1.50	8.16
20-50%	high	AS	6.06	1.50	6.24
50-80%	high	AS	5.73	1.50	5.93

Table 4.12: The final systematic errors from the h-h $\Delta\varphi$ near-side (NS) and away-side (AS) width extraction for each multiplicity bin in the lower (top) and higher (bottom) associated p_{T} bins. The total systematic error is calculated by adding each systematic error in quadrature.

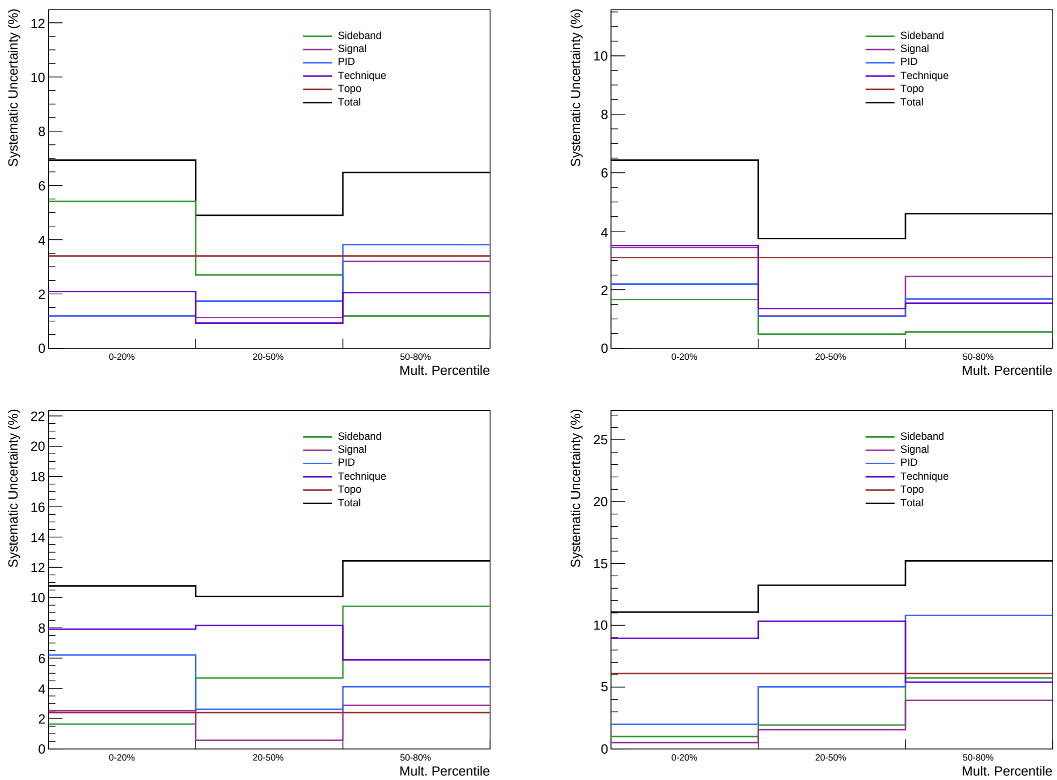

Figure 4.26: Final systematic errors for the h-Λ $\Delta\varphi$ near-side (top) and away-side (bottom) width extraction for each multiplicity bin in the lower (left) and higher (right) associated p_{T} bins.

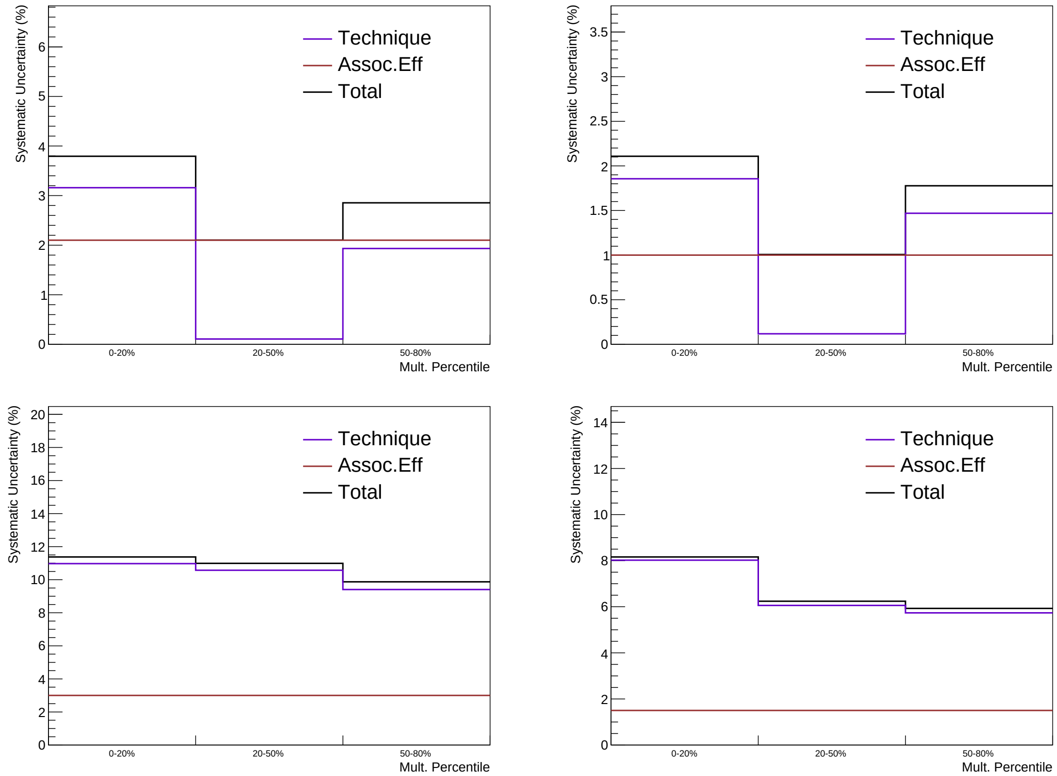

Figure 4.27: Final systematic errors for the h-h $\Delta\varphi$ near-side (top) and away-side (bottom) width extraction for each multiplicity bin in the lower (left) and higher (right) associated p_{T} bins.

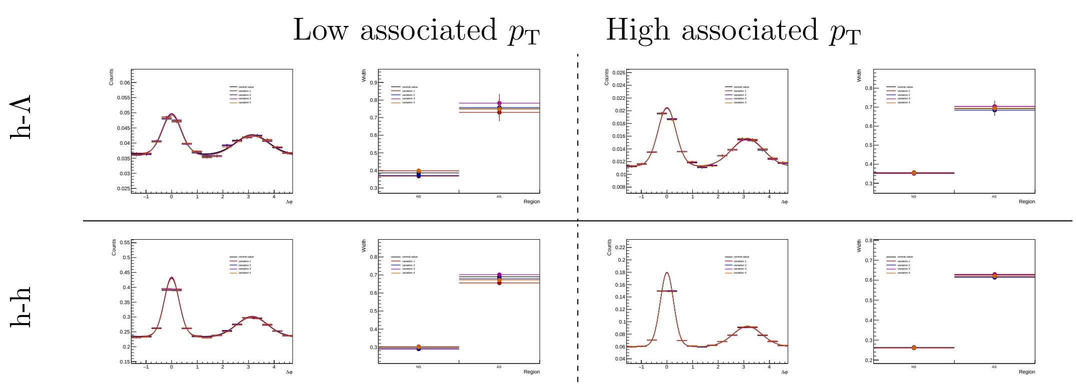

Figure 4.28: The resulting h-Λ (top) and h-h (bottom) von Mises fits and extracted jet widths in the 20-50% multiplicity bin for each momentum bin after random variations of the individual $\Delta\varphi$ bins within the topological selection (h-Λ) and tracking efficiency (h-h) uncertainties from Table 4.1.

4.1.4 Final systematics tables

For ease of reference, all of the final systematic uncertainties discussed in the previous sections have been consolidated into Tables 4.13 (h-Λ) and 4.14 (h-h).

Table 4.13: The final systematic uncertainties for the h-Λ $\Delta\varphi$ distributions, the per-trigger jet and UE yields, and the jet widths in all multiplicity and associated momentum bins. The fraction of the systematic uncertainty which is uncorrelated with multiplicity is reported separately in parentheses for the extracted yields. The low (high) momentum bin is such that $1.5 < p_T^{\text{assoc.}} < 2.5$ GeV/c ($2.5 < p_T^{\text{assoc.}} < 4.0$ GeV/c).

Mult. and p_{T} bin	$\Delta\varphi$ dist.	Y_{near}	Y_{away}	Y_{UE}	σ_{NS}	σ_{away}
0-20%, low	3.3%	5.5(2.7)%	5.6(2.8)%	3.1(0.7)%	6.9%	10.8%
20-50%, low	3.4%	4.9(3.1)%	5.2(3.6)%	3.2(1.0)%	4.9%	10.1%
50-80%, low	3.8%	6.3(5.8)%	7.2(7.0)%	3.7(2.2)%	6.5%	12.4%
0-20%, high	3.2%	5.5(2.9)%	6.1(3.7)%	3.2(0.7)%	6.4%	11.1%
20-50%, high	3.3%	5.9(4.3)%	6.5(5.4)%	3.3(1.3)%	3.8%	13.2%
50-80%, high	4.1%	4.8(4.5)%	5.3(5.5)%	3.7(2.4)%	4.6%	15.2%

Table 4.14: The final systematic uncertainties for the h-h $\Delta\varphi$ distributions, the per-trigger jet and UE yields, and the jet widths in all multiplicity and associated momentum bins. The fraction of the systematic uncertainty which is uncorrelated with multiplicity is reported separately in parentheses for the extracted yields. The low (high) momentum bin is such that $1.5 < p_T^{\text{assoc.}} < 2.5$ GeV/c ($2.5 < p_T^{\text{assoc.}} < 4.0$ GeV/c).

Mult. and p_{T} bin	$\Delta\varphi$ dist.	Y_{near}	Y_{away}	Y_{UE}	σ_{NS}	σ_{away}
0-20%, low	3.5%	4.5(1.7)%	4.8(2.3)%	3.5(0.2)%	2.4%	8.9%
20-50%, low	3.5%	3.8(1.3)%	3.6(1.9)%	3.5(0.2)%	1.0%	6.8%
50-80%, low	3.5%	4.9(3.9)%	6.4(6.2)%	3.7(1.2)%	2.0%	7.1%
0-20%, high	3.5%	3.8(1.0)%	4.0(1.7)%	3.5(0.2)%	2.1%	8.2%
20-50%, high	3.5%	3.6(0.7)%	3.6(1.2)%	3.5(0.3)%	1.0%	6.2%
50-80%, high	3.5%	4.2(2.3)%	5.2(4.1)%	3.8(1.5)%	1.8%	5.9%

4.2 Cross-checks

As mentioned in the introduction to this chapter, this section presents a number of cross-checks that were performed to verify the validity and robustness of the analysis procedure.

4.2.1 Monte Carlo closure tests

One of the most common procedures for verifying the validity of an experimental analysis comes in the form of a **Monte Carlo closure test MCClosure**. The basic steps of any MC closure test are as follows:

1. Generate a large sample of simulated events using a Monte Carlo generator, which models both the physics of the collision and the detector response

2. Apply the same analysis method and selection criteria to the detector-simulated events as to the experimental data to obtain a **reconstructed** observable

3. Compare the reconstructed observable with the **ground-truth** observable, which is obtained directly from the generator-level particles

Generally the third step is done by taking a ratio of the reconstructed observable to the ground-truth observable, which should be consistent with unity if the analysis procedure is valid. Significant deviations from unity would indicate that the experimental procedure introduces a non-physical bias to the measurement, which should be addressed.

For the Monte Carlo closure tests presented in this section, the p–Pb collision events are simulated using the DPMJet generator **DPMJet**, with the ALICE detector response to the simulated particles handled by the GEANT [12] software package. The reconstructed h-Λ and h-h 2D correlation distributions are generated using the same procedure as described in 3. In particular, this means that:

- Both the reconstructed trigger and associated Λ (h) pass the track cuts described in Tables 3.2 and 3.5 (3.3), respectively

- To avoid issues with PID using GEANT[6], the Λ daughter tracks are verified to be from a proton/pion by checking their corresponding generator-level particles
- The efficiency and acceptance corrections are applied to the h-h and h-Λ distributions in the same was as described in Section 3.5
- The additional corrections (sideband subtraction, signal scaling, two-track template) are applied to the h-Λ distributions as they are in Section 3.5.3

For the ground-truth distributions, the trigger and associated Λ (h) are taken directly from the generator-level particles. The same kinematic cuts are also applied, namely the trigger is required to have momentum $4.0 < p_{\mathrm{T}} < 8.0$ GeV/c, the associated Λ (h) have the same momentum ranges as the reconstructed case, and all particles are required to fall within $|\eta| < 0.8$. Applying these pseudorapidity cuts on the trigger and associated particles ensures that the underlying physics[7] is the same as the reconstructed case. Unfortunately this requirement also introduces the same triangular shape along $\Delta\eta$ in the correlation distributions as seen in data, which is corrected for using the mixed-event technique described in Section 3.5.

Both the reconstructed and ground-truth 2D correlation distributions are projected onto $\Delta\varphi$ in the range $|\Delta\eta| < 1.2$, and the results for the h-Λ and h-h $\Delta\varphi$ distributions are shown for each associated p_{T} bin in Figures 4.29 (h-Λ) and 4.30 (h-h), along with the corresponding (reconstructed)/(ground-truth) distribution ratios. A fit to the ratio is also shown, which is consistent with unity in all cases. This indicates that the analysis procedure is valid, and that the corrections applied to the h-Λ and h-h distributions are not introducing any non-physical biases to the $\Delta\varphi$ distribution measurements. As all of the observables are derived directly from these distributions, it is safe to assume the reconstructed and ground-truth versions of these observables are also consistent with each other.

While the MC closure tests provide a general framework for checking the validity of an experimental analysis, there are a few more specific checks that are performed to ensure the robustness of this analysis, which are described in the following sections.

[6]The $n\sigma_{\mathrm{TPC,TOF}}$ values predicted by GEANT differ from experimental data by a large margin, so using GEANT for PID is generally avoided whenever possible

[7]Particle production is rapidity-dependent, so choosing particles in a different rapidity range could alter the spectrum.

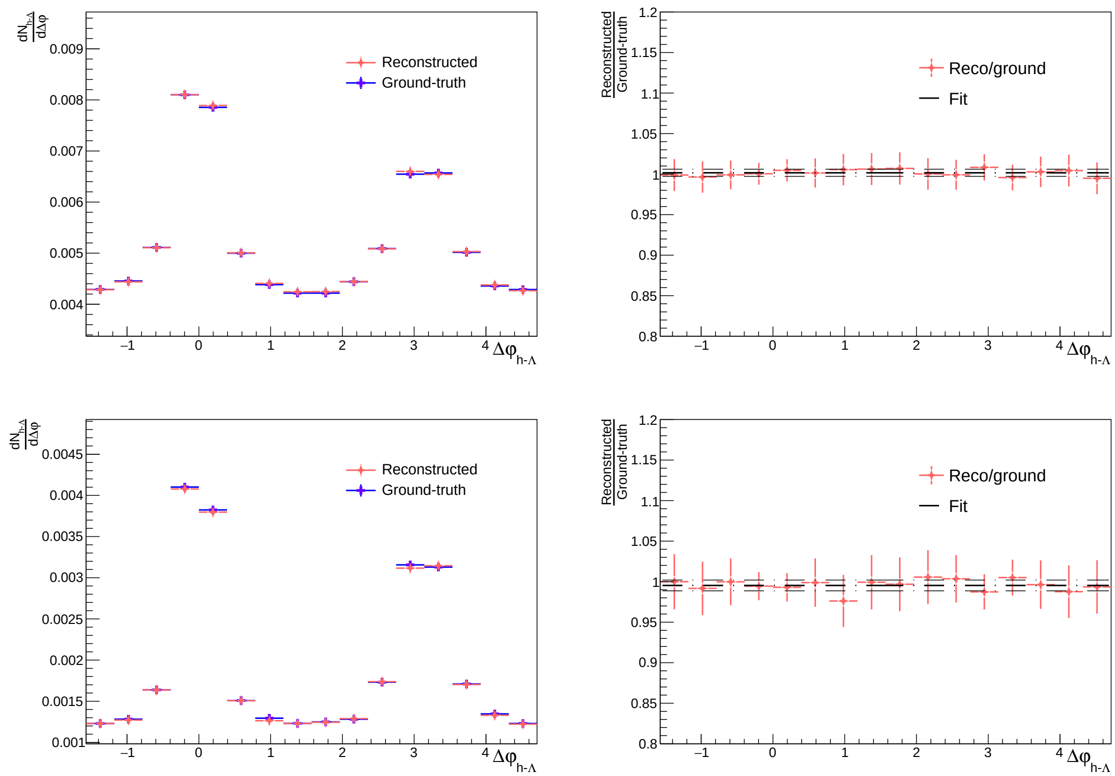

Figure 4.29: The reconstructed (pink) and ground-truth (blue) h-Λ $\Delta\varphi$ distributions in the lower (top) and higher (bottom) associated p_{T} bins, along with a (reconstructed)/(ground-truth) ratio and straight-line fit with errors shown as dashed lines. The ratio is consistent with unity, and thus the corrections applied to the h-Λ distributions are valid.

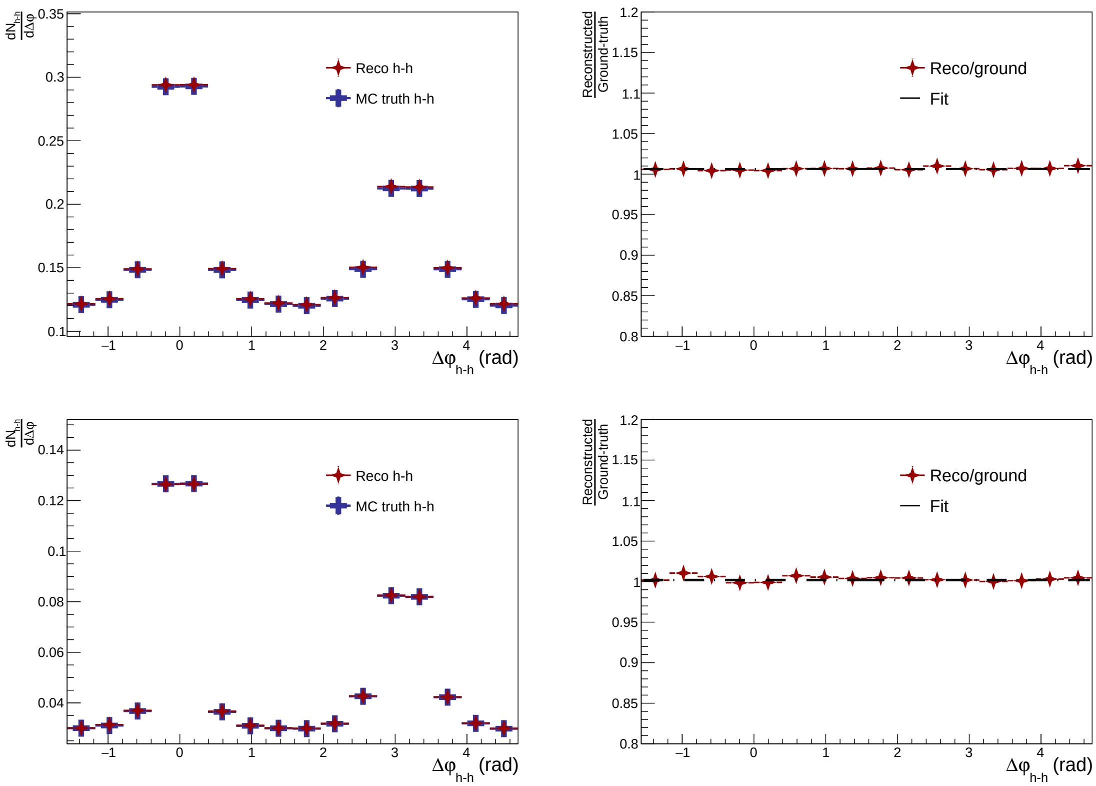

Figure 4.30: The reconstructed (pink) and ground-truth (blue) h-h $\Delta\varphi$ distributions in the lower (top) and higher (bottom) associated p_T bins, along with a (reconstructed)/(ground-truth) ratio and straight-line fit with errors shown as dashed lines. Again, the ratio is consistent with unity, and thus the corrections applied to the h-h distributions are valid.

4.2.2 Correlations with a single trigger

A central feature of this analysis relies on the assumption that the per-trigger pair-wise yields from the h-Λ or h-h distributions are roughly equal to the per-trigger associated yields for Λ baryons or charged hadrons in events that have a trigger hadron, so that the (h-Λ)/(h-h) yield results can be interpreted as the Λ/h ratio in each region. This is only true if there is only a single trigger hadron in each event, which is obviously not the case across a large event sample. To see why this is required, consider two events: the first has a single trigger with three associated particles, while the second has two triggers with three associated particles. In the first event, there are three trigger-associated pairs, which corresponds exactly to the number of associated particles in the event. In the second, there are twice as many pairs as there are associated particles, meaning that the pair-wise yield "double counts" the associated particles. A diagram of this effect is shown in Figure 4.31. This effect scales with the number of triggers: if there are N triggers in an event, there would be N times as many pairs as associated particles. This diagram also introduces another subtle effect of multiple triggers: if triggers t_1 and t_2 belong to separate jets within a single event, then the associated particles that fall into the jet-like regions when correlated with t_1 could be mistankingly placed in the "underlying event" when correlated with t_2, artificially inflating the UE yields.

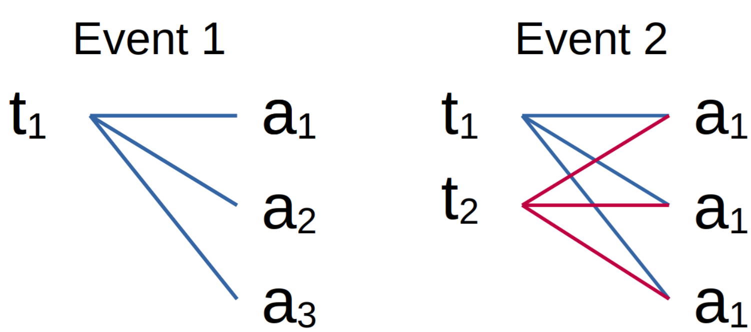

Figure 4.31: A diagram showing the effect of multiple triggers on the per-trigger pair-wise yield. In the first event, there is a single trigger with three associated particles, so the pair-wise yield is equal to the number of associated particles. In the second event, there are two triggers with three associated particles, so the pair-wise yield is twice the number of associated particles.

Luckily, less than 1% of all events have more than a single trigger, as shown in Figure 4.32. Even still, the effect of multiple triggers on the per-trigger pair-wise yield is investigated by repeating the same analysis procedure as described in the previous chapter, with one change:

- If an event has more than one trigger, only the trigger with the highest momentum within the $4.0 < p_{\mathrm{T}} < 8.0$ GeV/c range is used

This guarantees that no associated yields will be counted more than once, at the expense of a slightly modified trigger p_{T} spectrum[8]. The final single trigger h-Λ and h-h $\Delta\varphi$ distributions for each multiplicity bin are compared with the original method (all trigger) distributions in Figure 4.33. A flat deviation of around 5% is observed for both the h-Λ and h-h cases, which is consistent across all multiplicity bins.

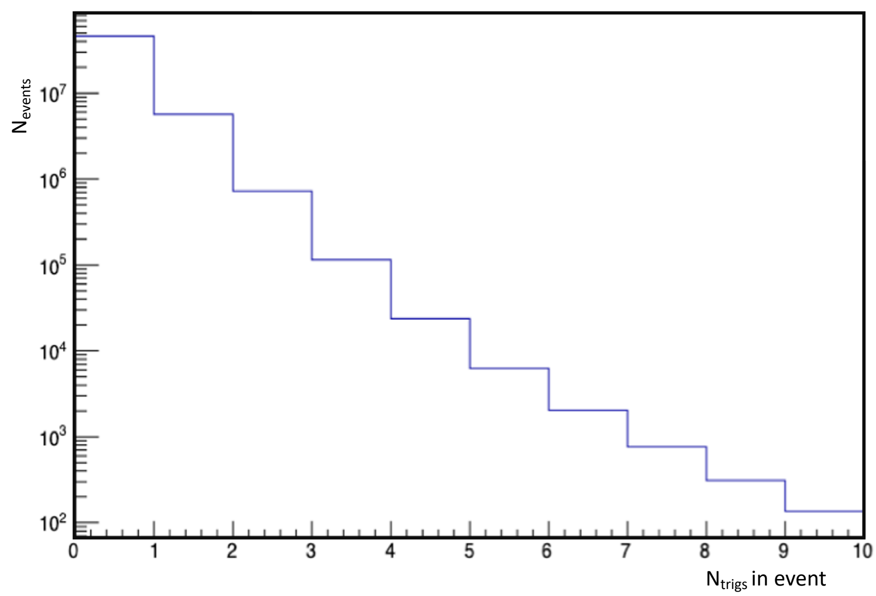

Figure 4.32: A log-plot showing the number of triggers per event across the entire data sample. Only a small fraction of events have at least a single trigger, and of those events, only a small fraction have more than one trigger.

[8]Selecting the highest p_{T} trigger in the 4-8 GeV/c range usually still amounts to selecting a ≈ 4 GeV/c particle.

As the (single trigger)/(all trigger) distribution ratios are mostly flat for both the h-Λ and h-h distributions across all multiplicty bins, the effect on the final yield measurements would only be a $\approx 5\%$ change of scale along the y-axis, and the ratio measurements would remain unchanged. Furthermore, this scale factor is the same across all multiplicity bins, indicating that using the standard per-trigger correlation method accurately captures the multiplicity-dependent behaviour of the Λ/h ratios in events with a trigger. Because the conclusions drawn from the results of this thesis only rely on the relative y-axis behavior of the measured observables, the effect of multiple triggers on the final distributions is negligible.

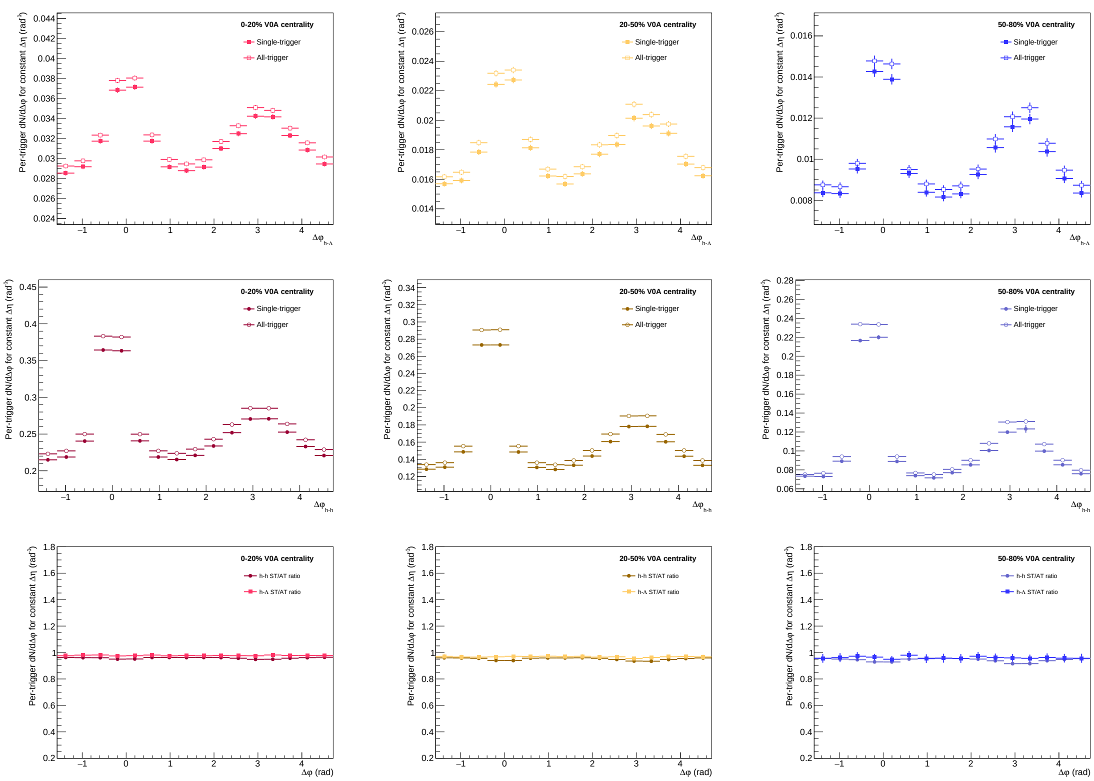

Figure 4.33: The per-trigger h-Λ (top) and h-h (middle) $\Delta\varphi$ distribution comparison between using a single trigger (closed points) and all triggers (open points) in a given event, along with the (single trigger)/(all trigger) distribution ratio (bottom), for the 0-20% (left), 20-50% (center) and 50-80% (bottom) multiplicity bins in the associated momentum range $2.0 < p_{\mathrm{T}} < 4.0$ GeV/c. The distributions are nearly identical up to a ≈ 0.95 scale factor, which is constant as a function of multiplicity.

4.2.3 Dihadron comparison with ϕ analysis

As mentioned in Section 4.1.3.2, the differences between open and hidden strangeness are investigated by taking the $\Lambda/\phi(1020)$ per-trigger yield ratios in the different kinematic regions (e.g. near-side jet, away-side jet, underlying event). This is done by taking a ratio of ratios, namely

$$\frac{(\text{h-}\Lambda)}{(\text{h-h})_1} \Big/ \frac{(\text{h-}\phi)}{(\text{h-h})_2}, \tag{4.21}$$

where the $(\text{h-}\phi)/(\text{h-h})_2$ ratio in the denominator is taken from previously published results in p–Pb collisions at $\sqrt{s_{\text{NN}}} = 5.02$ TeV which use the same angular correlation techniques to extract the per-trigger yields in the different regions [22]. This only reduces to the per-trigger $(\text{h-}\Lambda)/(\text{h-}\phi) \approx \Lambda/\phi$ yield ratios if two conditions are met:

1. The $(\text{h-h})_1$ and $(\text{h-h})_2$ yields are identical

2. The yields are extracted using the same procedure

Condition 2 has been met by design, as both analyses assume a flat UE taken as the average of the correlation distributions in the same $\Delta\varphi$ regions, and they both use bin-wise summation to extract the per-trigger yields. Condition 1, however, needs to be checked more thoroughly. While all of the selection criteria is the same between the two, the analyses were performed by two different humans with vastly different coding styles.

To this end, a direct comparison between the dihadron per-trigger $\Delta\varphi$ distributions from this analysis and the ϕ analysis is shown in Figure 4.34. The distributions are nearly identical across all multiplicity bins, which is indicated by the ratios at the bottom of the figure never deviating unity. As such, the cancellation of the $(\text{h-h})_1$ and $(\text{h-h})_2$ yields in Equation 4.21 is valid.

4.2.4 Resonance technique for Λ reconstruction

The Λ baryons used in this analysis are reconstructed by exploiting their characteristic V^0 decay topology, as discussed in Section 3.3. However, this method introduces a small physical bias in the Λ sample: only Λs which decay far enough from the primary vertex to be reconstructed as V^0s (i.e. they a detector-resolvable secondary vertex) are considered. While the average decay length of the Λ is quite large ($c\tau \approx 7.89$ cm

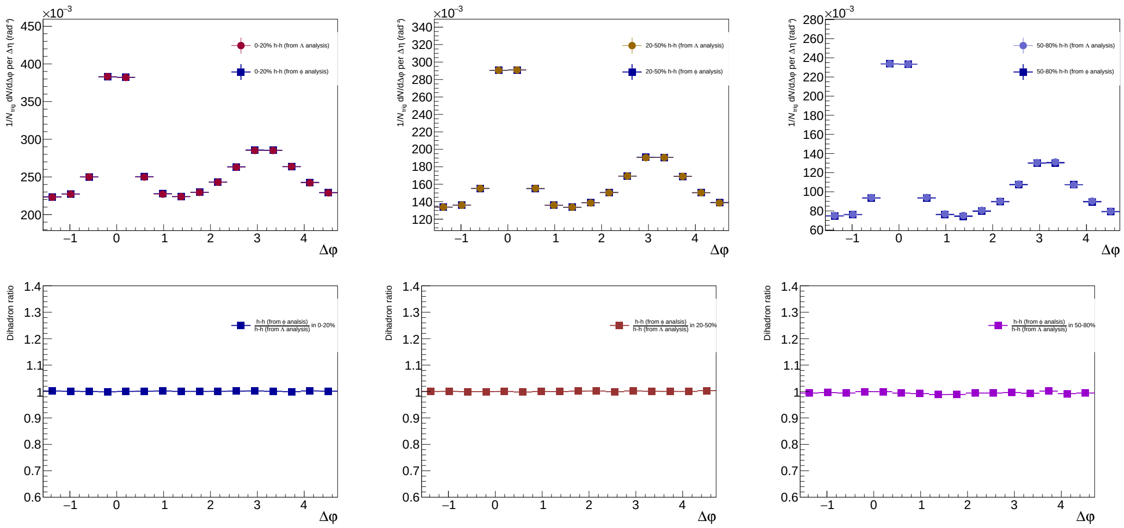

Figure 4.34: Comparison of the the dihadron $\Delta\varphi$ correlations between the ϕ and Λ analyses for the 0-20% (left), 20-50% (middle) and 50-80% (right) multiplicity bins, taken in the $2.0 < p_{\mathrm{T}} < 4.0$ GeV/c associated momentum range. They are functionally identical for all multiplicity bins.

where τ is the average lifetime), decay length distributions are exponentials of the form $e^{-t/\tau}$. This means that there is a small fraction of Λs that decay too quickly to be resolved using their V^0 topology, and thus are not included in the analysis. While the the single particle Λ efficiency is used to correct for the overall Λ yield, it may be possible that the h-Λ correlation shape is influenced by the exclusion of these short-lived Λ baryons.

To investigate this possible bias, another analysis is performed, whereby the Λ candidates are reconstructed using each oppositely-charged pπ pair in a given event.

Bibliography

[1] B. Pullman, *The Atom in the History of Human Thought*. Oxford: Oxford University Press, 1998, ISBN: 978-0-19-515040-7 (cit. on p. 1).

[2] J. Dalton, "Experimental enquiry into the proportion of the several gases or elastic fluids, constituting the atmosphere," *Memoirs of the Literary and Philosophical Society of Manchester*, vol. 1, pp. 244–258, 1805 (cit. on p. 1).

[3] E. Rutherford, "The scattering of α and β particles by matter and the structure of the atom," *Philosophical Magazine Series 6*, vol. 21, pp. 669–688, 1911 (cit. on p. 1).

[4] J. Chadwick, "Possible existence of a neutron," *Nature*, vol. 129, p. 312, 1932 (cit. on p. 1).

[5] H. Kendall, *Deep inelastic scattering: Experiments on the proton and the observation of scaling*, 1990. [Online]. Available: `https://www.nobelprize.org/uploads/2018/06/kendall-lecture.pdf` (visited on 08/21/2023) (cit. on p. 1).

[6] J. Friedman, *Deep inelastic scattering: Comparisons with the quark model*, 1990. [Online]. Available: `https://www.nobelprize.org/uploads/2018/06/friedman-lecture.pdf` (visited on 08/21/2023) (cit. on p. 1).

[7] R. Taylor, *Deep inelastic scattering: The early years*, 1990. [Online]. Available: `https://www.nobelprize.org/uploads/2018/06/taylor-lecture.pdf` (visited on 08/21/2023) (cit. on p. 1).

[8] R. P. Feynman, "The behavior of hadron collisions atthe uncertainties from these sources exhibit no multiplicity dependence, and a very small dependence on p_{T}. extreme energies," in *Special Relativity and Quantum Theory: A Collection of Papers on the Poincaré Group*, M. E. Noz and Y. S. Kim, Eds. Dordrecht: Springer Netherlands, 1988, pp. 289–304, ISBN: 978-94-009-3051-3. DOI: `10.1007/978-94-009-3051-3_25`. [Online]. Available: `https://doi.org/10.1007/978-94-009-3051-3_25` (cit. on p. 1).

[9] S. Roesler, R. Engel, and J. Ranft, "The monte carlo event generator DPMJET-III," in *Advanced Monte Carlo for Radiation Physics, Particle Transport Simulation and Applications*, Springer Berlin Heidelberg, 2001. arXiv: 0012252 [hep-ph] (cit. on pp. 11, 20).

[10] A. Kalweit, *Energy loss calibration of the ALICE TPC*, 2008 (cit. on p. 14).

[11] S. Acharya *et al.*, "Production of $K^*(892)^0$ and $\phi(1020)$ in pp and p–Pb collisions at $\sqrt{s_{NN}} = 5.02$ tev," *Phys. Rev.*, vol. C97, 2022. DOI: 10.1103/physrevc.106.034907. [Online]. Available: https://doi.org/10.1103%2Fphysrevc.106.034907 (cit. on p. 18).

[12] R. Brun *et al.*, *GEANT: Detector Description and Simulation Tool; Oct 1994*, ser. CERN Program Library. Geneva: CERN, 1993, Long Writeup W5013. DOI: 10.17181/CERN.MUHF.DMJ1. [Online]. Available: http://cds.cern.ch/record/1082634 (cit. on pp. 20, 86).

[13] S. Acharya *et al.*, "Two-particle differential transverse momentum and number density correlations in p–Pb and Pb–Pb at the LHC," *Phys. Rev. C*, vol. C100, no. 4, 2019. arXiv: 1805.04422 (cit. on p. 32).

[14] ——, "Longitudinal and azimuthal evolution of two-particle transverse momentum correlations in Pb–Pb collisions at $\sqrt{s_{NN}} = 2.76$ TeV," *Phys. Letters*, vol. B804, p. 135 375, 2020. arXiv: 1910.14393 (cit. on pp. 32, 36).

[15] ——, "K^0_S- and (anti-)Λ-hadron correlations in pp collisions at $\sqrt{s_{NN}} = 13$ TeV," *The European Phys. Journal*, vol. C81, no. 10, 2021. arXiv: 2107.11209 [nucl-ex] (cit. on pp. 35, 40, 41).

[16] R. Barlow, *Systematic errors: Facts and fictions*, 2002. arXiv: 0207026 [hep-ex] (cit. on pp. 38, 40, 50).

[17] S. Acharya *et al.*, "Multiplicity dependence of light-flavor hadron production in pp collisions at $\sqrt{s} = 7$ TeV," *Phys. Rev.*, vol. C99, 2019. arXiv: 1807.11321 [nucl-ex] (cit. on pp. 40, 41).

[18] B. A. et al., "Multiplicity Dependence of Pion, Kaon, Proton and Lambda Production in p-Pb Collisions at $\sqrt{s_{NN}} = 5.02$ TeV," *Phys. Letters*, vol. B728, pp. 25–38, 2014. arXiv: 1307.6796 [nucl-ex] (cit. on pp. 40, 41, 57).

[19] B. Abelev *et al.*, "K^0_S and Λ production in Pb-Pb collisions at $\sqrt{s_{\mathrm{NN}}} = 2.76$ tev," *Phys. Rev. Lett.*, vol. 111, 2013. arXiv: `1307.5530 [nucl-ex]` (cit. on p. 41).

[20] ——, "Long-range angular correlations of π, K and p in p-Pb collisions at $\sqrt{s_{\mathrm{NN}}}$ = 5.02 TeV," *Phys. Lett.*, vol. B726, pp. 164–177, 2013. arXiv: `1307.3237 [nucl-ex]` (cit. on pp. 55, 56).

[21] ——, "Observation of partonic flow in proton-proton and proton-nucleus collisions," *Nature Phys.*, vol. TBA, TBA, 2023. arXiv: `TBA [nucl-ex]` (cit. on p. 55).

[22] J. Blair, "Investigating strangeness enhancement in jet and medium via $\phi(1020)$ production," 2023. arXiv: `TBA [nuc-ex]` (cit. on p. 93).